

# *POLITECNICO DI TORINO*

*Master of Science in Biomedical Engineering*



*Master thesis*

## Hydroxyapatite-containing gelatin hydrogels coupled with Poly( $\epsilon$ -caprolactone)/hydroxyapatite 3D printed scaffolds: optimized fabrication method and characterization

### *SUPERVISORS*

*Prof. Gianluca Ciardelli*

*Dr. Monica Boffito*

*Dr. Elena Mancuso*

*Dr. Chiara Tonda Turo*

*CANDIDATE*

*Giuliana Zappalà*

*March 2020*

# Table of content

<b>Abstract</b> .....	4
<b>1. Introduction</b> .....	6
<b>1.1. Tissue Engineering and Regenerative medicine</b> .....	6
<b>1.2. Biomaterials in Tissue Engineering</b> .....	7
<b>1.3. Hydrogels</b> .....	8
<b>1.3.1. Gelatin-based hydrogels</b> .....	12
<b>1.3.2. Gelatin methacryloyl-based hydrogels</b> .....	15
<b>1.4. Hydrogel composite biomaterials</b> .....	17
<b>1.4.1. Gelatin/Hydroxyapatite and gelMA/Hydroxyapatite based hydrogel</b> .....	18
<b>1.5. Rapid prototyping techniques for scaffold production</b> .....	20
<b>1.5.1. Three-dimensional printing</b> .....	21
<b>1.5.2. Multicomponent scaffolds integrating hydrogels and thermoplastic polymers</b> .....	22
<b>2. Thesis goal</b> .....	24
<b>3. Materials and methods</b> .....	25
<b>3.1. Materials</b> .....	25
<b>3.2. Nomenclature</b> .....	25
<b>3.3. Synthesis of methacryloyl gelatin</b> .....	25
<b>3.4. GelMA Characterization</b> .....	26
<b>3.4.1. Attenuated Total Reflectance Fourier Transform Infrared (ATR-FTIR) Spectroscopy</b> .....	26
<b>3.4.2. Proton nuclear magnetic resonance spectroscopy</b> .....	27
<b>3.4.3. Colorimetric Ninhydrin assay (Kaiser test)</b> .....	27
<b>3.4.4. Tube inverting test</b> .....	28
<b>3.5. gelMA hydrogel preparation</b> .....	28
<b>3.6. GelMA hydrogel characterization</b> .....	29
<b>3.6.1. Photorheological analyses</b> .....	29
<b>3.6.2. Re-swelling test</b> .....	29
<b>3.6.3. Micro-Computed Tomography (<math>\mu</math>CT) analyses</b> .....	30
<b>3.7. Hydroxyapatite (HA) synthesis</b> .....	30
<b>3.7.1. Hydroxyapatite obtained from rapid mix method (HA r.m.)</b> .....	31
<b>3.7.2. Hydroxyapatite obtained from precipitation at 100°C (HA prec.)</b> .....	31
<b>3.8. Hydroxyapatite characterization</b> .....	32
<b>3.8.1. Energy dispersive X-ray (EDX) spectroscopy</b> .....	32
<b>3.8.2. X-ray powder diffraction (XRD) analysis</b> .....	32

3.8.3.	Field Emission Scanning Electron Microscope (FESEM) analysis .....	33
3.9.	Hydroxyapatite dispersion in gelMA solutions .....	33
3.9.1.	Dispersion stability test .....	34
3.9.2.	Tube inverting test.....	35
3.10.	Preparation of photo-crosslinked GelMA/HA hydrogels.....	35
3.11.	gelMA/HA hydrogels characterization.....	35
3.11.1.	Attenuated Total Reflectance Fourier Transform Infrared (ATR-FTIR) Spectroscopy .....	35
3.11.2.	Scanning Electron Microscopy (SEM) analyses .....	35
3.11.3.	Photorheological measurements.....	36
3.11.4.	Micro-Computed Tomography ( $\mu$ CT) analyses .....	36
3.12.	Polycaprolactone/Hydroxyapatite based scaffold realization: EnvisionTEC 3D Bioplotter .....	36
3.12.1.	The CAD file .....	37
3.12.2.	The Perfactory RP software .....	37
3.12.3.	The printing process .....	38
3.13.	PCL/HA based scaffold characterization .....	40
3.13.1.	Attenuated Total Reflectance Fourier Transform Infrared (ATR-FTIR) Spectroscopy .....	40
3.13.2.	Micro-Computed Tomography ( $\mu$ CT) analyses .....	41
3.13.3.	Scanning Electron Microscopy (SEM) analyses .....	41
3.13.4.	Compressive test.....	41
3.13.5.	Swelling test .....	41
3.14.	Preparation of gelatin and gelatin/HA r.m. crosslinked hydrogels .....	42
3.15.	Gelatin and gelatin/HA r.m. hydrogels characterization.....	43
3.15.1.	Attenuated Total Reflectance Fourier Transform Infrared (ATR-FTIR) spectroscopy .....	43
3.15.2.	Micro-Computed Tomography ( $\mu$ CT) analyses .....	43
3.15.3.	Scanning Electron Microscopy (SEM) analyses .....	43
3.15.4.	Re-swelling test .....	44
3.16.	PCL/HA-gel/HA r.m. multicomponent scaffolds fabrication .....	44
3.17.	PCL/HA-gel/HA r.m. multicomponent scaffolds characterization.....	45
3.17.1.	Micro-Computed Tomography ( $\mu$ CT) analyses .....	45
3.17.2.	Scanning Electron Microscopy (SEM) analyses .....	45
3.17.3.	Re-swelling test .....	45
4.	Results .....	46
4.1.	GelMA characterization.....	46

4.1.1.	Attenuated Total Reflectance Fourier Transform Infrared (ATR-FTIR) Spectroscopy	46
4.1.2.	Proton nuclear magnetic resonance ( <sup>1</sup> H-NMR)	47
4.1.3.	Ninhydrin colorimetric assay (Kaiser test)	48
4.1.4.	Tube inverting test	59
4.2.	GelMA hydrogel characterization	50
4.2.1.	Photo-rheological characterization	50
4.2.2.	Re-swelling test	51
4.3.	Hydroxyapatite characterization	52
4.3.1.	ATR-FTIR analyses on hydroxyapatite powders	52
4.3.2.	XRD analyses	53
4.3.3.	EDX analyses	54
4.3.4.	Field Emission Scanning Electron Microscope (FESEM) analysis	57
4.4.	Dispersion of HA powder in gelMA	58
4.4.1.	Dispersion stability	61
4.4.2.	Tube inverting test on gelMA/HA composite solutions	64
4.5.	GelMA/HA based hydrogel	64
4.5.1.	Photo-rheological characterization	67
4.5.2.	μCT analyses	69
4.6.	PCL/HA based scaffolds characterization	71
4.6.1.	Attenuated Total Reflectance Fourier Transform Infrared (ATR-FTIR) Spectroscopy	71
4.6.2.	μCT analyses	72
4.6.3.	SEM analyses	73
4.6.4.	Compressive test	74
4.7.	Gelatin and gelatin/HA crosslinked hydrogels preparation	75
4.8.	Gelatin and gelatin/HA crosslinked hydrogels characterization	76
4.8.1.	ATR-FTIR spectroscopy	76
4.8.2.	μCT analyses	76
4.8.3.	Re-swelling test	78
4.9.	Gel/HA r.m.-PCL/HA multicomponent scaffold fabrication	78
4.10.	Gel/HA r.m.-PCL/HA multicomponent scaffold characterization	78
4.10.1.	μCT analyses	78
4.10.2.	Re-swelling test	79
<b>5.</b>	<b>Conclusion and future works</b>	<b>82</b>
	<b>Bibliography</b>	<b>86</b>

## Abstract

The tissue engineering field has been gaining increasing relevance over the last few decades, due to its potentiality in health and life improvement. The literature reports many research works dealing with the use of hydrogels in regenerative medicine because of their durability, reproducibility, hydrophilicity and biocompatibility. Hydrogel mechanical properties can be improved by mixing their constituent polymer with a reinforcing phase (e.g., hydroxyapatite, HA) or by combining them with a thermoplastic framework. Such an approach also opens the way to the possibility to produce multi-component scaffolds suitable for new functional tissue formation, e.g., osteochondral tissue. This work fell within this context and aimed at the design of multi-component matrices resulting from the combination of 3D printed scaffolds and hydrogels. Specifically, glutaraldehyde (GA) cross-linked and photocured gelatin/HA composite gels (gel/HA and GelMA/HA, respectively) were designed with the aim to combine them with poly( $\epsilon$ -caprolactone)/HA (PCL-HA) 3D printed scaffolds. Each constituent of the composite scaffolds was first designed and thoroughly characterized. GA crosslinked gels were obtained by incubating physically gelled gelatin samples (from porcine skin, type A, 15% w/v) in a GA aqueous solution (0.25% v/v) for 10 min. As a different approach to design gelatin crosslinked gels, photocurable methacryloyl gelatin (GelMA) with different degrees of methacryloylation (i.e., 67 and 74%) was synthesized by reacting gelatin and methacrylic anhydride. GelMA solutions (10 and 15% w/v) were photocured using Lithium phenyl-2,4,6-trimethylbenzoylphosphinate (LAP) as photoinitiator (0.05 and 0.05% w/v) and a UV light source (10 mW/cm<sup>2</sup>, 365 nm). Stiffer hydrogels were obtained by increasing GelMA degree of methacryloylation, LAP amount and gelMA concentration. Photo-rheological measurements evidenced higher storage modulus values and faster crosslinking rates with increasing LAP concentration. Higher storage modulus values were also achieved by increasing GelMA concentration within the hydrogels. In order to develop composite hydrogels, hydroxyapatite (HA) powder was synthesized following two different precipitation methods, leading to HA prec. and HA r.m.. Both HA r.m. and HA prec. exhibited a Ca:P ratio (1.66 and 1.87, respectively) similar to the stoichiometric value of 1.67, meanwhile round shape and spindle-shape morphologies was obtained for HA prec. and HA r.m., respectively. Then, HA dispersion protocol within gelatin and gelMA solutions was optimized. The different distribution of HA powders turned out to be correlated to the type and concentration of HA within the samples (better dispersion was achieved with HA r.m. compared to HA prec. and at lower HA concentration, as assessed through scanning electron microscopy and micro-computed tomography ( $\mu$ CT)). In view of the final goal of this work, poly( $\epsilon$ -caprolactone)/HA 3D-printed structures with approx. 60% porosity were also fabricated (HA at 10% w/w) through a pressure assisted microsyringe technique. Finally, the coupling between PCL/HA scaffolds and

gel/HA r.m. composite hydrogels (gelatin and HA r.m. at 15 and 10% w/v, respectively) was performed. Briefly, hydrogel solution was pipetted onto the PCL/HA scaffold, exploiting the temperature driven gelation to achieve the coupling, followed by chemical crosslinking mediated by GA. The final structures were characterized in terms of swelling capability, which turned out to decrease with respect to the gels as such, due to the presence of PCL/HA structure as hydrophobic component. Similarly, also porosity decreased of approx. 10%, as a consequence of the integration process that almost completely closed the pores present in the first scaffold layers.  $\mu$ CT analyses highlighted a good integration of the hydrogel into the 3D structure, thus validating the here-adopted protocol for multi-component scaffold preparation. The results of this work provided a first proof of the feasibility to design multicomponent 3D scaffolds by combining different forming-materials and fabrication technologies. The here-manufactured scaffolds could have high potential for tissue engineering applications, in particular in all those cases in which an interface between different tissues should be repaired and regenerated, such as in osteochondral tissue engineering.

# 1. Introduction

## 1.1 Tissue Engineering and Regenerative medicine

The field of *Tissue engineering* was born at the end of 1980 with the aim of restoring living tissues when they are damaged, destroyed or affected by congenital diseases [1]. The idea of tissue regeneration was introduced in ancient times (e.g., it was described also in Prometheus myth), but only in the last decades a rigorous definition of *Regenerative medicine* has been formulated [1]. According to Langer and Vacanti, “the newly recognized multi-disciplinary field of regenerative medicine aims at the replacement, repair or restoration of normal function to disease organs/tissues by the delivery of safe, effective and consistent therapies composed of living cells, administered either alone or in combination with specially designed materials” (Langer & Vacanti 1993) [2]. The three pillars of regenerative medicine are cells, scaffolds and bioreactors. Concerning cells, different phenotypes can be used for biomedical applications, depending on their biological characteristics, such as proliferation and differentiation ability, and their origin. For example, autologous adult cells can be extracted from the patient’s body and grown *in-vitro* in a way to regenerate a specific kind of tissue. Unfortunately these cells usually have a limited proliferative ability and sometimes they are present in small amount in the body. Since the end of 1990, a lot of studies were carried out on isolated Embryonal Stem cells and Adult Stem cells which can overcome this barrier. More recently, Induced Pluripotent Stem cells (iPS) have been introduced by properly reprogramming somatic cells, with the additional potential of overcoming ethical limits attributed to the retrieval of Embryonal Stem cells [2]. The interaction between cells and scaffold biomaterials is one of the fundamental concepts to take into account in tissue regeneration. Foreign species, in fact, can elicit an immune response when implanted in the human body, and also direct cells to a certain pattern of differentiation or stimulate their proliferation or death. In order to reproduce a tissue *in-vitro*, cell expansion should be realized in a three-dimensional template, the scaffold, with mechanical and chemical properties similar to those of the physiological environment. Generally, scaffolds have to satisfy few important requirements:

- 1) They must be **biocompatible**: the scaffold must be integrated into the human host tissue without causing any immune response;
- 2) They serve as a matrix with appropriate **surface chemistry**, which can modulate cell response thanks to the functionalization with proper ligands or by absorbing adhesion proteins;
- 3) **Their biodegradation** must take place with an appropriate rate after implantation: in order to obtain a new functional tissue with physiological characteristics, regeneration and scaffold degradation should occur at the same speed;

- 4) Scaffolds must **not** be **toxic** and the degradation must not produce noxious by-products that could elicit an inflammatory response or cell death;
- 5) **Mechanical properties** tailored by **high porosity**, **interconnected pores** and an **organized structure** are necessary to permit oxygen and nutrients supply and waste removal, but also to allow cells growth;
- 6) **Good manufacturing practices** (GMP) should be followed in order to obtain high quality products, scalable for a clinical use [2],[3].

The aid of bioreactors is usually required to obtain a more homogeneous supply of oxygen and nutrients, but also to furnish different stimuli to the cells seeded into the scaffold [2].

In the field of Tissue Engineering (TE), different approaches can be followed: (i) growth of a tissue or organ *in-vitro* followed by its insertion into the body; (ii) implantation of a scaffold seeded with cells with tissue development *in-vivo*; (iii) seeding of a scaffold with cell and waiting awhile before incorporating the construct into the body; and (iv) implantation of a scaffold without cells (in case enriched with drugs or specific molecules such as protein or hormones) in a way to allow the patient's cells to populate it [4].

## 1.2 Biomaterials in Tissue Engineering

According to the American National Institute of Health a "Biomaterial is defined as any substance, other than a drug, or combination of substances synthetic or natural in origin, which can be used for any period of time, as a whole or as a part of a system which treats, augments, or replaces any tissue, organ, or function of the body" [5]. Biomaterials can be used to produce scaffolds in Tissue Engineering applications and, as said previously, they have a key role in influencing cell behavior and fate. These constructs could be seen as "biomatrices" that provide a physiological-like environment to the cells, mimicking the native extracellular matrix [6]. Biomaterials for biomedical applications can be divided into three generations. First generation biomaterials were born between the 1960s and 1970s and they were biologically inert when implanted *in-vivo*. Their basic requirement was to "achieve a suitable combination of physical properties to match those of the replaced tissue with a minimal toxic response of the host" (Hench 1980) [7]. In a way to overcome the inertness concept, characteristics of bioactivity and biodegradability were gradually introduced as fundamental features for biomaterials. Thus, the second generation of biomaterials, which appeared in the mid-1980s, was characterized by the production of bioactive materials able to elicit a biological response, interacting with the physiological environment and enhancing the tissue/surface bonding. Another class of second generation biomaterials consisted of resorbable ones, which were able to degrade meanwhile new functional tissue was forming. Concerning third generation biomaterials, they were

properly designed “to stimulate specific cellular responses at the molecular level” (Hench & Polak 2002) [7]. These biomaterials are both resorbable and bioactive, thus capable to interact with cell integrins, guide cell adhesion, proliferation and differentiation. Among the several types of scaffold biomaterials, natural and synthetic polymers have gained great relevance in Tissue Engineering applications due to the easy fabrication, the wide range of composition and physical properties, the opportunity to carry out surface modifications and functionalizations in a way to immobilize cells and biomolecules. Natural polymers are categorized in two classes: proteins and polysaccharides. They have great biocompatibility and contain ligand that can bind to cell receptors. In fact, some of them can be found in the extracellular matrix (e.g., chondroitin sulphate, heparin, hyaluronic acid, collagen, laminin, fibrin, etc.). The difficulty in processing and producing materials with controllable characteristics is one of the major limits that affect natural polymers. Another constraint is that of immunogenicity of the materials which can elicit an inflammatory response from the human body [3],[6]. On the contrary, synthetic polymers (e.g., poly-(glycolic acid), poly(lactic acid), poly( $\epsilon$ -caprolactone), poly(ethylene glycol), poly(urethane)s and poly(glycerol sebacate)), are preferable in scaffold production for their predictable, tunable and reproducible degradation rate, mechanical and chemical properties [3],[6]. However, compared to natural polymers, they possess inferior biocompatibility. Natural and synthetic polymers can be used in combination to create composite scaffold materials in order to merge their complementary advantages of biocompatibility and reproducibility. Another application of these compounds is hydrogel fabrication [3],[6]. Hydrogels are based on hydrophilic polymers which crosslinking permit to uptake even the 99% of water volume if introduced in a liquid environment. Thanks to this characteristic, hydrogels have a great swelling capability and can be injected *in vivo* with low invasive methods. This class of biomaterials is involved in a lot of biomedical applications as they can easily incorporate cells and bioactive molecules, fill the site of injury and provide embedded cells with physiological forces [3].

### 1.3 Hydrogels

Hydrogels constitute a class of cross-linked materials arising from the reaction of one or more monomers. They have a three-dimensional network, a great capability to absorb water (i.e., water mass fraction up to thousand times greater than the polymer one) and swell without dissolving [5],[15]. Thanks to their durability, reproducibility, hydrophilicity and biocompatibility, hydrogels are a suitable class of matrices for tissue engineering applications [10]. They can easily encapsulate soluble factors, enzymes and drugs which are then release while the material is in the swollen state. Moreover, surface modifications can be carried out in order to improve their interaction with cells [5].

Concerning hydrogel swelling mechanism, when the dry material is exposed to water, the latter starts to hydrate different groups (i.e., hydrophilic groups and hydrogen bonding groups) forming the “primary bound water”. After the chains start to expand, hydrophobic moieties are exposed to water and their interactions lead to a water coating called “secondary bound water”. When short-range interactions end, an additional swelling occurs until an equilibrium state is reached between osmotic forces and elastic retraction forces [5].

Hydrogels can be distinguished into “permanent” and “reversible” systems (Fig. 1).

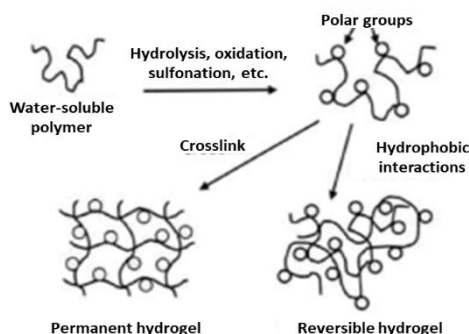


Figure 1: Permanent and reversible hydrogels [11].

The first ones are characterized by the presence of covalent bonds between the chains, while the second ones possess reversible crosslinking due to intermolecular and intramolecular interactions (such as hydrophobic interactions and hydrogen bonding). Another classification dividing hydrogels into “conventional” and “stimuli responsive” systems. Concerning conventional hydrogels, they simply swell in water without dissolving, while stimuli responsive hydrogels (that usually have hydrophobic moieties and can be charged) change their state depending on external stimuli (chemical or physical cues) [5],[9]. As highlighted in Fig. 2, chemical stimuli are:

- **pH variation:** changes in environmental pH lead to a different swelling thanks to the presence of acidic or basic groups in the polymer network (usually a polyelectrolyte) that can accept or release protons [12],[13];
- **Ionic strength:** free ions are exploited to elicit ionic interactions with cationic or anionic polymers. These forces, combined with water-polymer thermodynamic and elasticity of the polymer, cause its swelling [14];
- **Solvent composition:** entropy and enthalpy change generated when mixing polymer and solvent, can lead to swelling. The latter, in fact, depends on interaction between polymers chains and thermodynamic forces arisen from solvent and polymer mixing [13];
- **Molecular species:** gels’ molecular species co-assemble thanks to non-covalent interactions (i.e., hydrogen bonding, van der Waals forces, etc.) between its molecules [13].

While physical stimuli include:

- **Temperature:** when hydrogel chains are not covalently bound, they can undergo a sol-gel or gel-sol transition when exposed to appropriate temperature variations, depending on the polymer characteristics [15]. There are two different types of temperature sensitive-polymers: the ones which form gels when the temperature goes down under a certain limit (Upper Critical Solution Temperature, UCST) and the ones which need to overcome the Lower Critical Solution Temperature (LCST) to undergo a sol to gel transition [16]. For example, some natural polymers are able to move from a random coil conformation to an organized one (with double helices and aggregates formation), forming physical hydrogels, when exposed to a temperature lower than temperature transition [17]. Another classification can be made into negatively and positively thermosensitive polymers, where the first ones swell with decreasing temperature and the second ones with the opposite phenomenon [15];
- **Electric field:** polyelectrolytes are sensitive to electric current changes that can elicit a swelling response in the hydrogel [14];
- **Magnetic field:** magneto-rheological and ferrofluids containing nanoparticles sensitive to an applied field behave as swelling agent making hydrogels able to uptake a larger amount of liquid [18];
- **Light:** UV or visible light can be exploited to induce hydrogel modifications. Concerning UV-sensitive hydrogels, a leuco derivative molecule divides into a pair of tryphenylmethil cations upon exposure to irradiation, inducing an increase in osmotic pressure and then hydrogel swelling. Shrinkage phenomena occur when the irradiation ends. As regards visible light-sensitive hydrogels, the irradiation is dissipated as heat by a chromophore inserted into the hydrogel, resulting in an increasing temperature which causes the swelling (hydrogels are, in this case, thermosensitive) [15];
- **Pressure:** pressure changes can be exploited to induce variation in hydrogels, thanks to their viscoelastic properties [19];
- **Sound:** molecular switching and molecule transitory movement can be induced applying an opportune sound stimulus [20];

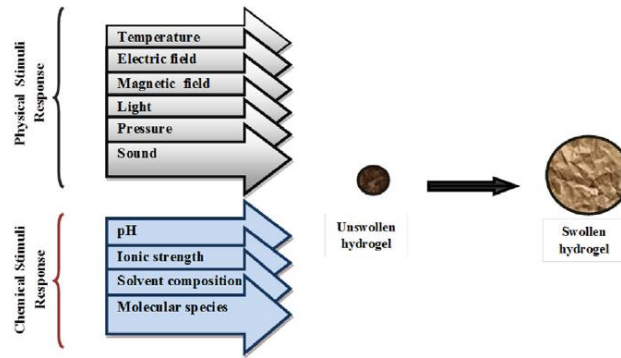


Figure 1: Physical and chemical stimuli responsive hydrogels [9].

Beside the abovementioned classification methods, hydrogel products can be distinguished depending on different features, as highlighted in Fig. 3.

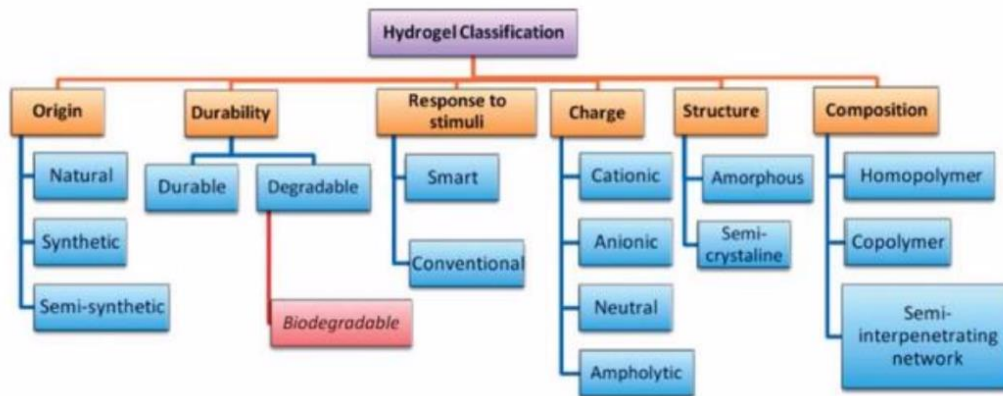


Figure 2: Hydrogels classification [21].

Generally, the three pillars of hydrogel formation are: monomer, initiator and cross-linker. In order to realize hydrogels, copolymerization and free radical polymerization methods can be exploited by reacting hydrophilic monomers and cross-linkers. Different techniques are used in hydrogel preparation, such as bulk polymerization, solution polymerization, suspension polymerization and polymerization by irradiation. Both natural and synthetic polymers can be used in hydrogel fabrication, where the latter are preferred for their tailorable characteristics of water absorption, durability and reproducibility [9]. Swelling capability of synthetic hydrogels derives from the presence of specific groups in their backbone (e.g. carboxyl, amide, amino and hydroxyl groups) which cross-linking impedes the dissolution in water, which happens in non-crosslinked state [22]. Different methods can be used to enable cross-linking reactions: chemical reactions, ionizing radiations (they trigger the formation of free radicals in the chain which can react starting the polymerization), and physical interactions. In order to obtain a cross-linked material starting from natural polymers, radical polymerization is usually required using the functional groups contained in the polymer chains. Eventually, natural polymers, can be functionalized with adequate moieties suitable for radical polymerization [9]. Moreover, hydrogel materials present several advantages

including optimal absorption capacity at a tailorable rate, durability and stability, no toxicity and biodegradability, re-wetting capability and cheap production costs. For these reasons this class of biomaterials is excellent for tissue engineering, but also for diagnostics and biosensor applications [9]. Extracellular matrix can be mimicked acting on hydrogels morphology and composition, enabling cell proliferation, adhesion and differentiation thanks to the 3D framework. External stimuli can be provided to cells, exploiting the release of soluble factors and other specific molecules while they are in a swollen state. Furthermore, chemical changes in hydrogels chain can be carried on including degradation or adhesion motifs like those present in the extracellular matrix.

### 1.3.1 Gelatin-based hydrogels

Recently a lot of studies have been carried out concerning the use of collagen (Fig. 4) as a material for tissue engineering (TE). Some examples

reported in literature concern wound healing, bone tissue regeneration, vascular graft and cardiovascular engineering applications [23],[24],[25]. Moreover, being collagen an extracellular matrix (ECM) protein, it can

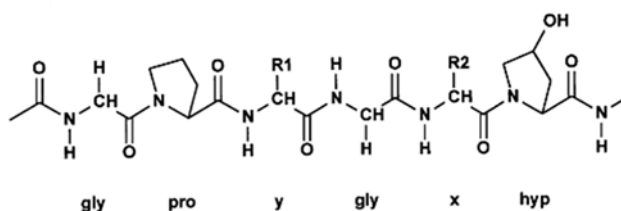


Figure 4: chemical structure of collagen type I.

interact with cells affecting their behavior, but it is also able to provide mechanical properties, resistance and integrity to the tissues [26],[27]. Some of the major advantages of collagen use concern its simple chemical or physical modification by crosslinking (thanks to glutaraldehyde, cyanamide, carbodiimide treatment etc.), its biodegradability, biocompatibility and low antigenicity [28]. However, collagen production is costly because of its difficult isolation from animals and the mild and not-aggressive conditions required during the processing to avoid its denaturation. Furthermore, the protein is characterized by a high swelling rate *in vivo* due to its hydrophilicity and by a poor control of the degradation rate [3],[10]. Concerning scaffold realization with collagen, other drawbacks are related to its poor mechanical properties, which make further functionalization with other components required to reach adequate final properties [24]. In order to overcome collagen disadvantages, several researches have been carried out concerning the use of gelatin (Fig. 5) as a material for Tissue Engineering applications.

Gelatin derives from collagen denaturation (Fig. 6) through alkaline or acid treatments.

Hence, two different types of gelatin can be obtained: type B (acid, isoelectric point 5.0) and type A (basic, isoelectric point 9.0)

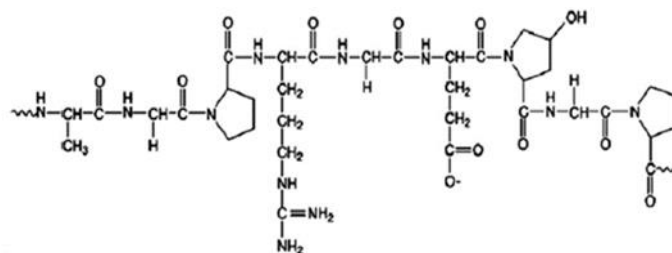


Figure 5: Chemical structure of gelatin.

[24],[29]. Thus, the collagen characteristic repetitive amino acid sequence (Glycine, Proline and Hydroxyproline triplet) is kept (Fig.4), but its right handed supercoil structure is lost. Some differences can be noticed among gelatin products, depending on the collagen source and adopted denaturation process. For example, depending on the native collagen used, gelatin secondary structure can vary, presenting  $\alpha$ ,  $\beta$  and  $\gamma$ -chains, which differ from their molecular weight. The latter, combined with amino acids composition, can affect mechanical properties, such as viscosity and strength, and gelation temperature of the resulting gelatin [10]. Moreover, since the production of gelatin is simpler compared to that of collagen, it is a cheaper material to obtain. Other advantages concern its biocompatibility and biodegradability, but also the better solubility and minor antigenicity compared to collagen, considering its denatured origin. Cell adhesion sites, such as arginine-glycine-aspartic

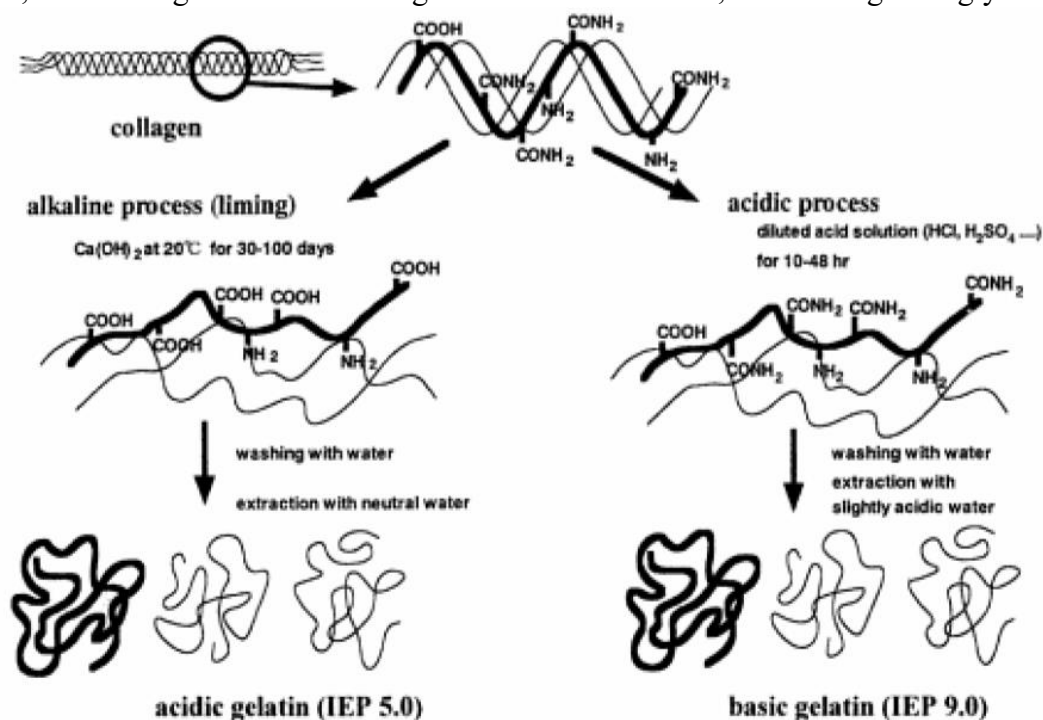


Figure 6: Gelatin extraction from denatured collagen [30].

acid (RGD) and metalloproteinases sequences, are also contained in gelatin chains. Furthermore, the groups present in the side chains of gelatin can be exploited for further functionalizations (e.g., crosslinking agents and targeting molecules). Gelatin could be used as porous scaffold in Tissue Engineering, acting as a framework for surrounding tissue if blended with other materials (e.g., ceramics like hydroxyapatite in bone tissue engineering). Other potential applications of gelatin have been reported in cell therapy and drug delivery [30]. Gelatin drawbacks are due to its solubility in aqueous solution and poor mechanical properties. Moreover, considering its sol-gel transition at almost  $30^\circ\text{C}$ , a further crosslinking is required in order to use it as a scaffold in Tissue Engineering avoiding its dissolution at body temperature [16]. Gelatin, which undergoes gelation thanks to hydrogen bonds formation among polymer chains, is part of UCST materials. Lowering the

temperature, structural changes occur from a random coil state to triple helices and helical aggregates, as shown in Fig. 7 [16]. Gelatin hydrogels can be used as porous scaffolds in regenerative medicine (Tab. 1) and a lot of studies have been carried out, demonstrating that gelatin cryogel scaffolds support adhesion and growth of fibroblasts, endothelial cells, glial cells, osteoblasts and epithelial cells. Moreover, gelatin hydrogels can be combined with other materials like *glycosaminoglycans* (GAGs) which make them optimal for cell interaction, but also with calcium phosphates or both. Gelatin can also be used as part of composite scaffolds in combination with synthetic polymers like poly(L-lactic acid), poly(urethane)s and poly(caprolactone) [16]. In order to obtain chemical hydrogels with covalent bonds, gelatin crosslinking is carried out thanks to the presence of several side chains that can be cross-linked after functionalization with specific groups. The cross-linking reagent must be water-soluble, such as glutaraldehyde, diisocyanates, carbodiimides, genipin, polyepoxy-compounds and acyl azides. Usually, gelatin modification occurs acting on the amino groups of lysine and hydroxylysine residues. For instance, a possible approach for gelatin functionalization consists in reacting its pendant amines with methacrylic anhydride, obtaining a methacrylamide-modified gelatin that can be crosslinked in the presence of a photoinitiator, through irradiation of its solutions with UV or visible light. Other ways to realize chemical gelatin hydrogels involve e-beam and gamma-rays, which do not require the use of solvent and perform crosslinking and sterilization at the same time.

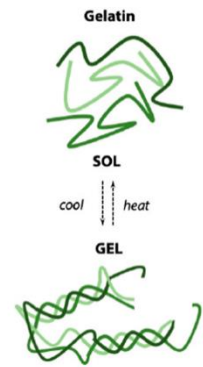


Figure 7: Mechanism of sol (random coil)-gel (triple helices aggregates) transition of gelatin [16].

Table 1: Different applications of gelatin products in Tissue Engineering [16].

type of gelatin	application
gelatin sponge	adipose tissue
gelatin/poly( $\epsilon$ -caprolactone) nanofibers, VEGF immobilized gelatin, polyethylene-glycol diacrylate/gelatin, chitosan/gelatin, gelatin/PET nanofibers, gelatin/PES fibers, gelatin/PTFE	blood vessel
hydroxyapatite chitosan/gelatin, gelatin/poly( $\alpha$ -hydroxy acids), glutaraldehyde cross-linked gelatin, hydroxyapatite/gelatin, $\beta$ -tricalcium phosphate/gelatin, gelatin/poly( $\epsilon$ -caprolactone) nanofibers, gelatin microcarriers/polyester, micro- and nanohydroxyapatite/chitosan/gelatin, rhBMP-2-loaded gelatin/nanohydroxyapatite/fibrin, poly[(L-lactide)-co-(epsilon-caprolactone)]/gelatin, gelatin-based photopolymers	bone
gelatin/chondroitin-6-sulfate/hyaluronan, plasmid DNA/chitosan/gelatin, gelatin microparticle/OPF, gelatin microparticle/poly(D,L-lactide- $\epsilon$ -caprolactone), TGF- $\beta$ 1-loaded gelatin, ceramic/gelatin, esterified hyaluronan/gelatin, gelatin/chitosan/hyaluronan	cartilage
transglutaminase cross-linked gelatin, proanthocyanidin cross-linked chitosan/gelatin, gelatin/poly(D,L-lactide), gelatin fibers, PHBHHx/gelatin, PVA/gelatin, PNIPAM/gelatin, gelatin- and fibronectin-coated PE multilayer nanofilms, gelatin/montmorillonite/cellulose, chitosan/PEG/gelatin, gelatin/hydroxyphenylpropionic acid, gelatin microparticles, gelatin/chitosan cryogels, genipin-cross-linked PCL/gelatin nanofibers, silk sericin/gelatin, $\alpha$ -chitin/gelatin, agarose/gelatin cryogel, hyaluronan/gelatin	general
gelatin/polyurethane, photo-cross-linked gelatin, alginate/gelatin	heart
gelatin/chondroitin-6-sulfate/hyaluronan, gelatin, glutaraldehyde cross-linked gelatin/chondroitin-6-sulfate	intervertebral disk
gelatin/silk fibroin	ligament
cross-linked sodium alginate/gelatin, chitosan/gelatin	liver
gelatin/PCL nanofibers	muscle
photo cross-linkable gelatin, gelatin/hydroxyphenylpropionic acid	nerve
chitosan/gelatin/glycerol phosphate	nucleus pulposus
gelatin/agarose	pancreas
glutaraldehyde cross-linked gelatin	skin

### 1.3.2 Gelatin methacryloyl-based hydrogels

Gelatin methacryloyl (gelMA), synthesized for the first time in 2000 by Van den Bulcke and coworkers [31], is a material derived from the reaction between gelatin and methacrylic anhydride (Fig. 8a). The latter enables the grafting of methacrylate or methacrylamide groups to hydroxyl

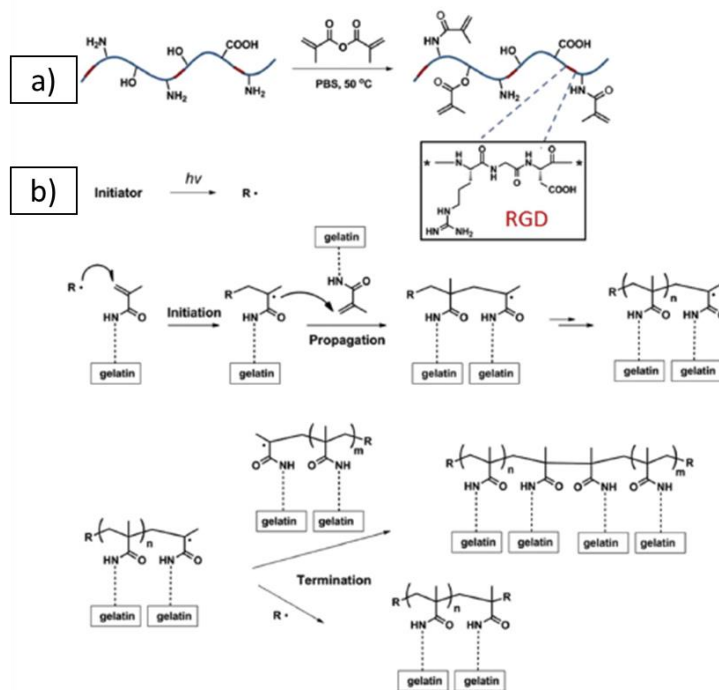


Figure 8: a) Reaction between gelatin and methacrylic anhydride, b) photo initiated radical polymerization of gelMA [31].

groups and primary amines exposed along gelatin backbone, respectively. Thanks to these moieties, a radical polymerization is achieved in the presence of small quantities of a photo-initiator (e.g., Irgacure 2959 and Lithium phenyl-2,4,6-trimethylbenzoylphosphinate) and UV or visible light irradiation. In this way, a permanent and stable hydrogel, even at physiological temperature, with intra and inter chains covalent bonds is obtained (Fig. 8b). The methacryloylation reaction occurs in mild conditions in terms of temperature (i.e., 50 °C) and pH (i.e., 7.4), leading to better monitoring of temporal and spatial conditions of the process. Moreover, the bonding with methacryloyl moieties affects a small amount (<5%) of amino acid residues of gelatin, allowing to not disrupt its biological properties. Hence, tailorable physical characteristics and bioactive behavior are proper of gelMA-based scaffolds, which contain ECM sequences (such as RGD and metalloproteinases) thanks to gelatin precursor, favoring cell adhesion, proliferation, but also enzymatic degradation. For these reasons, gelMA hydrogels can be exploited in 2D, 3D cultures and in cell-laden scaffolds realization. It has been reported in literature that mechanical and morphological properties (such as pore gradient and size) are tunable, acting on the degree of methacrylation, polymer concentration, irradiation time and gradient cooling rate method. At the state of the art, gelMA scaffolds can be used in different field of Tissue Engineering, being possible substitutes of ECM for cell cultures *in-vitro*, but also in

cell signaling and drug delivery. As highlighted in Fig. 9, different techniques can be exploited to process gelMA solutions, such as micromolding, photopatterning, self-assembly, microfluidic, bioprinting, etc., realizing constructs with adequate structure [32]. Moreover, thanks to their biocompatibility and tunable properties, a variety of experiments have been carried out regarding the possibility to mimic different types of tissues (e.g., bone and cartilage) using gelMA hydrogels, as highlighted in Fig. 10 [32]. Furthermore, in order to produce GelMA cell-laden based hydrogels, different pathways have been exploited. For example, gelMA aligned fibers with embedded cells have been created by means of microfluidic approaches, in order to mimic blood vessels or muscle fibers which could provide cells a framework that could affect their orientation [31]. Furthermore, layer-by-layer microfabrication has been reported by exploiting micropatterning methods to realize osteon-like structures, demonstrating that cells were able to recreate the bone's vascular and osteogenic parts. Stereolithography and three-dimensional printing approaches have been also introduced to overcome micropatterning techniques drawbacks (i.e., high cost and time-consuming process) [31]. 3D bioprinting allows to microfabricate several types of constructs with different structure and architecture. Additionally, also materials embedding cells can be used as "bioink". Three-dimensional bioprinting strategies have been exploited to recreate bone tissue, combining gelMA with components which could improve the solution viscosity, such as hyaluronic acid and gellan gum [31]. Moreover, in order to improve gelMA mechanical properties, three-dimensional printing techniques have been exploited to co-deposit thermoplastic materials like poly(caprolactone) (PCL) and gelMA hydrogel (e.g., gelMA fibers bounded by PCL ones) [31]. In order to obtain a bioactive scaffold able to give specific cues to cells, gelMA hydrogels could be combined with inorganic particles (e.g., gold particles and hydroxyapatite), carbon nanomaterials, biopolymers or synthetic polymers. The resulting gelMA blends present specific characteristics which include tailorable mechanical strength, response to temperature and magnetic stimuli, conductivity, bioactivity, controllable porosity, swelling and degradability [28]. For instance, a GelMA hydrogel has been used with magnetic nanoparticles (MNp)

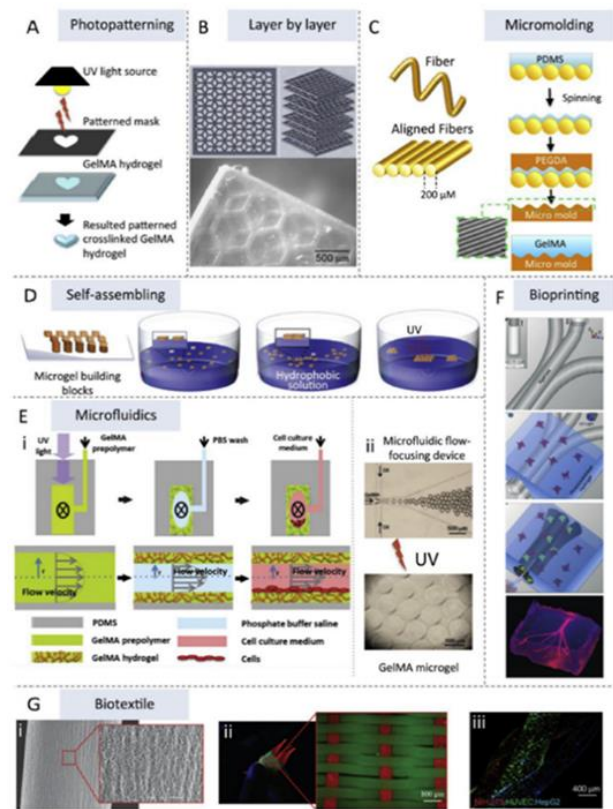


Figure 9: Different microfabrication techniques for gelMA processing [29]

improve the solution viscosity, such as hyaluronic acid and gellan gum [31]. Moreover, in order to improve gelMA mechanical properties, three-dimensional printing techniques have been exploited to co-deposit thermoplastic materials like poly(caprolactone) (PCL) and gelMA hydrogel (e.g., gelMA fibers bounded by PCL ones) [31]. In order to obtain a bioactive scaffold able to give specific cues to cells, gelMA hydrogels could be combined with inorganic particles (e.g., gold particles and hydroxyapatite), carbon nanomaterials, biopolymers or synthetic polymers. The resulting gelMA blends present specific characteristics which include tailorable mechanical strength, response to temperature and magnetic stimuli, conductivity, bioactivity, controllable porosity, swelling and degradability [28]. For instance, a GelMA hydrogel has been used with magnetic nanoparticles (MNp)

which can guide hydrogel self-assembly and cell migration in the three-dimensional structure in a simple and inexpensive way [33]. Furthermore, gelMA combined with other ECM proteins, such as hyaluronic acid (ligand for CD44 receptor) could be used to mimic tumoral microenvironment, allowing the investigation of tumoral cells (which over express CD44) interactions with the extracellular matrix [34].

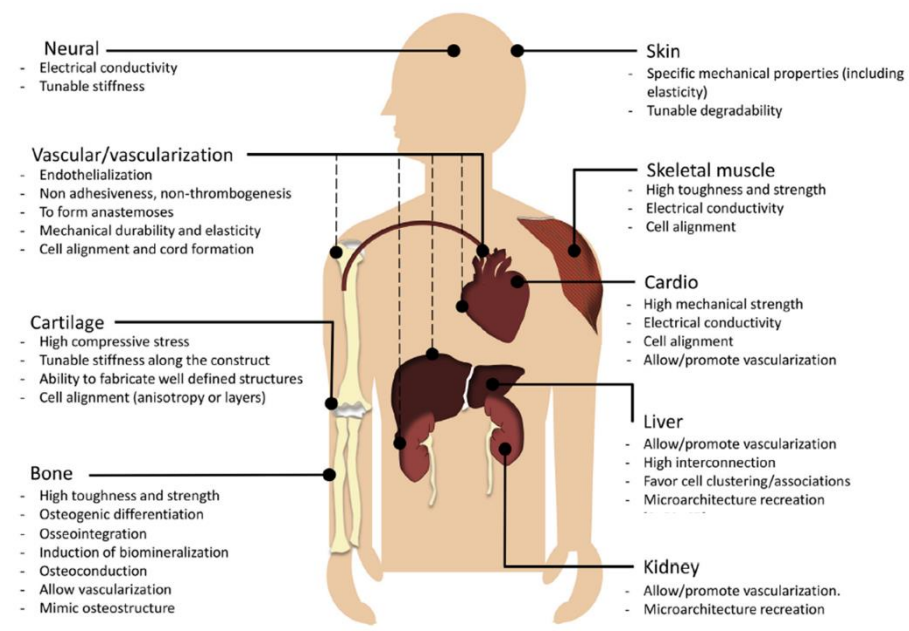


Figure 10: Different types of tissue and properties reproducible with gelMA.

#### 1.4 Hydrogel composite biomaterials

One possible strategy to improve mechanical and chemical properties of hydrogels consists in the addition of a ceramic counterpart in order to exploit their biocompatibility, resistance to corrosion and good compressive modulus. However, these materials alone present disadvantages like high density, fragility, complexity of fabrication, low resistance to fracture and no resilience. Ceramic materials can be divided into ‘inert’, ‘bioactive’ and ‘biodegradable’. Inert ceramics (e.g., alumina and zirconia) do not elicit any inflammatory response, but they are not absorbable, while bioactive ones (e.g., glass ceramics and hydroxyapatite) trigger cellular responses if implanted into the body. Concerning biodegradable ceramics (e.g., aluminum calcium phosphate and coralline), they are resorbed progressively with tissue formation [35]. Recently, bioceramics composite hydrogels have been used in Tissue Engineering applications, mainly in the design of bone substitutes thanks to their osteoconductivity and mechanical properties. Difficult challenges concerning implants, involve the composite degradation rate which must be tailored in order to be matched with tissue growth. Furthermore, porous scaffolds with suitable properties can be realized to culture cells and form a new tissue. For example, polymeric materials such as poly-L-lactide, collagen, gelatin and chitosan are

used in combination with bioceramics like calcium phosphate, hydroxyapatite and tricalcium phosphate for Bone Tissue Engineering applications [35].

### 1.4.1 Gelatin/Hydroxyapatite and gelMA/Hydroxyapatite based hydrogels

Hydroxyapatite (HA,  $\text{Ca}_{10}(\text{PO}_4)_6(\text{OH})_2$ ) is a bioactive bioceramic widely used in Tissue Engineering applications thanks to its osteoconductive properties (it provides a suitable interface where bone tissue can grow), biocompatibility and similarity with the mineral bone component. For these reasons, implants containing this material show a great affinity with bone tissue. Moreover, composite materials based on natural/synthetic polymers and HA are nowadays exploited in cranioplasty and as coatings of femoral and hip prostheses [36],[37]. HA

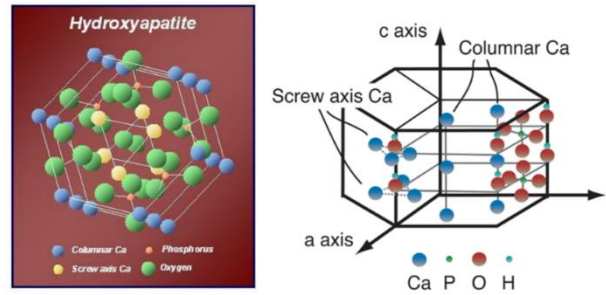


Figure 11: crystal lattice of Hydroxyapatite [34].

is part of the apatites family, having a specific composition and crystal lattice (Fig. 11). HA can be synthesized by three different methods including the wet one, the hydrothermal treatment and solid-state reactions. The resulting final Ca/P molar ratio is usually similar to that of biological HA (i.e., 1.67) [37]. Concerning bioactivity, it depends on the pH of the solution in contact with the implant. The acid pH of physiological environment favors the dissolution of calcium phosphate, causing an increase in the concentration of  $\text{Ca}^{2+}$ ,  $\text{HPO}_4^{2-}$  and  $\text{PO}_4^{3-}$  ions in the solution, with a subsequent hydrate film formation [37]. After this step, the formation of mixed phosphates in the solution, which hydrolyze in the presence of  $\text{CO}_3^{2-}$  (abundant in biological fluids), occurs giving hydroxycarbonate apatite:  $[\text{Ca}_3(\text{PO}_4)_2]_3\text{Ca} [0,4 (\text{OH})_2 0,6 (\text{CO}_3)]$  (Fig.12).

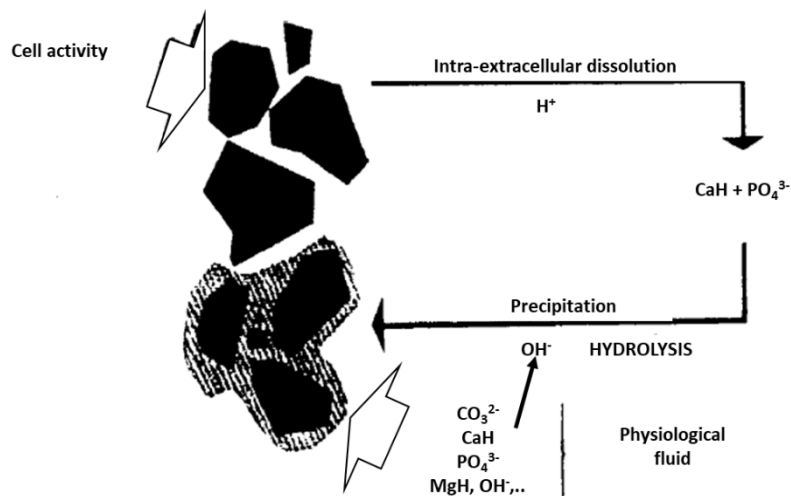


Figure 12: Dissolution/precipitation phenomenon of  $\text{CO}_3^-$  apatite on hydroxyapatite implant in vivo [37].

Hydroxyapatite can be used in porous or dense form, depending on the kind of bone, which has to be substituted. Dense material can be obtained by sintering, uniaxial high pressure or isostatic high

pressure applied on the powders produced through one of the abovementioned methods. Concerning porous hydroxyapatite, it can be fabricated sintering HA powders mixed with organic particles, which will be eliminated by evaporation during the heat treatment. By increasing the temperature of the sintering process, the following properties are improved: density, grain dimension, elastic modulus, resistance to compression, torsion and bending. Unfortunately, the appearance of tricalcium phosphate over 950 °C introduces instability in the ceramic composition, because of tenacity reduction. Sintered HA has superior properties compared to cortical bone, enamel and dentine. However, it is exploited only for coatings and small bone substitutes because of its low resistance to fatigue, which impedes its use as substitute of load bearing bones. Hence, it cannot be applied as substitute of bone defects bigger than 30 mm. For this reason, polymer/nano-hydroxyapatite (nHA) composites are currently investigated. Nowadays, different types of both synthetic (e.g. polylactic acid and polycaprolactone) and natural (e.g. collagen, gelatin, chitosan and fibrin) polymers have been tested in combination with nHA [38]. For instance, different products based gelatin/HA composites have been realized and are currently available on the market in the form of porous scaffolds, hydrogels and fibers, as listed in Tab. 2.

Table 2: collagen and gelatin based materials in the market [39].

Product	Company	Collagen/Gelatin	Additive	Application
Collagraft®	Zimmer	Bovine Collagen Type I (>95%), Type II (<5%)	HAP - 65% β-TCP - 35%	Acute long bone fractures and traumatic osseous defects, bone void filler
GingivAid®	Maxigen Biotech Inc.	Type I collagen	HAP/β-TCP	Dental implant surgeries, sinus lift and alveolar ridge augmentation
Formagraft®	Maxigen Biotech Inc.	Type I collagen	HAP/β-TCP	Bone graft substitute
CopiOs Sponge and Paste	Zimmer	Type I Bovine Collagen	Calcium phosphate	Bone void filler
Ossigen®	Exactech	Collagen	Bone mineral	Bone void filler
OsseoFit®	DSM Biomedical	Type I bovine collagen	PLLA, β-TCP	Bone voids or bone defects in the pelvis and extremities
CONDUCT® Matrix	GLOBUS Medical	Type I collagen	Carbonate apatite mineral	Bone void filler
Puros® DBM Putty	Zimmer	Demineralized bone matrix	-	Bone void filler
CONFORM® Demineralized Cancellous Bone	Depuy Synthes	Demineralized cancellous bone	-	Bone void filler, use within posterolateral gutters of the spine
DBX®	Depuy Synthes	Gelatin-Sodium hyaluronate	Demineralized bone matrix	Bone void filler, treatment of oral/maxillofacial and dental intraosseous defects
Integra Mozaik™	Integra LifeSciences	Type I collagen	TCP	Bone void filler
INFUSE® Bone Graft	Medtronic	Type I bovine collagen	rhBMP-2	Bone void filler
Vitoss®	Stryker	Collagen	β-TCP, Bioactive glass	Bone void filler
OP-1 Implant	Stryker	Type I bovine collagen	BMP-7	Bone void filler
MASTERGRAFT® Putty	Medtronic	Type I bovine collagen	β-TCP	Bone void filler
RegenOss®	JRI Orthopaedics	Type I collagen fibers	Magnesium-enriched HAP	Long bone fractures, Spinal fusion
Orthoss® Collagen	Geistlich Surgery	Porcine Collagen	Bovine HAP	Bone void filler, reconstruction in orthopaedic and in spinal surgery, volume extender for composite bone grafting
Bio-Oss Collagen®	Geistlich Biomaterials	Porcine Collagen	Geistlich Bio-Oss® particles	Sinus Floor Elevation, Peri-Implantitis, Periodontal Regeneration, Ridge Augmentation

Gelatin/HA solutions can be processed to obtain scaffolds by means of different methods, such as freeze-drying, electrospinning, gas foaming, etc.. Hydrogels can even be realized by solution crosslinking exploiting gelatin suitability to physical, chemical or enzymatic cross-linking methods. According to literature, gelatin/HA composites can be enriched with TiO<sub>2</sub> to improve

osteoconductivity, bone formation, cell proliferation and osteogenic differentiation [38]. Concerning gelMA/HA composites, they have interesting properties because of their photoinitiated crosslinking. For this reason, this class of composite hydrogels can be processed to realize scaffolds with desired geometry, mechanical and biological properties.

### 1.5 Rapid prototyping techniques for scaffold production

Concerning scaffold fabrication, many different methods can be exploited including conventional (e.g., solvent casting and particulate leaching, gas foaming, phase separation, etc.) and rapid prototyping techniques (e.g., stereolithography, 3D printing, selective laser sintering, etc.). Unfortunately, conventional methods lack in controllability and repeatability, which make the realization of reproducible structures with adequate degradation and physico-chemical properties (paragraph 1.1) difficult. On the contrary, rapid prototyping techniques (Fig. 13) allow the fabrication

*Table 3: Advantages and drawbacks of some rapid prototyping techniques [41].*

of three-dimensional constructs with precise geometry, starting from data processed by a software CAD (computer-aided design) (Fig. 14). These methods allow the realization of scaffolds which fill perfectly the patient’s defect, starting from data obtained by computerized tomography (CT) and magnetic resonance imaging (MRI). The name rapid prototyping, born in 1980, derives from the ability in realizing complex geometries exploiting a layer-by-layer method, starting from a .STL file, guided by a software. The image is divided into several slices which are progressively created and put together to create a 3D construct starting from a 2D layer. Each layer is linked to the other through a bond or a glue, leading to a final solid scaffold [40].

Methods	Advantages	Disadvantages	Materials	Ref.
SLA, DLP	<ul style="list-style-type: none"> <li>• Manufactured simple and complex</li> <li>• Fast and good resolution</li> <li>• No need for support materials</li> </ul>	<ul style="list-style-type: none"> <li>• Expensive equipment and materials</li> <li>• Only photopolymers</li> <li>• Cytotoxicity of uncured photoinitiator</li> </ul>	PEG, PCL, PEG-co-PDP, PEGDA.	[45–48]
FFF	<ul style="list-style-type: none"> <li>• Easy to use</li> <li>• Good mechanical properties</li> <li>• Solvent not required</li> </ul>	<ul style="list-style-type: none"> <li>• Materials limited to thermoplastics</li> <li>• Filament required</li> <li>• Cannot used with cells</li> </ul>	PCL/PLGA/ $\beta$ -TCP, PCL/PLGA	[50, 51]
SLS	<ul style="list-style-type: none"> <li>• No need for support materials</li> <li>• Various of biomaterials</li> </ul>	<ul style="list-style-type: none"> <li>• Rough surface</li> <li>• Expensive and cumbersome equipment</li> </ul>	PCL/HA, PCL, HA/PEEK, Titanium.	[59–62]
Inkjet	<ul style="list-style-type: none"> <li>• Cells and hydrogel printed</li> <li>• Incorporation of drug and biomolecules</li> </ul>	<ul style="list-style-type: none"> <li>• Limited biomaterials suite</li> <li>• Low resolution</li> <li>• Low mechanical properties</li> </ul>	Collagen/PDL, Fibrin, Gelatin.	[63–65, 68]

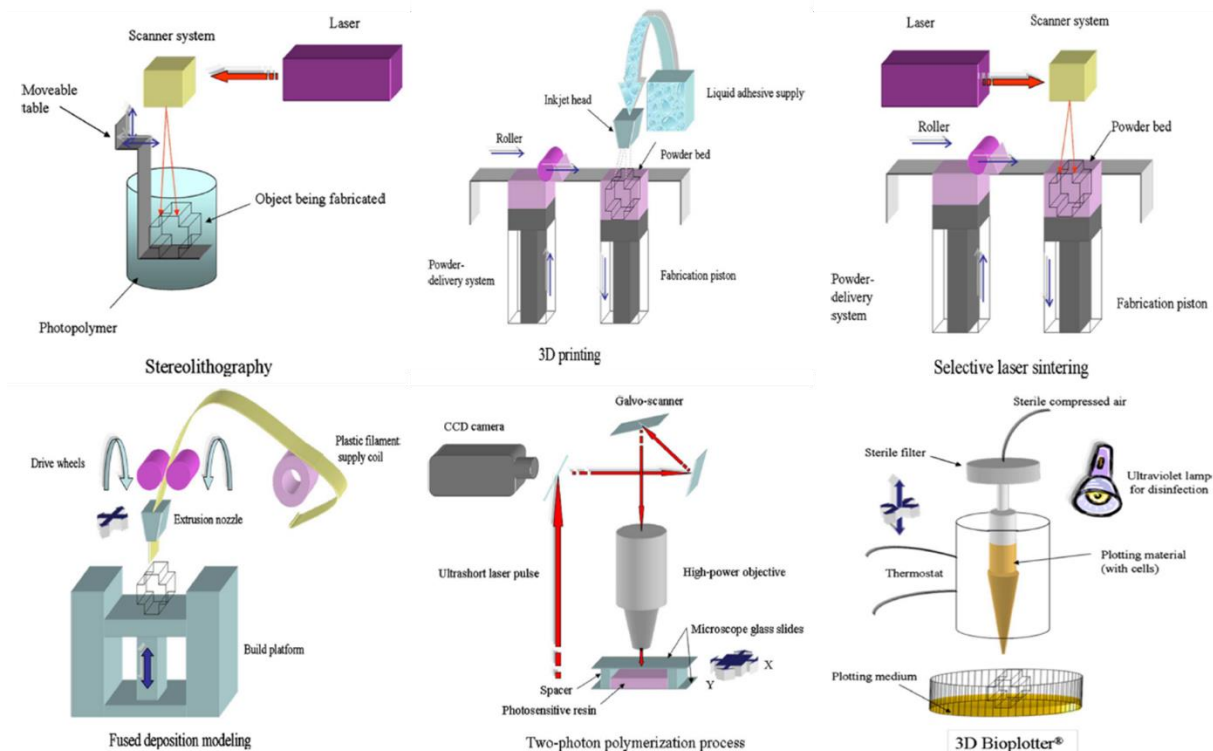


Figure 13: Different types of rapid prototyping techniques [40].

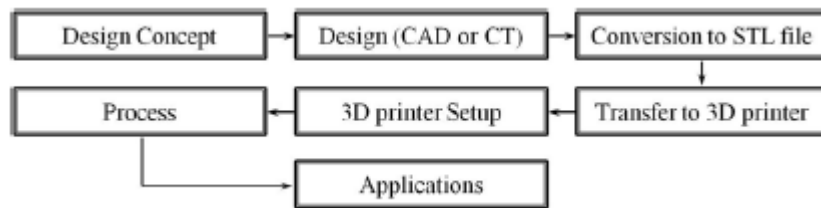


Figure 14: process of 3D printing [42].

### 1.5.1 Three-dimensional printing

Three-dimensional printing (3D printing) is part of the wide family of rapid prototyping techniques and its final aim is the production of a scaffold with precise geometry, shape and porosity. 3D printing includes different techniques, such as stereolithography (SLA), fused deposition modeling (FDM), selective laser sintering (SLS) and solid freeform fabrication (SFF). Each method exploits different energy sources, work parameters and components. SLA uses a UV source to photo-crosslink a polymer resin (added dropwise on the machine basement) layer-by-layer. Instead, in FDM approaches a thermoplastic polymer is melted inside the machine ‘head’ and then extruded in a filament form to create a 3D structure layer-by-layer. Concerning SLS, a laser is used as power source to locally fuse material powder [41]. SFF techniques allow the production of scaffolds with precise geometry, thanks

to the ability to control the xyz positioning of the machine nozzle which deposit the material layers (Fig. 15). Different architectures can be achieved tuning nozzle dimension, temperature, pressure and speed of extrusion. The resolution of the printed constructs is limited by the needle size, the precision of the motion system and material viscosity characteristics. However, solid free form techniques lack of support material, which make material cooling or crosslinking after the extrusion mandatory in order to use them as support for the other layers. on the other hand, SFF printers' cartridges can be filled with both thermoplastics (e.g. polycaprolactone) requiring high temperature to be processed and hydrogels that can be printed at lower temperature. Several scaffolds have been realized with SFF techniques by alternating PCL and alginate fibers, or combining PCL with gelatin methacryloyl [42]. A recently published work reported the realization of 3D printed bone scaffolds based on PCL/hydroxyapatite and cell-laden methacrylated gelatin bioink to investigate the possibility of vascular network production and osteogenic differentiation [43].

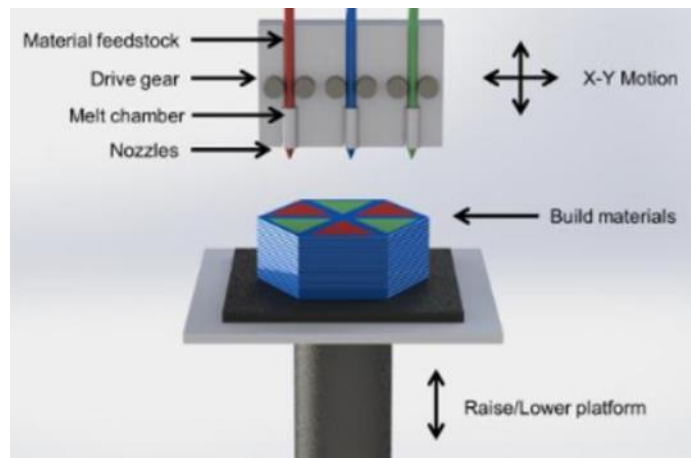


Figure 15: Schematic functioning of Solid Freeform Fabrication technique [43].

### 1.6 Multicomponent scaffolds integrating hydrogels and thermoplastic polymers

Among synthetic polymers used in the biomedical field, thermoplastics like poly-ethylene (PE), polypropylene (PP) and poly( $\epsilon$ -caprolactone) (PCL) have found widespread application. Because of their ability of melting at a specific temperature, these polymers can be modelled to obtain different shapes. Furthermore, they can be exploited as materials for suture wires, but also as matrices for tissue engineering/regenerative medicine applications [44]. Moreover, scaffolds with tunable mechanical properties can be obtained from thermoplastics, because of their ease of processing. For this purpose, different techniques such as electrospinning or fused deposition modeling, can be exploited to realize scaffolds with organized structures. Finally, combining hydrogels with a thermoplastic framework gives the possibility to produce composite scaffolds suitable for new functional tissue formation, such as for osteochondral tissue engineering. Several researches have been carried out concerning the use of rapid prototyping techniques, such as 3D bioprinting, to realize a hydrogel layer on top of a thermoplastic matrix, in order to overcome hydrogel drawbacks of poor shape fidelity and mechanical properties [45]. For example, studies in literature reports the realization of a gelatin/hydroxyapatite/PCL multilayered scaffold for Bone Tissue Engineering application. In this

case a PCL solution was poured on the gelatin/hydroxyapatite layer after solvent (acetone) evaporation [46]. Poly( $\epsilon$ -caprolactone) (PCL) is a thermoplastic polyester widely used in Tissue Engineering applications thanks to its biocompatibility and biodegradability. This polymer is semicrystalline because of its regular structure (Fig. 16) and it possesses a low degradation rate (more than one year), making it suitable for long-term applications. Moreover, glass transition temperature ( $T_g$ ) is around  $-60\text{ }^\circ\text{C}$ , while PCL melting temperature ( $T_m$ ) is between  $59\text{-}64\text{ }^\circ\text{C}$ , thus at physiological temperature it is in the semi-crystalline form. Its semi-crystalline structure allows to obtain good tenacity thanks to presence of amorphous rubbery regions. PCL degradation is achieved by hydrolysis into the body, but because of the presence of hydrophobic  $-\text{CH}_2$  groups, this phenomenon is very slow. For this reason, PCL is mainly used for drug delivery and suture applications. PCL use as blend component or as building block of copolymers opens the way to its application in several TE approaches [47]. For instance, biodegradability, biocompatibility and mechanical properties of PCL can be improved by blending PCL with gelatin. In a different approach, PCL coating with gelatin enhances cell adhesion, migration, growth and proliferation thanks to gelatin characteristic low immunogenicity and the presence of RGD sequences [47],[48]. As reported in literature, gelatin/nHA/PCL electrospun scaffolds could be applied in Dental Tissue Engineering, where nHA particles enhance cell adhesion, odontogenic genes expression and protein absorption [49]. A possible application of gelatin coated PCL scaffolds is the release of biomolecules (e.g., bone morphogenetic protein-2) from gelatin coating to improve bone tissue regeneration [33].

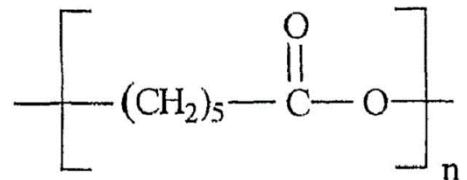


Figure 16: Chemical structure of PCL [41].

## 2. Thesis goal

Taking into account the previously discussed advantages of composite scaffolds, the final aim of this work is the design of thermoplastic/ceramic multi-layered 3D printed scaffolds, physically coupled with gelatin/ceramic based hydrogels. Different forming-materials and fabrication technologies will be exploited to finally obtain a multicomponent scaffold suitable for tissue engineering/regenerative medicine applications (e.g., osteochondral tissue engineering). With regard to the 3D printed scaffolds, commercially available FDA approved poly( $\epsilon$ -caprolactone) ( $M_n=45000$  Da) will be the main constituent of this thermoplastic counterpart because of its biocompatibility, slow degradation rate (i.e., hydrolytic degradation in 2-3 years) and low melting point ( $\sim 60$  °C). This last characteristic is preferred for three-dimensional printing, leading to a better control of the final shape. However, PCL alone is not osteo-inductive. Hence, in order to provide it with osteo-inductive properties, hydroxyapatite (HA) will be added at a weight ratio of 10:90 with respect to PCL. In particular, two types of hydroxyapatite (HA) differing in their shape (i.e., rod-like and spherical shape) will be synthesized through two different precipitation methods, thoroughly characterized in terms of their chemical composition and morphology and finally blended with PCL before scaffold printing. Complete morphological and mechanical characterization of 3D printed structures will be performed by scanning electron microscopy, micro-CT and compression tests. Concerning the hydrogel counterpart of the final device, two different gelatin/HA hydrogels will be explored, differing in the crosslinking mechanism of gelatin (i.e., through glutaraldehyde or by photocuring of gelatin previously functionalized with methacrylate moieties). First gelatin methacryloyl (gelMA) will be synthesized and chemically characterized to assess the success of the synthesis. Then, its hydrogels will be characterized in terms of morphology, swelling capability, mechanical properties and photocuring kinetics. In parallel, gelatin crosslinked gels through glutaraldehyde will be developed and characterized. A protocol for HA homogeneous dispersion within gelatin-based hydrogels will be also optimized. Finally, the physical coupling between hydrogels and PCL/hydroxyapatite structures will be optimized and the resulting multicomponent structures will be characterized to evaluate their morphological and mechanical properties. The work regarding HA and GelMA synthesis, GelMA hydrogel design and the optimization of HA dispersion protocol will be conducted at the Biomedical Laboratory of Politecnico di Torino, meanwhile PCL/HA 3D printing, glutaraldehyde-crosslinked gelatin hydrogel design and hydrogel coupling with 3D printed scaffolds will be performed at the Nanotechnology and Integrated Bioengineering Centre of Ulster University (Jordanstown Campus, Ireland).

### 3. Materials and methods

#### 3.1 Materials

Methacryloyl gelatin synthesis was conducted using gelatin type A from porcine skin (number average molecular weight  $M_n=100000$  g/mol) and methacrylic anhydride ( $M_n=154.16$  g/mol) as reagents, both purchased from Sigma Aldrich, Italy. Lithium phenyl-2,4,6-trimethylbenzoylphosphinate ( $M_n=294.10$  g/mol, TCI Chemicals, Belgium) was used as photoinitiator for hydrogel production. Polycaprolactone/hydroxyapatite based scaffolds required poly( $\epsilon$ -caprolactone) powder with number average molecular weight  $M_n=50000$  g/mol purchased from Polysciences, Inc (Warrington, Pennsylvania). Concerning hydroxyapatite synthesis, phosphoric acid ( $H_3PO_4$ ) and calcium hydroxide ( $Ca(OH)_2$ ), both purchased from Sigma Aldric, Italy, were used as precursors. Concerning gelatin based crosslinked hydrogels, Glutaraldehyde ( $M_n=100.12$  g/mol), purchased from Alfa Aesar (Lancashire, United Kingdom) was used as crosslinking molecule.

#### 3.2 Nomenclature

The abbreviations defined in tab. 4 will be used in the next paragraphs to refer to the here-developed materials and their properties.

Table 4: Abbreviations.

Material	Abbreviation
Methacryloyl gelatin	gelMA
Degree of Methacryloylation	DoM
Methacryloyl gelatin with degree of methacryloylation 67%	gelMA 67%
Methacryloyl gelatin with degree of methacryloylation 74%	gelMA 74%
Gelatin	gel
Hydroxyapatite obtained from rapid mixing method	HA r.m.
Hydroxyapatite obtained from precipitation method at 100°C	HA prec.
poly( $\epsilon$ -caprolactone)	PCL

#### 3.3 Synthesis of methacryloyl gelatin

In this work, two types of gelMAs were synthesized, differing from their degree of methacryloylation, i.e., 67 or 74%. GelMA synthesis was performed according to the protocol reported in [32] and summarized in Fig.1. Briefly, 10 g of gelatin were first dissolved in 100 mL of phosphate buffered

saline (PBS, pH 7.4, Sigma Aldrich, Italy) at 50 °C. Then, methacrylic anhydride (MA) was added drop wise to gelatin solution at 0.16 or 0.25 ml/g<sub>gelatin</sub>, depending on the desired gelMA DoM (adding MA at 0.16 or 0.25 ml/g<sub>gelatin</sub> leads to gelMA with 67 or 74% DoM, respectively). After 3 hours, 500 mL of PBS were added to the mixture to stop the reaction. The reaction mixture was then transferred to a dialysis tube (cut off 12 kDa, Sigma Aldrich, Italy) and dialyzed against deionized water at 37 °C for one week. The dialysis medium was changed twice a day. Finally, the solution was freeze dried (Martin Christ ALPHA 2-4 LSC) to collect GelMA sponges (i.e., GelMA 67% or GelMA 74%), which were then stored under vacuum at 5°C protected from light until use.

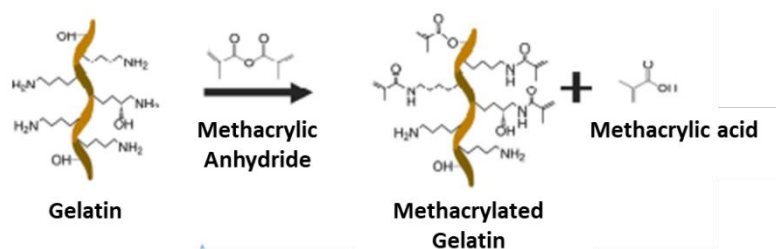


Figure 27: Synthesis of methacrylated gelatin [51].

### 3.4 GelMA Characterization

#### 3.4.1 Attenuated Total Reflectance Fourier Transform Infrared (ATR-FTIR) Spectroscopy

Infrared spectroscopic analysis was conducted to investigate the presence of gelatin and gelMA characteristic peaks in the investigated samples. In detail, in this work Attenuated Total Reflectance Fourier Transform Infrared (ATR-FTIR) Spectroscopy was performed. ATR-FTIR differs from the classical infrared transmission spectroscopy because of the presence of a crystal (made of diamond, ZnSe or Ge) through which the infrared (IR) beam passes. The light beam is directed to the crystal, above on which the sample under study is placed. When the beam hits the crystal, an evanescent wave is generated, that overcomes it. The evanescent wave is absorbed and then attenuated by the sample. Finally, the IR beam reaches the detector (Fig.2). Finally, an infrared spectrum is generated thanks to a Fourier Transform made by the system. Concerning spectra, characteristic peaks appear depending on the composition and kind of bonds present in the material under investigation. Each peak is characterized from a wavenumber (on the horizontal axis) and a width proportional to the number of bonds [52],[53]. In this work, gelMA 67%, gelMA 74% and gelatin (control) were analyzed using a Perkin-Elmer Spectrum 100 in combination with an ATR accessory with diamond crystal. ATR-FTIR spectra were obtained at room temperature in the range

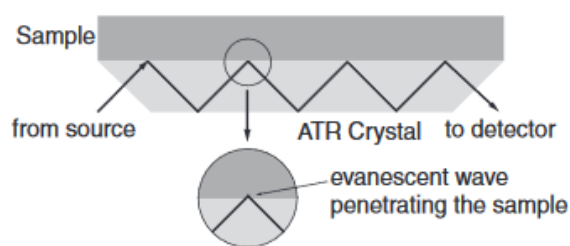


Figure 18: Representation of functioning of an ATR crystal.

between 4000 and 600  $\text{cm}^{-1}$ , as a result of 32 scans with a 4  $\text{cm}^{-1}$  resolution. Spectra analysis was performed using the Perkin-Elmer Spectrum Software.

### 3.4.2 Proton nuclear magnetic resonance spectroscopy

The degree of methacryloylation of the two different kinds of GelMA investigated in this work was determined by Proton Nuclear Magnetic Resonance ( $^1\text{H-NMR}$ ) spectroscopy. In nuclear magnetic resonance spectroscopy signals generated by atoms subjected to a static magnetic field are studied. Each nucleus with spin different from zero is able to provide an NMR signal. Concerning  $^1\text{H-NMR}$  spectra, characteristic peaks derive from elements containing protons. Each nucleus owns a specific frequency resonance, depending on the chemical environment, generating a specific signal. In this way, different molecules and diverse chemical groups can be distinguished in the spectrum. At each peak corresponds a chemical shift in parts per million (ppm), that is the difference between the frequency resonance and the frequency chosen as reference. The area of the peak, also known as intensity of a resonance, is directly proportional to the amount of protons generating the signal [54]. In this thesis work,  $^1\text{H-NMR}$  analyses were performed in deuterated water by means of Avance III bruker spectrometer equipped with a 11.75T superconductor magnet (500 MHz  $^1\text{H}$  Larmor frequency). The  $^1\text{H-NMR}$  spectra were recorded by averaging 12 runs, with 10 sec relaxation time. The signals were referenced to TMS at 0 ppm. Both Gelatin and gelMAs samples were analysed. The phenylalanine signal between 6.9 and 7.5 ppm was taken as reference and used to normalize all the spectra, since this peak is proportional to polymer concentration. The amount of lysine methylene signal ( $\text{NH}_2\text{CH}_2\text{CH}_2\text{CH}_2\text{CH}_2-$ ) at 3,0 ppm has been considered to quantify the number of free  $-\text{NH}_2$  moieties still present after the reaction with methacrylic anhydride [55]. More in detail, these signals (between 2.8 and 2.95 ppm) were integrated in both gelatin and gelMAs spectra in order to obtain their area and the DoM of gelMA samples was calculated applying the following formula [56]:

$$\text{DoM} = 1 - \frac{(\text{lysine methylene proton of gelMA})}{(\text{lysine methylene proton of gelatin})} * 100$$

### 3.4.3 Colorimetric Ninhydrin assay (Kaiser test)

Colorimetric Ninhydrin assay (Kaiser test) was also performed to calculate the degree of methacryloylation in an easier and less expensive way compared to  $^1\text{H-NMR}$  spectroscopy. Kaiser test allows to quantification of free amino groups present in the samples through the measurement of

the absorbance of the complexes that ninhydrin forms with free primary amines. In this work, a Kaiser test kit purchased from Sigma Aldrich, Italy was used to enable the reaction between ninhydrin and gelatin, gelMA 67% or gelMA 74%. After the reaction, each sample was inserted in a quartz cuvette and analyzed by means of a LAMBDA™ 365 UV/Vis Spectrophotometer (PerkinElmer, Italy). A spectrum was obtained from each sample thanks to 21 CFR part 11 software. From Lambert-Beer equation it was possible to calculate the molar concentration of ninhydrin and then the concentration (mmol/g<sub>Gel</sub>) of free amino groups. Thus, from the amount of free -NH<sub>2</sub> in gelMA and unmodified gelatin, in an indirect way, it was possible to obtain the percentage of methacryloylation applying the following formula:

$$\text{DoM} = \frac{\text{NH}_2 \text{ gelatin} \left( \frac{\text{mmol}}{\text{g}} \right) - \text{NH}_2 \text{ gelMA} \left( \frac{\text{mmol}}{\text{g}} \right)}{\text{NH}_2 \text{ gelatin} \left( \frac{\text{mmol}}{\text{g}} \right)} * 100$$

#### 3.4.4 Tube inverting test

Tube inverting test is a simple method used to analyze the sol-gel transition of a solution subjected to a gradual temperature change. In this work, “inverse” tube inverting test was carried out to determine if gelatin methacryloylation could compromise gelatin characteristic physical gelation and in which way the concentration of gelMA can affect gelation temperature. To this aim, gelMA 67% and gelMA 74% solutions with different concentrations (5, 8, 10, 12, 15, 18 and 20% w/v) were analyzed. GelMA solutions were prepared by dissolving the polymer in phosphate buffered saline (PBS, pH 7.4, Sigma Aldrich) so as to reach the previously listed concentrations. Sample solubilization was conducted in incubator at 37 °C. Then the samples were subjected to a controlled temperature change from 37 °C to 17 °C at 1 ± 0.2 °C/step. At each step, the temperature was maintained for 5 minutes and then the samples were observed by inverting the tubes. The samples were considered as a gel when “no flow” was visible with 30 s of tube inversion [57].

#### 3.5 gelMA hydrogel preparation

In this work the capability of gelMA aqueous solutions to form chemically-crosslinked gels when cured with UV light was studied and for this purpose, the effect of photoinitiator concentration was investigated. Lithium phenyl-2,4,6-trimethylbenzoylphosphinate (TCI Chemicals, Belgium) has been selected as photoinitiator for its biocompatibility and ability to enhance cell viability and production of extracellular matrix proteins like glycosaminoglycans *in-vitro* [58]. If sufficient for gelMA curing and able to furnish the desired mechanical properties, a lower concentration of LAP would be

preferred since it is less dangerous for cells. In this study, gelMA gels were realized by photopolymerizing their aqueous solutions at 10 mW/cm<sup>2</sup> and 365 nm in the presence of LAP at two different concentrations (0.5% w/v and 0.05% w/v). Different combinations of gelMA concentration in PBS and LAP were investigated: gelMA 67% at 10% and 15% w/v in PBS, with 0.5% and 0.05% w/v LAP concentration; gelMA 74% at 10% and 15% w/v in PBS, both of them with 0.5% and 0.05% w/v concentration of LAP. For all the selected combinations, circular samples with 10 mm diameter were fabricated by pipetting 200  $\mu$ L of GelMA solution on a glass surface into a metal mold and photocured with UV light at 365 nm for one minute by means of INKREDIBLE+<sup>TM</sup> (CELLINK®).

### **3.6 GelMA hydrogel characterization**

#### **3.6.1 Photorheological analyses**

Photo-rheological measurements were carried out in order to investigate the effect of LAP concentration on gelMA hydrogels crosslinking and the mechanical properties of the resulting gels. Tests were carried on by means of an Anton Paar Modular Compact Rheometer 302 (Anton Paar). GelMA 67% and gelMA 74% (at 10% and 15% w/v concentration) aqueous solution added with LAP at different concentrations (i.e., 0.05%, 0.1% and 0.5% w/v) were analyzed. Each solution was poured on the lower plate of the rheometer and a gap of 0.25 mm was set. Analysis were performed at 20 °C, 1% strain (within the linear viscoelastic region as assessed through strain sweep tests), 1 Hz frequency and normal force set at 0 N. For each sample, after ten minutes of equilibration at the testing temperature, an time sweep test was conducted. Initially, Storage Modulus ( $G'$ ) trend was registered for 1 minute, then the sample was photo-cured by means of UV light (365 nm, 10 mW/cm<sup>2</sup>) for 90 seconds, and finally the sample behavior was registered for other 60 seconds to verify if the mechanical properties were maintained.

#### **3.6.2 Re-swelling test**

In order to investigate the possibility to store lyophilized samples and use them when needed, re-swelling tests were carried out. For this experiment both gelMA 67% and gelMA 74% at 10% and 15% w/v, with LAP at 0.5% and 0.05% w/v concentration were used. After freeze drying, the samples were put in a 24-multiwell plate with 1 mL of PBS (Sigma Aldrich, Italy) and incubated at 37 °C for different time intervals (30 min, 1, 1.5, 2, 3, 4, 5, 6 and 24 hours). Swelling capability was calculated to evaluate the time samples required to recover their original weight and shape. At predetermined time points, the samples were removed from PBS, blotted with filter paper and weighed. Swelling ratio was calculated with the following formula:

$$\text{Swelling ratio} = \frac{w_s - w_d}{w_d}$$

where  $w_s$  is the weight after swelling and  $w_d$  the dry weight.

### 3.6.3 Micro-Computed Tomography ( $\mu$ CT) analyses

Micro-computed Tomography is a non-destructive technique widely used to perform volumetric analyses on small samples, with a micrometric spatial resolution (1 to 50  $\mu$ m). Porosity, morphology and scaffold composition can be easily analyzed thanks to the device functioning principles. As a radiographic technique, X-ray are the energy source which interacts with the material in order to produce a three-dimensional image. To perform the analysis, samples are divided in slices and are gradually irradiated from the bottom to the edge. X-ray are attenuated because of the attenuation coefficient of the specimen and then collected by means of a detector. In this way, a two-dimensional map is created, in which every pixel is related to the attenuation coefficient. The latter is linked to the material density, allowing to observe the different phases in the analysed structures. Finally, a three-dimensional image is created by a specific software which allows to combine the two-dimensional figures [59]. In this work, micro CT analyses have been carried out on different composite based scaffolds in order to observe their morphology, composition and to calculate their porosity and structure thickness. SKYSCAN 1275 X-ray microtomography (Bruker, Maryland) equipment, with a voltage of 40kV and 250 mA current has been exploited to this aim. The X-ray source performed analyses over an angle of 360° with a rotational step of 0.6°/min. Then, scan files were reconstructed by means of NRecon software and the post processing of the 3D image was performed with CTvox software. 3D analyses were carried out on images after NRecon processing, by means of CTan software. In this section, gelMA 67% and 74% based hydrogels (i.e., at concentration of 10% and 15% w/v and 0.05% and 0.5% w/v LAP) were analysed in the dry state.

### 3.7 Hydroxyapatite (HA) synthesis

In this work Hydroxyapatite (HA) nano-powders were synthesized through two simple precipitation methods, where the water is the only by-product of the reaction [60]:



One type of HA was prepared following the protocol developed by Wilcock et al. [61]. This kind of HA will be referred to with the acronym HA r.m.. Instead, the second type of HA, named HA prec., was produced using the precipitation method at 100 °C [61].

### 3.7.1 HA obtained from rapid mix method (HA r.m.)

The protocol developed by Wilcock et al. [60] allows to obtain hydroxyapatite (HA) with a Calcium to Phosphorous molar ratio (Ca/P) of 1.67 from a rapid mixing process (Fig.10). Briefly, 3.795 g of calcium hydroxide were added to 500 mL of deionized water and left under stirring at 400 rpm for one hour, while in another beaker 3.459 g of phosphoric acid (85%) were added to 250 mL of deionized water. Then, phosphoric acid solution was poured into the one containing calcium hydroxide at a rate of almost 100 mL/s. The beaker was covered with Parafilm (Bemis, USA) and the solution stirred for 1 h at 400 rpm. The suspension was left to rest all night. Then, the supernatant was poured off, 500 mL of deionized water were added and the suspension has been left under stirring for 30 minutes. This last step was repeated three times with a gap of two hours. The third time the supernatant was removed after 30 minutes of stirring and the residual suspension was dried at 60 °C. After being dried, nHA was pestled into a mortar and milled. The nHA produced was finally put in an alumina crucible and sintered at 1000 °C for 2 hours with an increasing temperature of 10 °C/min and left cooling down in the furnace [60].

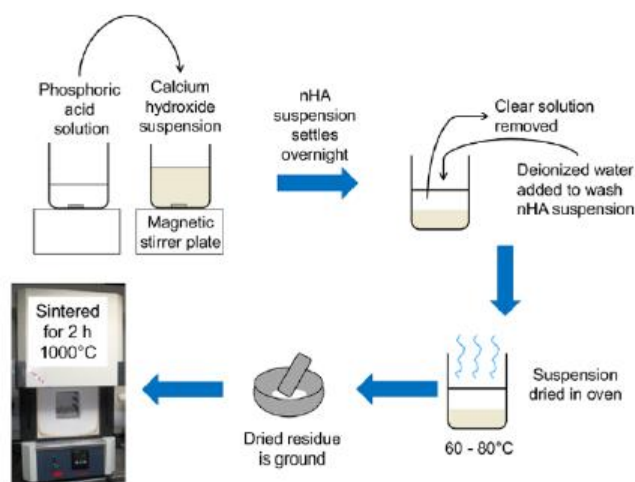


Figure 19: Rapid mix schematic process [60].

### 3.7.2 Hydroxyapatite obtained from precipitation at 100 °C (HA prec.)

HA prec. was obtained through a precipitation reaction carried on at 100 °C. Briefly, 7.41 g of Calcium Hydroxide were added to 500 mL of deionized water in a balloon and stirred at 400 rpm for one hour at 100 °C. Then 6.76 g of phosphoric acid (85%) were dissolved in 500 mL of deionized and the resulting solution was added to the Ca(OH)<sub>2</sub> one at a rate of 4 mL/min. After this step, the resulting reaction mixture was stirred for two hours and left to rest overnight. Then, two washing steps were performed each consisting of pouring off the supernatant, adding 500 mL of deionized water, leaving the dispersion under stirring for 30 minutes and then sedimenting for 2 hours. Finally,

the nano-powder was put in oven at 60 °C to dry. The resulting material was then pestled and grinded in a mortar [61].

### 3.8 Hydroxyapatite characterization

#### 3.8.1 Energy dispersive X-ray (EDX) spectroscopy

Energy dispersive X-ray (EDX) spectroscopy is an analytical technique used to analyze the chemical composition of a sample. Its functioning is based on the study of the interactions occurring between a certain energy source (usually electron or x-ray beam) and the material. Each element has a specific atomic structure, which allows to obtain precise interactions and then, different peaks on electromagnetic emission spectrum. The intensity or area of a peak in an EDX spectrum is relative to the element concentration in the sample. At rest conditions, atoms own electrons in unexcited state in electron shells. If the beam hits an electron, dislocating it, electrons from outer shells of higher energy will fill the hole. Achieving such a “jump”, electrons release energy in X-ray form, equal to the gap between the two states. In this way, the number and energy of the X-rays emitted can be measured by an energy dispersive spectrometer, allowing to obtain the elemental composition of the sample (Fig. 20 [62]). Concerning this work, an EDX analysis has been carried on hydroxyapatite samples in a way to quantify the percentage of calcium and phosphorous to verify if their molar ratio was comparable with the physiological one. Samples were analyzed by means of Leo 1450 MP device with a working distance of 10 mm and accelerating voltage of 20 kV.

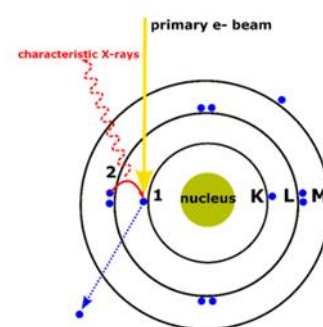


Figure 20: Schematic phenomenon of X-ray production [12].

#### 3.8.2 X-ray powder diffraction (XRD) analysis

X-ray powder diffraction is a nondestructive technique used to characterize structural features at the atomic scale of both organic and inorganic crystalline materials. When X-ray light reflects on any crystal or powder specimen, specific diffraction patterns form reflecting the physico-chemical characteristics of the crystal, thus allowing material identification. In XRD, a monochromatic X-ray beams is focused on the sample to obtain structural information concerning the crystal lattice (Fig. 21 [63]). Materials are composed of repeating uniform atomic planes, which make up their crystal. Typically, polychromatic X-rays are produced in a cathode-ray tube. Polychromatic X-rays are filtered in order to obtain a monochromatic radiation, which hits the material atomic planes, then being absorbed and diffracted by them. The most prevalent type of diffraction is known as Bragg diffraction, defined as the scattering of waves from a crystalline structure. Bragg equation (i.e.,  $2d\sin\theta$

$=n\gamma$ ) correlates wavelength to angle of incidence and lattice spacing, where 'n' is a numeric constant known as the order of the diffracted beam,  $\gamma$  is the beam wavelength, 'd' denotes the distance between lattice planes and  $\theta$  represents the angle of diffracted wave. In this work, XRD analyses were performed on HA powders to assess their crystallinity. The instrument used was a SIEMENS d5005 X-ray diffractometer. Data were collected over the range of  $2\theta= 20-70^\circ$  using a step size and scan rate fixed at  $0.05^\circ$  and  $0.6^\circ/\text{min}$ , respectively (radiation at 40 kV and 40 mA).

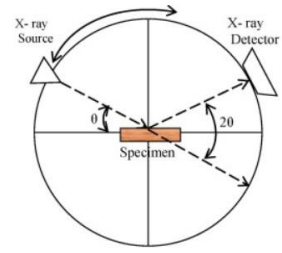


Figure 21: XRD schematic functioning [63].

### 3.8.3 Field Emission Scanning Electron Microscope (FESEM) analysis

Field Emission Scanning Electron Microscopy (FESEM) is a widely exploited technique to investigate material surface structure, topography and composition. Electron microscopies exploit an electron beam instead of a light one, because of its shorter wavelength, which allows to obtain a better resolution (atomic resolution) when observing samples. According to physics, electrons have both a corpuscular and undulatory nature, where the wavelength is relative to the particle momentum. For this reason, if electron beams are accelerated under high voltage, a smaller wavelength can be achieved, allowing to obtain information at the nanometer range. When the electrons hit the sample's surface, they are backscattered or give rise to secondary electrons (with energy lower than 50 eV) which are collected by the detector, allowing the production of a 3D image. Conventional Scanning Electron Microscope (SEM) analysis resolution depends only on the electron probe and on the interaction with the material. Images with high magnification can be obtained from 20 up to 30000 times greater with a spatial resolution of 50-100 nanometers. Concerning FESEM, voltage ranges from 0.5 to 30 kV can be achieved, allowing to give higher acceleration to the electron beam. This phenomenon can be translated in better magnification levels from 10x to 300000x and images with higher resolution, without the necessity to cover samples with conducting materials [64]. In our work, a ZEISS Supra 40 Field Emission Scanning Electron Microscope at 5 kV was used to characterize hydroxyapatite powder morphology.

### 3.9 Hydroxyapatite dispersion in gelMA solutions

In order to create composite gelMA/HA hydrogels with a well dispersed inorganic phase, different dispersing methods were investigated based on literature protocols [65]. For this preliminary optimization, gelMA 67% at 15% w/v concentration in PBS (Sigma Aldrich, Italy) was used with

10% w/v of both types of HA. The sonicator Sonics Vibra-Cells VCX 130 PB (Sonics & Materials, Inc.) was where required.

Investigated dispersion methods:

- 1) The required amount of HA r.m. (i.e., 100 mg) was added to 0.5 mL of PBS and sonicated (at 40% of the sonication device power with a frequency of 20 kHz) for 1 minute. Then, the dispersion was added to 0.5 mL of gelMA solution (at 30%w/v) and left for 15 minutes in a sonication bath at 45 °C;
- 2) The required amount of HA r.m. (i.e., 100 mg) was added to 0.5 mL of PBS and sonicated (at 40% of the sonication device power with frequency of 20 kHz), for 3 minutes. Then, the dispersion was added in 0.5 mL of gelMA solution (30% w/v) and left for 15 minutes in a sonication bath at 45 °C;
- 3) The required amount of HA r.m. (i.e., 100 mg) was added to 0.5 mL of PBS and sonicated (at 40% of the sonication device power with a frequency of 20 kHz), for 10 minutes. Then, the dispersion was added in 0.5 mL of gelMA solution (30% w/v) and left for 30 minutes in a sonication bath at 45 °C;
- 4) The required amount of HA r.m. (i.e., 100 mg) was added to 1 mL of gelMA solution (15% w/v) and left for 15 minutes in a sonication bath at 45 °C;
- 5) The required amount of HA prec. (i.e., 100 mg) was added to a 1mL of gelMA solution (15% w/v) and then left for 15 minutes in a sonication bath at 45 °C;
- 6) The required amount of HA prec. (i.e., 100 mg) was added to 1mL of gelMA solution (15% w/v) and then sonicated (at 40% of the sonication device power with a frequency of 20 kHz) for 1 minute;
- 7) The required amount of HA r.m. (i.e., 100 mg) was added to 1 mL of gelMA solution (15% w/v) and then sonicated for 1 minute (at 40% of the sonication device power with a frequency of 20 kHz);

Starting from each GelMA/HA composite formulation, a circular sample with 10 mm diameter was prepared, freeze dried and analyzed by SEM in order to establish which method allowed the best HA dispersion with GelMA solution.

### **3.9.1 Dispersion stability test**

In order to assess the stability of HA/GelMA dispersions, stability tests were performed on both types of HA and gelMA at different formulations. This aspect is important for further experiments, such as the possibility to print the composite formulations. Concerning gelMA 67%, concentrations of 10% w/v and 15% w/v in PBS were selected and mixed with both types of HA (HA r.m. and HA prec.) at

concentration of 5% w/v and 10% w/v. Each solution was prepared following the previously selected methods. The samples were stored at room temperature and at 37 °C and observed after 10 minutes, 2h and 24 hours storage time. Regarding gelMA 74%, only the stability of formulations containing GelMA 74% at 15%w/v was assessed upon addition of HA at 5 or 10% w/v concentration.

### **3.9.2 Tube inverting test**

A tube inverting test was performed on gelatin and gelMA samples at 15% w/v concentration added with HA (i.e., r.m. and prec.) at 5% and 10% w/v. The study was conducted to assess if hydroxyapatite dispersion could modify the gelation temperature of gelMA in view of future bioprinting applications. Samples were analyzed according to the protocol previously described in paragraph 3.4.4.

### **3.10 Preparation of photo-crosslinked GelMA/HA hydrogels**

Photo-crosslinked hydrogels made up of gelMA and hydroxyapatite were realized with the lowest tested LAP concentration (0.05% w/v). The starting gelMA/HA composite hydrogels were prepared according to the optimized dispersion protocols, and PBS containing LAP at 0.05% w/v concentration was used as solubilization medium. Circular photo-crosslinked gels were prepared as previously described in paragraph 3.5.

### **3.11 gelMA/HA hydrogels characterization**

#### **3.11.1 Attenuated Total Reflectance Fourier Transform Infrared (ATR-FTIR) Spectroscopy**

Attenuated Total Reflectance Fourier Transform Infrared Spectroscopy analysis was performed on gelMA/HA samples to assess the presence of the typical gelatin and hydroxyapatite peaks. Analyses were carried out on freeze dried gels made up of gelMA 67% and gelMA 74% at 15% w/v concentration and hydroxyapatite (i.e., r.m. and prec.) both at 10% and 5% w/v concentration. Samples were investigated with a Perkin-Elmer Spectrum 100 in combination with an ATR accessory with diamond crystal. Spectra were recorded and analyzed according to the protocol reported in paragraph 3.4.1.

#### **3.11.2 Scanning Electron Microscopy (SEM) analyses**

SEM analyses were performed on gelMA/HA samples in order to investigate the dispersion of hydroxyapatite into gelMA hydrogels. Analyses were carried out on gelMA 67% at concentration of 15% w/v with both types of hydroxyapatite at 5% w/v and on gelMA 74% at concentration of 15% w/v with both types of hydroxyapatite at 5% and 10% w/v. In order to investigate hydrogel surface

morphology, internal network, and section, hydrogel circular samples ( $8.9\pm 0.3$  mm diameter,  $1.3\pm 0.2$  mm thickness) were lyophilized, gold coated and finally analyzed using a SEM Leo 1450 MP at 20 kV.

### **3.11.3 Photorheological measurements**

Photo-rheological measurements were conducted on gelMA/HA samples to assess potential effects of hydroxyapatite presence on the photo-polymerization process and the mechanical properties of photo-cured gels. Analyses were performed according to the protocol reported paragraph “Photorheological analysis”. In this study both gelMA 67% and gelMA 74% at concentration of 10% and 15% w/v, combined with both types of HA at 5% and 10% w/v and LAP at 0.05 and 0.5% w/v concentration were tested.

### **3.11.4 Micro-Computed Tomography ( $\mu$ CT) analyses**

In this section, gelMA (i.e. 67% and 74% at concentration of 15% w/v and 0.05% w/v LAP)/ Hydroxyapatite (i.e., r.m. and prec. at 5% and 10% w/v concentration) based hydrogels were analysed in the dry state. Micro CT analyses have been carried out in order to observe their morphology and composition. SKYSCAN 1275 X-ray microtomography (Bruker, Maryland) device, with a voltage of 40kV and 250 mA current has been exploited to this aim. The X-ray source performed analyses over an angle of  $360^\circ$  with a rotational step of  $0.6^\circ/\text{min}$ . Then, scan files were reconstructed by means of NRcon software and the post processing of the 3D image was performed with CTvox software. 3D analyses were carried out on images after NRcon processing, by means of CTan software.

### **3.12 Polycaprolactone/Hydroxyapatite based scaffold fabrication: EnvisionTEC 3D Bioplotter**

Concerning this work, the EnvisionTEC 3D bioplotter technology was exploited to fabricate 3D scaffolds of different compositions. The 3D-Bioplotter™ is a special dispensing machine for fabrication of three-dimensional objects for tissue engineering applications and medical technology. The central process involves dispensing of a viscous material through a thin needle and the subsequent hardening of the material. The layer by layer process allows to obtain 3D structures. The selected material must not change its structural properties after the deposition, e.g. shrinking or swelling when solidifying. Compounds can be deposited in presence of air or liquid medium, where the latter allows to avoid structure deformation but also allows crosslinking reactions. Usually, quick solidifying or highly viscous materials are processed in air (e.g. polycaprolactone), while hydrogels can exploit liquid media. Different needle types, depending on the material viscosity can be used: conical needles,

short straight needles (both preferred for highly viscous materials) and long straight needles (preferred for materials with low viscosity).

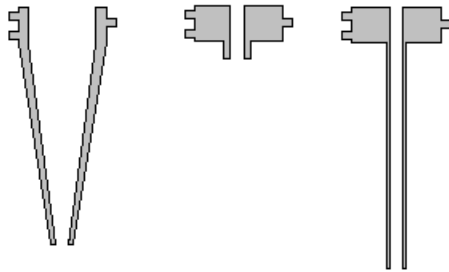


*Figure 22: Needles of different shape exploited for 3D printing.*

Another important printing parameter is the dispense pressure, which is related to the material flow through the nozzle and its consequent hardening. The slower a material hardens, the lower the dispense rate has to be and vice versa. A low dispense rate will allow the material to harden while still being affected by the needle tip, resulting in thinner and rounder strands. Moreover, the dispense pressure has to be tuned even considering the XY movement speed of the device. Different patterns can be designed thanks to the EnvisionTEC software, tuning the strand distance, their orientation and the shift in XY for each layer. Furthermore, dispensing different materials is possible thanks to the automatic tool changing option.

### **3.12.1 The CAD file**

CAD files are required for 3D printing, being this at the basis of the process. CAD software (e.g. Solidworks or SolidEdge) are exploited to create STL files used as input by the printer software. Concerning this work, the 3D printing first step involved the realization of cylindrical structures of 0.7 cm diameter and 0.5 cm height by means of SolidEdge software.

### **3.12.2 The Perfactory RP software**

Concerning the EnvisionTEC's 3D Bioplotter, the Perfactory RP software was exploited to read STL, 3MF and BPL files in order to perform further editing or positioning of the object to print. In this work, the STL file containing the cylindric structure was opened by means of Perfactory RP and then positioned and scaled in a correct way on a virtual building platform (Fig.23, 24).

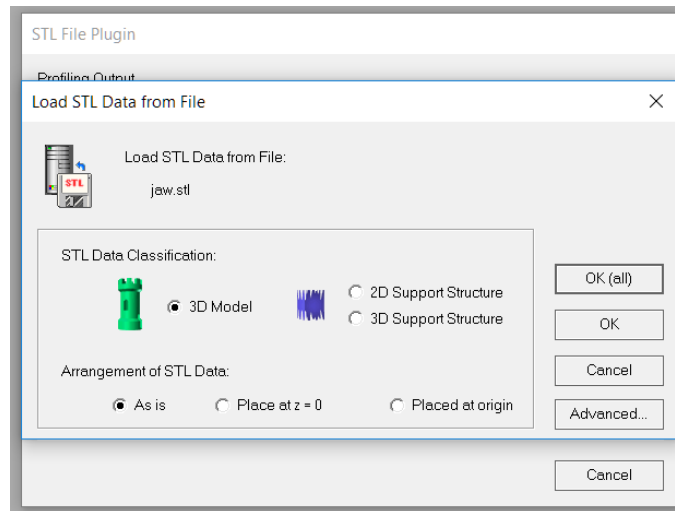


Figure 23: Loading .STL files on Perfactory RP software.

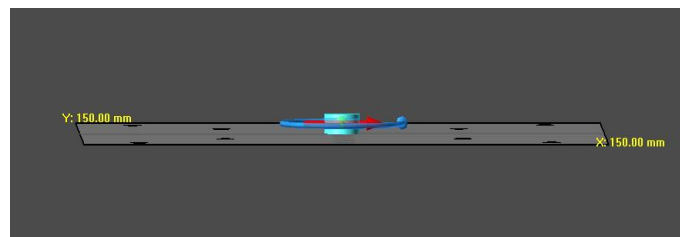


Figure 24: 3D structure positioning and scaling.

Then, structures were sliced (Fig. 25) with the correct layer thickness, which usually is 80% of the needle tip diameter. Concerning our work, a layer thickness of 320  $\mu\text{m}$  was chosen, related to a needle tip inner diameter of 400  $\mu\text{m}$  (22 Gauge needle).

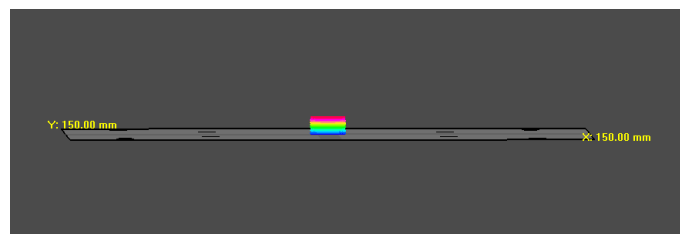


Figure 25: 3D structure slicing.

Finally, the 3D object was built by the “build” function, in order to save the file in the BPL format, which could be read by the Visual Machines software.

### 3.12.3 The printing process

Concerning this work, PCL/HA prec. and PCL/HA r.m. based scaffold were obtained by means of EnvisionTEC’s 3D-bioplotter technology. In order to perform the printing process, different parameters were chosen for both materials. The EnvisionTEC software allowed to define the material

printing properties as highlighted in Tab. 5 (e.g., printing pressure and temperature, XY motion speed, time delay between layers, etc.) and then the printing parameters of the needle (e.g., needle offset, transfer height between layers, etc.) in Fig. 26. Then, a specific inner pattern of the structure was selected (Fig. 26). After having assigned a specific material to the robot head, the device was able to reproduce the cylindrical scaffold (Fig. 27). Concerning the printing process performed in this work, PCL/HA prec. and PCL/HA r.m. constructs were realized using 10% w/w hydroxyapatite with respect to PCL (Mn 45000). A 38  $\mu\text{m}$  sieve was used to achieve a better dispersion of HA before its mixing with PCL. Then, the resulting powder was left under contact mixing overnight before the printing process started. Both materials were poured into a stainless-steel syringe and left at 130°C for 30minutes in order to achieve a homogeneous molten. Additionally, the temperature of 130°C was maintained for the whole printing process. Moreover, since the thermoplastic polymer kept the heat inside its structure, the platform temperature was set at 10°C or 5°C (for HA r.m. and prec. respectively), to achieve a faster dissipation. Furthermore, a delay of 180s was imposed between each printed layer. A 22 Gauge needle with an inner diameter of 400  $\mu\text{m}$  was used, with a XY plane speed of 0.7 mm/s and a pressure of 6.2 bar. The distance between strands was fixed at 600  $\mu\text{m}$ , while their thickness was expected to be 320  $\mu\text{m}$  (i.e., 80% of the needle inner diameter). Moreover, Layer by layer cylindrical scaffolds (diameter 7 mm, height 2 mm) were printed in order to achieve circular grid structure with an open porosity of 60%. Specifically, a repetitive sequence was made up of two orthogonal layers, then followed by two layers shifted of 800  $\mu\text{m}$ .

*Table 5: Printing parameters.*

<b>Material</b>	<b>Pressure [bar]</b>	<b>XY speed [<math>\text{ms}^{-1}</math>]</b>	<b>Printing Temperature [°C]</b>	<b>Platform Temperature [°C]</b>
PCL/HA prec.	6.2	0.7	130	10
PCL/HA r.m.	6.2	0.7	130	5

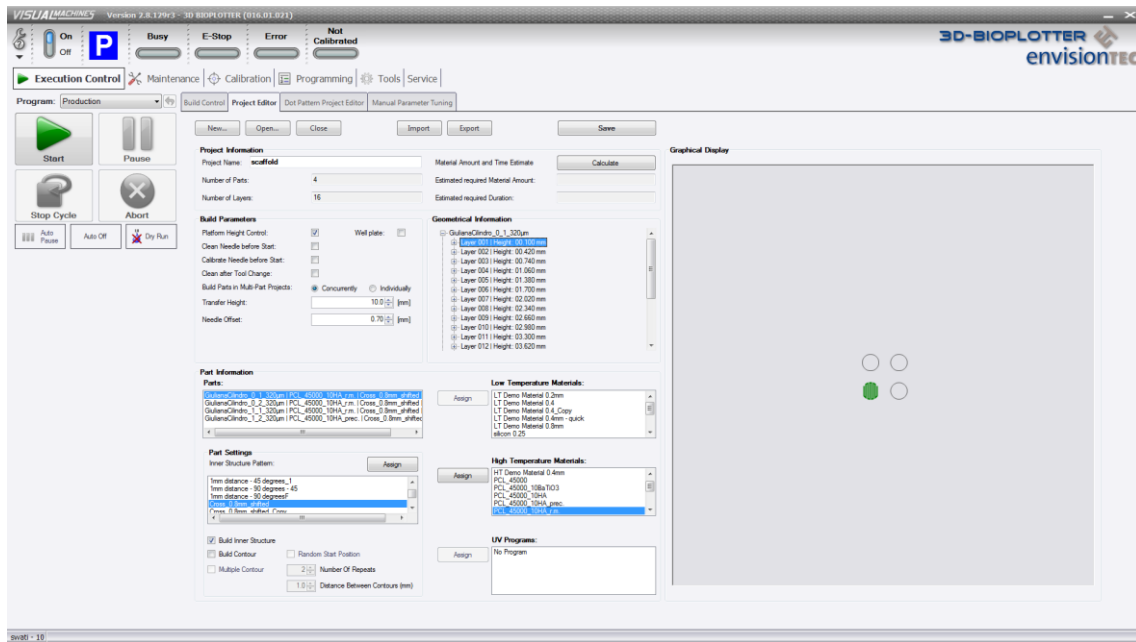


Figure 26: Project pattern parameters.

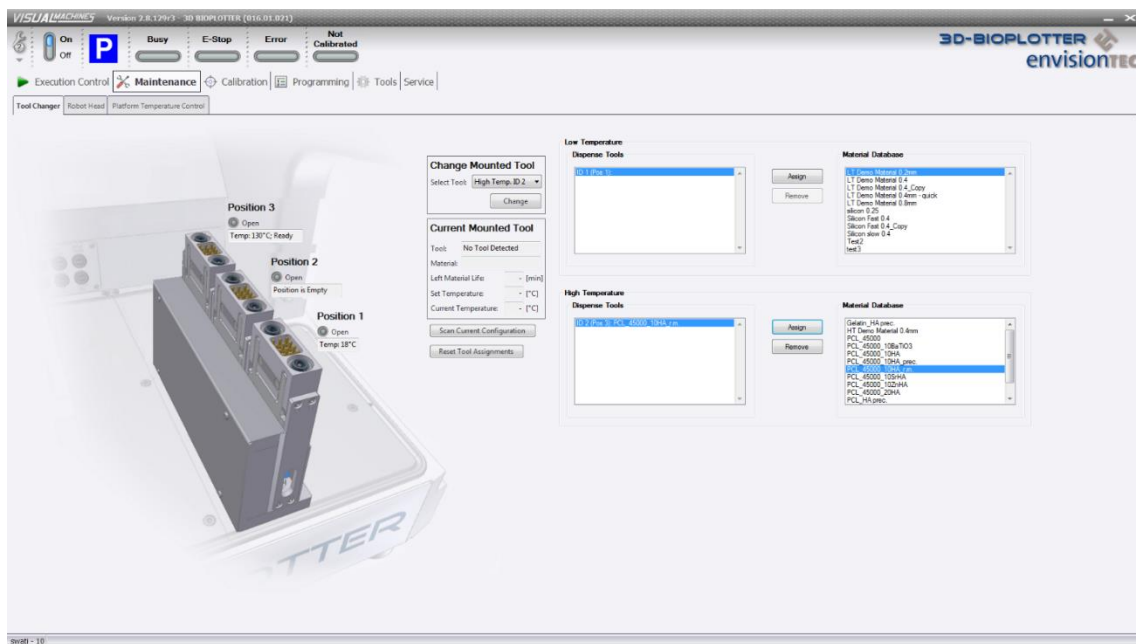


Figure 27: Material assigning to the printing tool.

### 3.13 PCL/HA based scaffold characterization

#### 3.13.1 Attenuated Total Reflectance Fourier Transform Infrared (ATR-FTIR) Spectroscopy

PCL/HA powders were analyzed by means of Attenuated Total Reflectance Fourier Transform Infrared (ATR-FTIR) Spectroscopy, in order to investigate the presence of the characteristic bonds of polycaprolactone and hydroxyapatite (i.e., HA prec. and HA r.m.). To this aim, Nicolet iS5 FTIR Spectrometer (Thermo Fisher Scientific, USA) equipped with an iD5 ATR probe was exploited.

Samples were analysed in the 600-4000  $\text{cm}^{-1}$  range, with a resolution of 4  $\text{cm}^{-1}$  and 30 scan per spectrum.

### **3.13.2 Micro-Computed Tomography ( $\mu$ CT) analyses**

SKYSCAN 1275 X-ray microtomography (Bruker, Maryland) device, with a voltage of 40kV and 250 mA current has been exploited to this aim. The X-ray source performed analyses over an angle of 360° with a rotational step of 0.6°/min. Then, scan files were reconstructed by means of NRecon software and the post processing of the 3D image was performed with CTvox software. 3D analyses were carried out on images after NRecon processing, by means of CTan software. In this section, PCL/hydroxyapatite (i.e., r.m. and prec. at a concentration of 10% w/w) based scaffolds of 0.7 cm of diameter and 0.2 cm height were analysed.

### **3.13.3 Scanning Electron Microscopy (SEM) analyses**

SEM analyses were performed on PCL/HA (i.e., prec. and r.m. at a concentration of 10% w/w with respect to PCL) samples in order to investigate the scaffold surface morphology, internal network, and section. Each sample (7x2 mm) was stored in desiccator after being manufactured and then gold coated before the analysis. SEM images of gold-coated samples were obtained by means of Field Emission Scanning Electron Microscope SU5000 (Hitachi) at 10 kV with a working distance of 5.5 cm.

### **3.13.4 Compressive Tests**

The Elastic Modulus for PCL/HA (i.e., r.m. and prec.) scaffolds was measured using a INSTRON 5500R universal tensile machine (Instron, US) by uniaxial compression tests. The analysed sample size was of 7x5 mm, with a strain rate of 1 mm/min, until achieving a 60% deformation. Young modulus was calculated as the stress/strain ratio (slope of elastic linear region of the stress-strain curve) considering the range between 0.5-1.5% of the strain. To this aim n=5 samples were analysed.

### **3.13.5 Swelling test**

Swelling test were carried out on PCL/HA (i.e., r.m. and prec. at concentration of 10% w/w) in order to use it as control. In this experiment, cylindrical scaffolds of 0.7 cm diameter and 0.2 cm height were exploited. Samples were dried in a desiccator for five days and then put in a 24-multiwell plate with 1 mL of PBS (Sigma Aldrich, Italy) and incubated at 37 °C for different time intervals (30 min, 1, 1.5, 2, 3, 4, 5, 6 and 24 hours). Swelling capability was calculated in a way to understand after how much time the sample reached the plateau region (i.e., achieving the maximum water uptake). At

predetermined time points, the samples were removed from PBS, blotted with filter paper and weighted. Swelling ratio was calculated with the following formula:

$$\text{Swelling ratio} = \frac{w_s - w_d}{w_d}$$

where  $w_s$  was the weight after swelling and  $w_d$  the dry weight.

### 3.14 Preparation of gelatin and gelatin/HA r.m. crosslinked hydrogels

In this work the capability of gelatin and gelatin/hydroxyapatite based hydrogels to form a chemically-crosslinked gel when reacted with glutaraldehyde (GA) solution was studied and, for this purpose, the effect of the dialdehyde concentration was investigated. The presence of glutaraldehyde at two different concentrations (0.25% v/v and 0.3% v/v) was investigated. If sufficient for hydrogels crosslinking and able to furnish the desired mechanical properties, a lower concentration of GA would be preferred since it is less dangerous for cells. Glutaraldehyde is a cross-linking molecule widely used in the biomedical field thanks to its ease of use, low cost, biocidal properties and efficiency even at low, non-toxic concentrations. Moreover, GA is an aliphatic dialdehyde commercialized as aqueous solution of (2%, 25%, 45% and 50% v/v) [66]. Gelatin cross-linking is performed thanks the nucleophilic addition reaction between aldehyde groups of GA and  $\epsilon$ -amino groups ( $-\text{NH}_2$ ) of lysine or hydroxy-lysine in gelatin backbone. To allow this phenomenon, alkaline pH is preferable to avoid amino groups protonation and, consequently, to obtain a major amount of free moieties. As highlighted in Fig.28 the first step of the reaction concerns the nucleophilic addition of free gelatin amino groups to GA carbonyl moieties, then, a conjugated Schiff base forms after the  $-\text{OH}$  protonation [66].

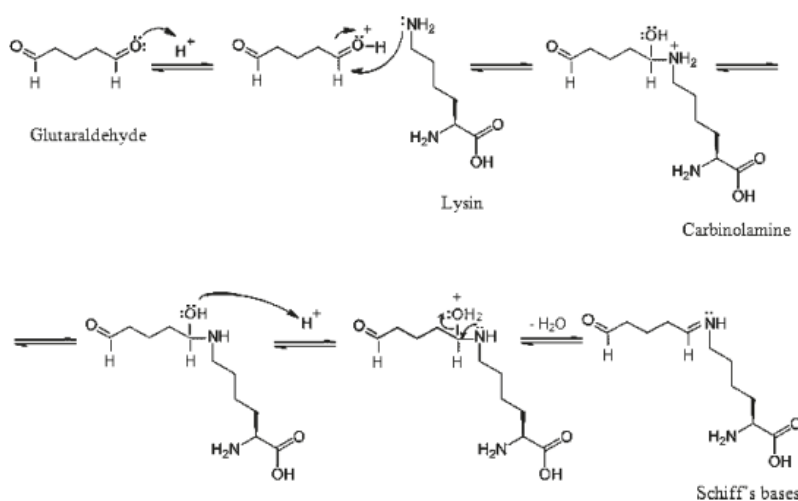


Figure 28: Gelatin crosslinking mediated by glutaraldehyde [66] .

Concerning this work, different combinations of gelatin and gelatin/hydroxyapatite in GA solutions were investigated: gelatin at 15% w/v in PBS and gelatin/hydroxyapatite (i.e., r.m. at 10% w/v in PBS), both of them with 0.25% and 0.3% v/v concentration of GA. For all the selected combinations, circular samples with 1 mm diameter were fabricated by pipetting 200  $\mu$ L of gelatin and gelatin/hydroxyapatite solutions on a 24 well plate then reacted with GA for 1, 3, 5 and 10 minutes. Then, the success of the crosslinking was assessed observing if samples underwent gel-sol transition in incubator at 37°C.

### **3.15 Gelatin and gelatin/HA r.m. hydrogels characterization**

#### **3.15.1 Attenuated Total Reflectance Fourier Transform Infrared (ATR-FTIR) Spectroscopy**

The presence of the characteristic bonds of gelatin and hydroxyapatite in gelatin (i.e., at a concentration of 15% w/v) and Gel/HA r.m. (i.e., at a concentration of 15% and 10% w/v for gelatin and HA respectively) crosslinked hydrogels was investigated by Attenuated Total Reflectance Fourier Transform Infrared (ATR-FTIR) Spectroscopy. Analyses were carried out by means of Nicolet iS5 FTIR Spectrometer (Thermo Fisher Scientific, USA) equipped with an iD5 ATR probe. Samples were analysed in the 600-4000  $\text{cm}^{-1}$  range, with a resolution of 4  $\text{cm}^{-1}$  and 30 scan per spectrum.

#### **3.15.2 Micro-Computed Tomography ( $\mu$ CT) analyses**

Micro CT analysis were carried out on gelatin (i.e., at a concentration of 15% w/v) and Gel/HA r.m. (i.e., at a concentration of 15% and 10% w/v for gelatin and HA respectively) crosslinked hydrogels (i.e., with 0.25% v/v Glutaraldehyde solution) in order to observe their morphology. Moreover, HA r.m. dispersion within gelatin could be thoroughly observed. The same setup as reported in paragraph 3.12.1 was exploited for micro-CT analysis.

#### **3.15.3 Scanning Electron Microscopy (SEM) analyses**

SEM analyses have been performed on Gelatin (i.e., at a concentration of 15% w/v) and Gel/HA r.m. (i.e., at a concentration of 15% and 10% w/v for gelatin and HA respectively) crosslinked hydrogels in order to investigate the surface morphology, internal network, and section. the hydrogel discs (7 $\pm$ 0.3 x 2 $\pm$ 0.2 mm) were lyophilized after being initially frozen and then gold coated. SEM images of gold-coated samples were obtained by means of Field Emission Scanning Electron Microscope SU5000 (Hitachi) at 10 kV.

### 3.15.4 Re-swelling test

In order to investigate the water uptake capability, swelling tests were carried out on of Gelatin (i.e., at a concentration of 15% w/v) and Gel/HA r.m. (i.e., at a concentration of 15% and 10% w/v for gelatin and HA respectively) crosslinked hydrogels (i.e., with 0.25% v/v Glutaraldehyde solution). For this experiment, cylindrical disks of 0.7 cm diameter and 0.2 cm height were used. After lyophilization samples were put in a 24-multiwell plate with 1 mL of PBS (Sigma Aldrich, Italy) and incubated at 37 °C for different time intervals (30 min, 1, 1.5, 2, 3, 4, 5, 6 and 24 hours). Swelling capability was calculated in a way to understand after how much time the sample reached its original weight and the plateau region. At predetermined time points, the samples were removed from PBS, blotted with filter paper and weighed. Swelling ratio was calculated with the following formula:

$$\text{Swelling ratio} = \frac{w_s - w_d}{w_d}$$

where  $w_s$  was the weight after swelling and  $w_d$  the dry weight.

### 3.16 PCL/HA-gel/HA r.m. and PCL/HA-gelMA/HA r.m. multicomponent scaffolds fabrication

Composite scaffolds based on PCL/HA-gel/HA r.m and PCL/HA-gelMA/HA r.m., were realized within this work. The same compositions used in paragraph 3.11.3 and 3.14.1 were exploited for the thermoplastic and hydrogel counterpart. Briefly, cylindrical PCL/HA (i.e., r.m. and prec.) based scaffolds of 0.7 cm diameter and 0.2 cm height were obtained by means of EnvisionTEC's 3D bioplotter, as described in paragraph 3.11.3. A solution of gelatine/HA r.m. (i.e., at a concentration of 15% and 10% w/v for gelatin and HA r.m. respectively) was prepared following the procedure explained in paragraph 3.11.3. Scaffolds were physically coupled, pipetting 100  $\mu$ L of Gel/HA solution on the surface of the PCL/HA scaffold. In order to obtain a cylindrical structure, PCL/HA scaffolds were inserted into a circular mould in which the hydrogel solution was pipetted. Samples were then left at room temperature ( $\sim$ 17-18°C) to allow the hydrogel gelation. Then, concerning the gel/HA based hydrogel, the composite structure was removed from the mould and added to 1mL glutaraldehyde solution (at 0.25% v/v) for ten minutes to perform the chemical crosslinking. Samples were then removed from the GA solution and washed for three times with PBS solution to remove the GA residues. Concerning PCL/HA-gelMA (i.e., 67%)/HA r.m. (i.e., 15% and 10% w/v respectively for gelMA and HA r.m. with 0.05% LAP concentration), the same procedure was carried out to couple the materials, with a different crosslinking strategy. The crosslinking reaction was carried out thanks to the photo-curing mechanism. To this aim, the composite based hydrogels were irradiated by means of UV light (10 W/cm<sup>2</sup>) for 1 minute. The obtained structures (i.e., PCL/HA-

gel/HA r.m and PCL/HA-gelMA/HA r.m.) were finally stored at -80°C for one day and then lyophilized. To investigate mechanical properties, morphology, inner structure and porosity, compressive tests, SEM and  $\mu$ CT analyses were carried out. Swelling ratio was also measured.

### **3.17 PCL/HA-gel/HA r.m. and PCL/HA -gelMA/HA r.m. multicomponent scaffolds characterization**

#### **3.17.1 Micro-Computed ( $\mu$ CT) analyses**

The same setup as reported in paragraph 3.12.1 was exploited for micro-CT analysis. Moreover, the open porosity was calculated at the thermoplastic/hydrogel interface. In this work, different samples were analyzed: gel/HA r.m. (i.e., at concentration of 15% w/v and 10% w/v respectively for gelatin and HA)-PCL/HA (i.e., r.m. and prec. at a concentration of 10% w/w) and gelMA/HA r.m. (i.e., at concentration of 15% w/v and 10% w/v respectively for gelMA and HA)-PCL/HA (i.e., r.m. and prec. at a concentration of 10% w/w) multi-component scaffolds of 0.7 cm diameter and 0.5 cm height.

#### **3.17.2 Scanning Electron Microscopy (SEM) analyses**

SEM analyses have been performed on PCL/HA (i.e., r.m. and prec. at a concentration of 10% w/w with respect to PCL)-gel/HA r.m. (i.e., at concentration of 15% w/v and 10% w/v respectively for gelatin and HA) multi-component scaffolds in order to investigate the surface morphology, internal network, and section. The scaffolds (7 $\pm$ 0.3 x 5 $\pm$ 0.2 mm) were lyophilized after being initially frozen and then gold coated. SEM images of gold-coated samples were obtained by means of Field Emission Scanning Electron Microscope SU5000 (Hitachi) at 10 kV.

#### **3.17.3 Re-swelling test**

In order to investigate the water uptake capability, swelling tests were carried out on PCL/HA (i.e., r.m. and prec. at a concentration of 10% w/w with respect to PCL)-gel/HA r.m. (i.e., at concentration of 15% w/v and 10% w/v respectively for gelatin and HA crosslinked with 0.25% v/v Glutaraldehyde solution) and PCL/HA (i.e., r.m. and prec. at a concentration of 10% w/w with respect to PCL)-GelMA/HA r.m. (i.e., at concentration of 15% w/v and 10% w/v respectively for gelatin and HA with 0.05% w/v LAP concentration). For this experiment, cylindrical disks of 0.7 cm diameter and 0.2 cm height were used. After lyophilization samples were put in a 24-multiwell plate with 1 mL of PBS (Sigma Aldrich, Italy) and incubated at 37 °C for different time intervals (30 min, 1, 1.5, 2, 3, 4, 5, 6 and 24 hours). Swelling capability was calculated in a way to understand after how much time the sample reached its original weight and the plateau region. At predetermined time points, the samples

were removed from PBS, blotted with filter paper and weighed. Swelling ratio was calculated with the following formula:

$$\text{Swelling ratio} = \frac{w_s - w_d}{w_d}$$

where  $w_s$  was the weight after swelling and  $w_d$  the dry weight.

## 4. Results

### 4.1 GelMA characterization

#### 4.1.1 Attenuated Total Reflectance Fourier Transform Infrared (ATR-FTIR) Spectroscopy

The presence of the characteristic bonds of gelatin and gelMA was investigated by Attenuated Total Reflectance Fourier Transform Infrared (ATR-FTIR) Spectroscopy (Fig. 29). Peaks at 3080  $\text{cm}^{-1}$  and 2930  $\text{cm}^{-1}$  represent the stretching vibration of C-H bonds. In gelMA spectra a strong peak at 1633  $\text{cm}^{-1}$  can be appreciated due to C=C bond vibration; however, this peak is overlapped with the characteristic amide I band of gelatin at around 1627  $\text{cm}^{-1}$ . The band between 1500-1570  $\text{cm}^{-1}$  is due to the concurrent C-N stretching and N-H bending vibrations, while that at 3200-3400  $\text{cm}^{-1}$  is due to N-H stretching vibration [67]. However, at about 3290  $\text{cm}^{-1}$  also pendant hydroxyl groups along gelatin backbone show stretching vibration. The peak at 1337  $\text{cm}^{-1}$  can be attributed to the wagging vibration of proline side chains of gelatin, that is usually present in the range of 1260-1400  $\text{cm}^{-1}$  [68].

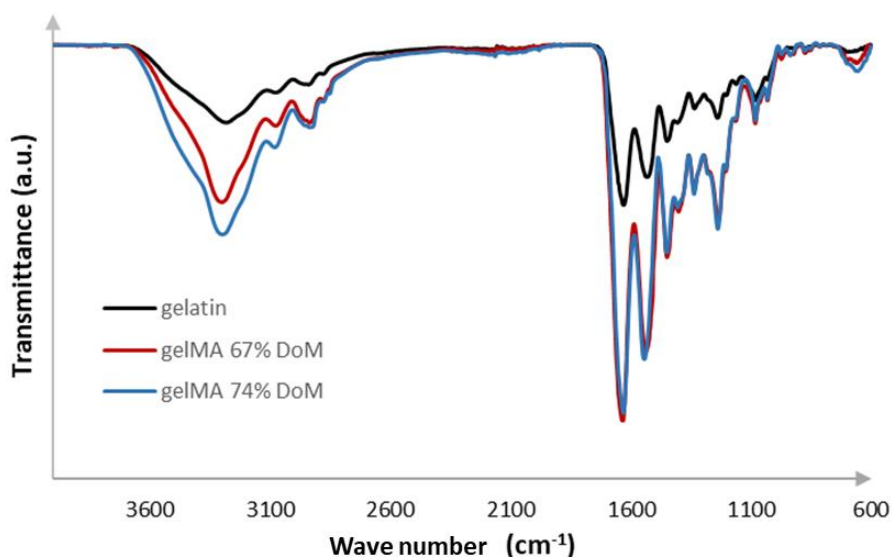


Figure 29: ATR-FTIR spectra of gelatin, gelMA 67% and gelMA 74%.

Hence, the success of the methacryloylation reaction could not be exhaustively assessed through ATR-FTIR spectroscopy since the characteristic peaks of methacrylate groups were overlapped on

those of unmodified gelatin. Nevertheless, , increased intensity at  $3200\text{ cm}^{-1}$  (stretching vibration of pendant hydroxyl groups and N-H bonds),  $1627\text{ cm}^{-1}$  (stretching of C=O and C=C bonds),  $3000\text{ cm}^{-1}$  (stretching vibrations of C-H) and  $1500\text{ cm}^{-1}$  (C-N stretching vibration) indirectly proved the effective grafting of methacryloyl moieties.

#### 4.1.2 Proton nuclear magnetic resonance ( $^1\text{H-NMR}$ )

$^1\text{H-NMR}$  analyses allowed to successfully calculate the Degree of methacryloylation of the two synthesized gelMAs (i.e., with  $0.16$  and  $0.25\text{ ml}_{\text{methacrylic anhydride}}/\text{g}_{\text{gelatin}}$ ), showing that the addition of different amounts of methacrylic anhydride to gelatin solution led to different DoM values. Moreover, comparing  $^1\text{H-NMR}$  spectra of gelatin and gelMA, new peaks appeared in gelMA spectra in addition to the characteristic ones of gelatin, proving the success of the methacrylation reaction (Fig.30): chemical shifts between  $5.7\text{--}5.6$  and  $5.5\text{--}5.4$  ppm can be ascribed to acrylic protons ( $\text{CH}_2=\text{C}(\text{CH}_3)\text{CONH}$ ) of methacrylamide groups, while the signal at  $1.9$  ppm is due to the methyl protons ( $\text{CH}_2=\text{C}(\text{CH}_3)\text{CO-}$ ) of methacryloyl groups. Lysine methylene signal ( $\text{NH}_2\text{CH}_2\text{CH}_2\text{CH}_2\text{CH}_2\text{-}$ ) at  $3.0$  ppm decreased in gelMA samples compared to gelatin control because of the reaction of its lateral chain with methacrylic anhydride [55]. The degree of methacryloylation of the two synthesized polymers resulted to be  $67\%$  and  $74\%$ , according to the amount of methacrylic anhydride added during the synthesis (i.e.,  $1.6$  and  $2.5\text{ ml}_{\text{methacrylic anhydride}}/\text{g}_{\text{gelatin}}$  led to gelMA  $67\%$  and gelMA  $74\%$ , respectively).

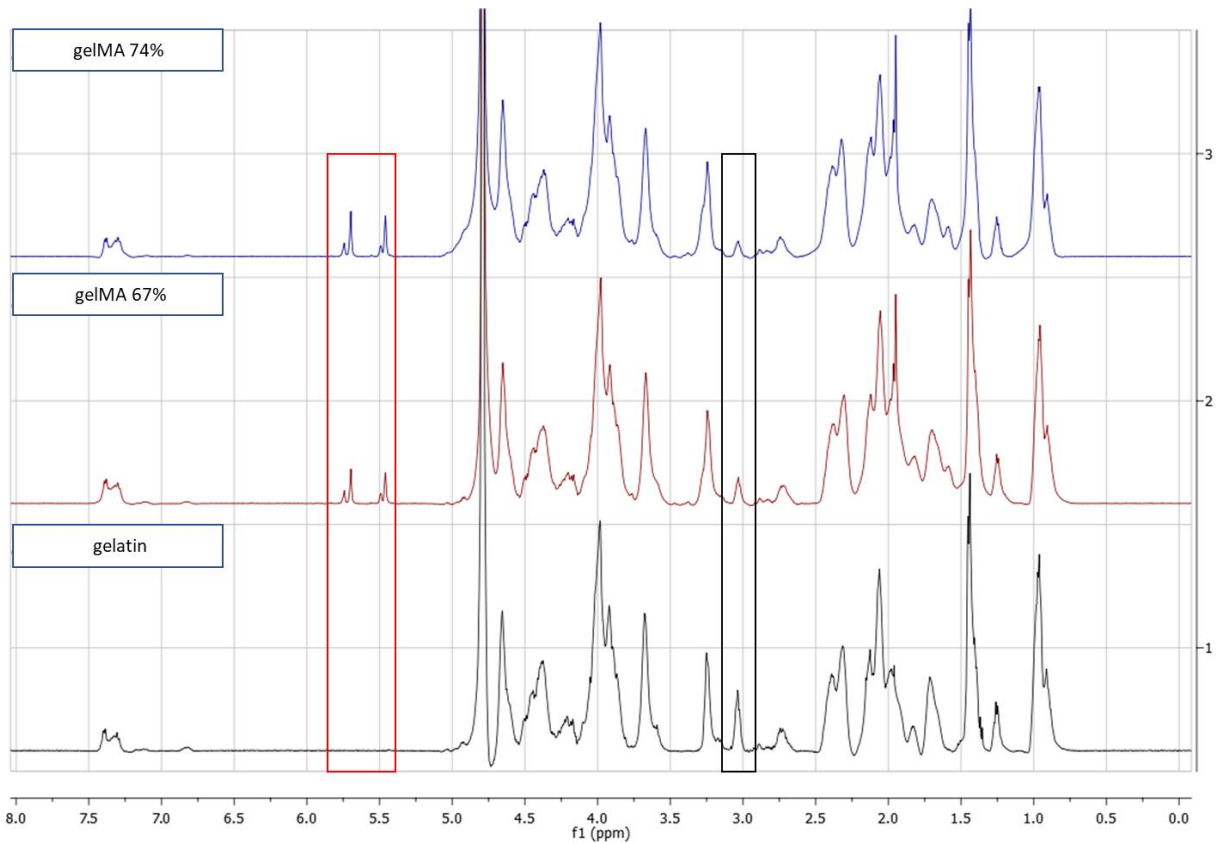


Figure 30:  $^1\text{H-NMR}$  spectra of gelatin, gelMA 67% and gelMA 74%.

#### 4.1.3 Ninhydrin colorimetric assay (Kaiser test)

DoM obtained thanks to Kaiser test resulted to be  $76 \pm 1.1 \%$  for gelMA 67% and  $81 \pm 1.8 \%$  for gelMA 74%. Visual inspection clearly highlighted that with increasing GelMa DoM samples exhibited lower shading towards blue/violet color compared to gelatin as such (Fig. 31). The poor variability of the obtained results (as suggested by the small standard deviations) indicates that the test is highly repeatable (Fig. 32).

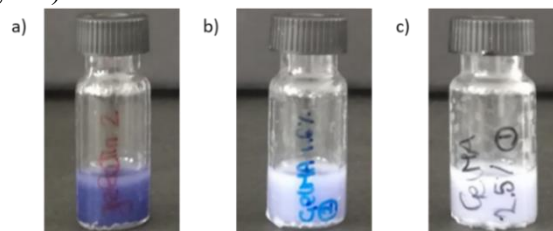


Figure 31: Sample appearance after Kaiser test: a) gelatin, b) gelMA 67%, gelMA 74%.

By comparing the obtained results with  $^1\text{H-NMR}$  data, the error made with the Kaiser test is about 10-12% for both gelMA 67% and gelMA 74% (Fig. 32).

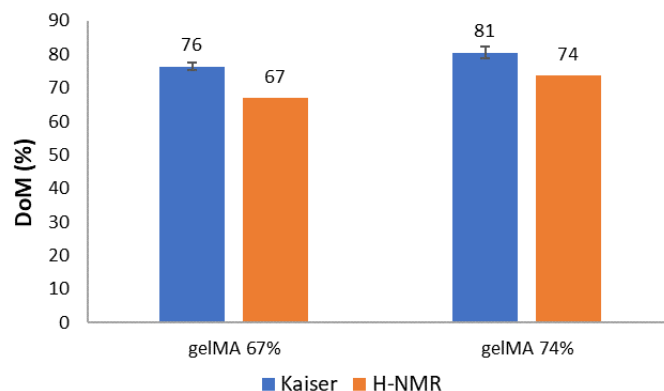


Figure 32: DoM calculated from Kaiser test and <sup>1</sup>H-NMR spectra.

#### 4.1.4 Tube inverting test

Gelation temperature of gelatin and gelMA (67% and 74%) aqueous solutions is reported in Fig.33. As expected, with decreasing gelMA 67% and 74% concentration (% w/v) a decrease in gelation temperature was observed, as highlighted in Fig. 6. Indeed, with decreasing polymer concentration, a lower amount of dispersed chains was present in the solution and, for this reason, the UCST mechanism of gel formation was hindered because of the higher distance between chains. In order to allow chains to pack in a gel network, lower temperature were required at which the bonding between intraoligomer hydrogens could take place and the transition from random coils to single helices occurred. These single helices reorganized themselves until reaching an equilibrium state, forming a gel network [69]. No differences between gelMA 67% and gelMA 74% were observed in terms of gelation behavior. However, both GelMAs showed slight decreased gelation temperature with respect to gelatin as such (at 15%w/v concentration, gelatin and GelMA exhibited gelation temperature of 28 and 25 °C, respectively). This phenomenon can be correlated to the steric hindrance due to the side-chain modification in gelMAs, which hinders triple helix assembly.

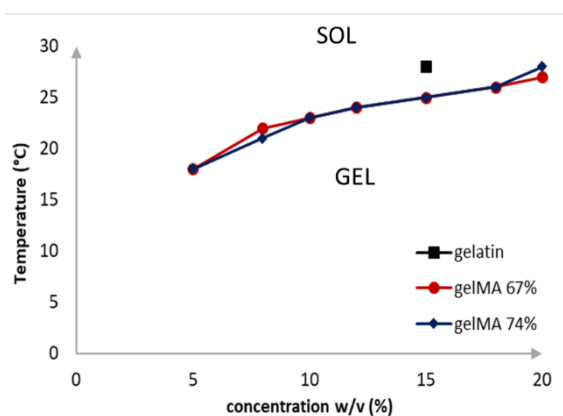


Figure 33: Tube inverting test of gelatin at 15% w/v, and gelMA (GelMA 67% and gelMA 74%) at different concentrations within 5 and 20% w/v.

## 4.2 GelMA hydrogel characterization

### 4.2.1 Photo-rheological characterization

Concerning gelMA hydrogels as such (i.e., without HA) (Fig. 34) higher storage modulus values and faster crosslinking rates were observed with increasing LAP concentration. Another difference was present between gelMA gels with 10% and 15% w/v polymer concentration, with the latter reaching higher storage modulus values, as expected (Fig.35 and Fig.36).

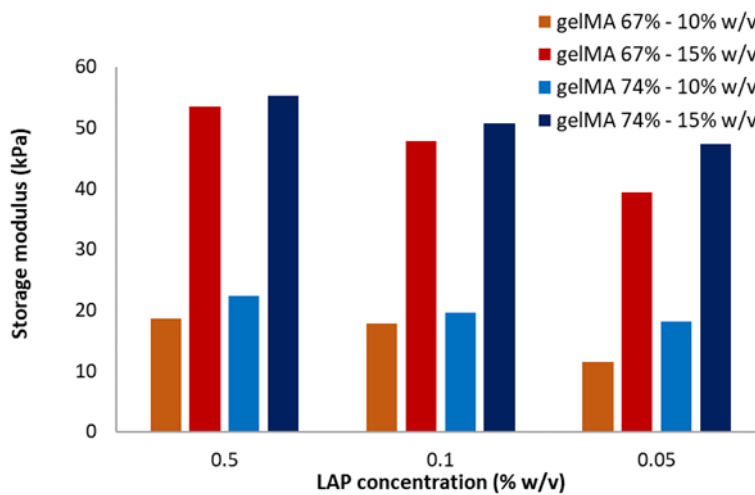


Figure 34: Storage moduli of gelMA after photo-curing.

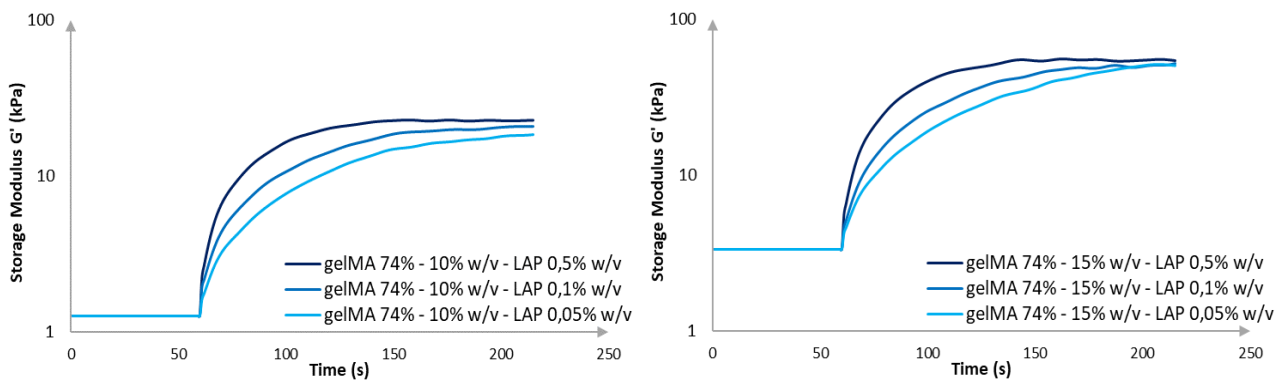


Figure 35: Storage modulus trend of gelMA 74% sample before, during and after photo curing as assessed through time sweep tests. GelMA concentration was fixed at 10 and 15% w/v, while LAP concentration ranged between 0.01 and 0.5% w/v.

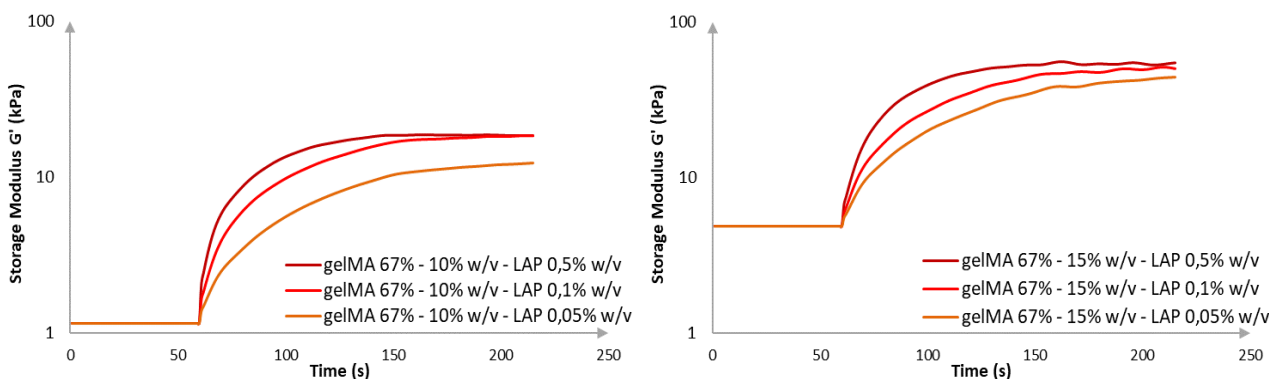


Figure 36: Storage modulus trend of gelMA 67% sample before, during and after photo curing as assessed through time sweep tests. GelMA concentration was fixed at 10 and 15% w/v, while LAP concentration ranged between 0.01 and 0.5% w/v

#### 4.2.2 Re-swelling test

Fig. 37 reports the trend of swelling ratio overtime for all the analyzed samples. For both types of gelMA gels a plateau of swelling ratio parameter was reached after a maximum of 5h incubation in PBS. Additionally, at this time point, all the samples gave back to their original form and weight (Fig. 48).

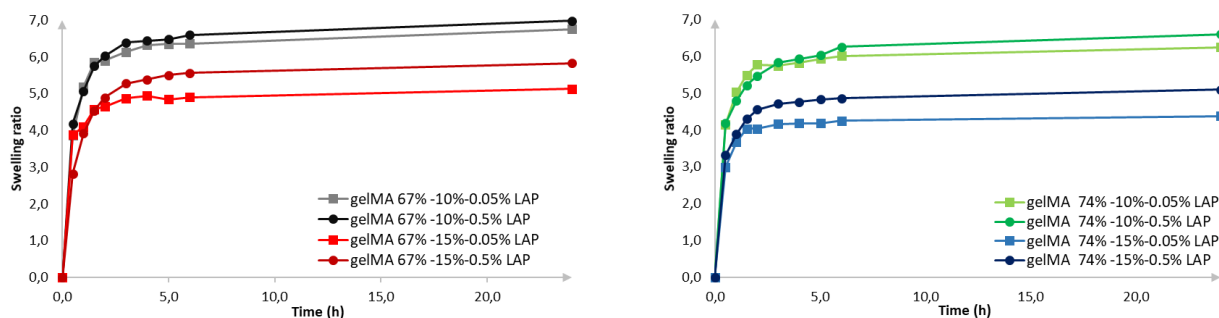


Figure 37: Swelling ratio of a) gelMA 67% and b) gelMA 74% gels.

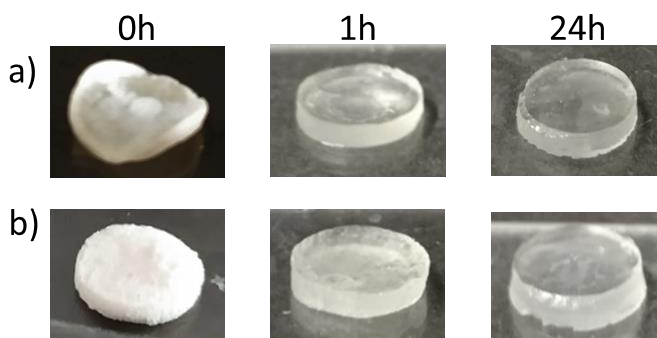


Figure 38: Images of a) gelMA 67% and b) gelMA 74% gels after incubation in PBS of different time intervals.

### 4.3 Hydroxyapatite characterization

#### 4.3.1 ATR-FTIR analyses on hydroxyapatite powders

Attenuated Total Reflectance Fourier Transform Infrared Spectroscopic analyses of both types of HA (i.e., HA r.m. and HA prec.) demonstrated the successful synthesis of hydroxyapatite nanopowders. HA r.m. ATR-FTIR spectrum (Fig. 39) showed the characteristic peaks of phosphate ( $\text{PO}_4^{3-}$ ) and hydroxyl groups ( $\text{OH}^-$ ). Specifically, the peak at  $3570\text{ cm}^{-1}$  can be ascribed to the  $\text{OH}^-$  stretching vibration ( $\nu\text{OH}^-$ ), while peaks at  $1072\text{ cm}^{-1}$ ,  $1028\text{ cm}^{-1}$ ,  $964\text{ cm}^{-1}$  and  $605\text{ cm}^{-1}$  can be attributed to  $\text{PO}_4^{3-}\nu_3$ ,  $\text{PO}_4^{3-}\nu_2$ ,  $\text{PO}_4^{3-}\nu_1$ , and  $\text{PO}_4^{3-}\nu_4$  stretching, respectively. Regarding unsintered HA r.m. other peaks were identified due to the presence of residual water molecules (band peak at around  $3330\text{ cm}^{-1}$ ), and to  $\text{CO}_3^{2-}\nu_3$  ( $1430\text{ cm}^{-1}$ ,  $1410\text{ cm}^{-1}$ ) and  $\nu_2$  ( $862\text{ cm}^{-1}$ ) stretching. With sintering, water and carbonate groups were eliminated and a more crystalline product was obtained. Increase in crystallinity was also highlighted by hydroxyl- and phosphate-related peaks sharpening. Unsintered HA r.m. underwent B-type carbonate substitution, where the latter takes the place of  $\text{PO}_4^{3-}$ . This kind of substitution is typical in young bones, while A-type substitution (carbonate ions instead of hydroxyl groups) is mainly present in old bones. B-type substitution could cause a diminished crystallinity and thermal stability, but a higher nHA solubility [60].

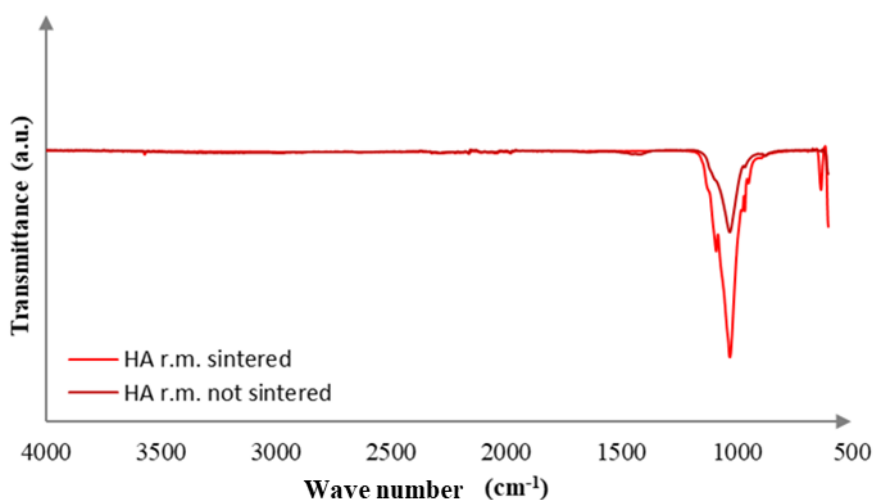


Figure 39: FTIR spectra of HA r.m. sintered and not sintered.

Concerning HA prec. ATR-FTIR spectrum (Fig. 40), peaks linked to phosphate and hydroxyl groups typical of hydroxyapatite phase were found, such as illustrated in literature [61]. Even in this case, the reaction temperature of  $100^\circ\text{C}$  allowed the B-type substitution. Finally, the peak at  $3567\text{ cm}^{-1}$  was related to  $\text{OH}^-$  stretching, while the ones at  $3485\text{ cm}^{-1}$  and  $1633\text{ cm}^{-1}$  were linked respectively to  $\text{H}_2\text{O}$  stretching and bending. B-type substitution was confirmed by  $1454\text{ cm}^{-1}$ ,  $1416\text{ cm}^{-1}$  ( $(\text{CO}_3)^{2-}\nu_3$  stretching) and  $876\text{ cm}^{-1}$  ( $(\text{CO}_3)^{2-}\nu_2$  stretching) peaks. Phosphate peaks were at  $1022\text{ cm}^{-1}$  ( $\text{PO}_4^{3-}\nu_3$

stretching) and  $630\text{ cm}^{-1}$  ( $\text{PO}_4^{3-}$   $\nu_4$  stretching). Generally,  $\text{CO}_3^{2-}$  ions appearance could come from  $\text{CaCO}_3$  impurities in the reactants and  $\text{CO}_2$  in the atmosphere [70].

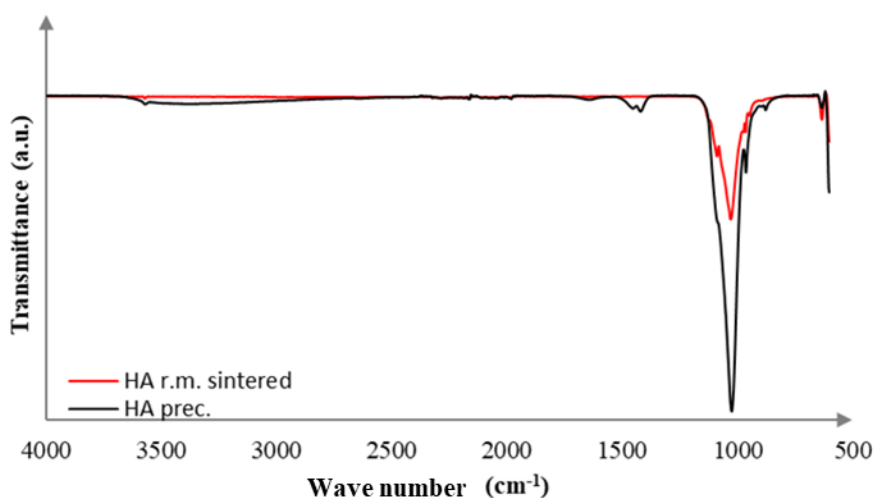


Figure 40: FTIR spectra of HA r.m. and HA prec..

#### 4.3.2 XRD analyses

HA characterization with XRD confirmed that both HA prec. and HA r.m. were well crystallized and that crystalline hydroxyapatite was successfully synthesized with both the adopted protocols (Fig. 41). Moreover, the absence of Calcium Hydroxide precursor was assessed.

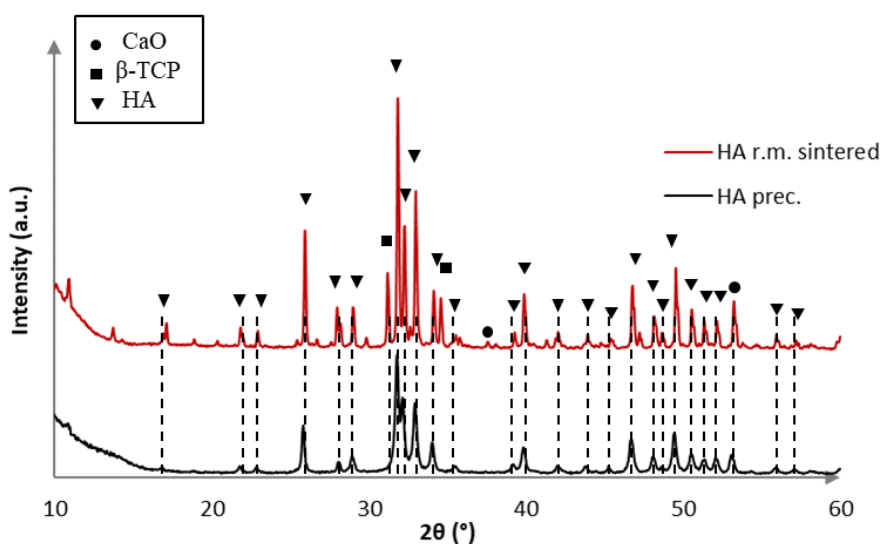


Figure 41: XRD spectra of HA r.m. sintered and HA prec.

Concerning HA obtained from rapid mixing method, XRD analyses were performed before and after sintering. As reported in literature, the fast addition (i.e., within approx. 2.5 s) of phosphoric acid to the reaction mixture allowed the formation of hydroxyapatite thanks to pH modification. The peaks

on XRD spectrum revealed the precipitation of pure hydroxyapatite with small amorphous crystals. With the increasing temperature during the sintering process, the formation of  $\beta$ -tricalcium phosphate ( $\beta$ -TCP) occurred [60]. At the same time, observing the XRD spectra, as shown in Fig. 19, more peaks related to HA appeared after sintering. Moreover, these peaks were sharper if compared with the ones of the unsintered hydroxyapatite. This latter phenomenon was related to the increasing crystallite size after the sintering process [60].

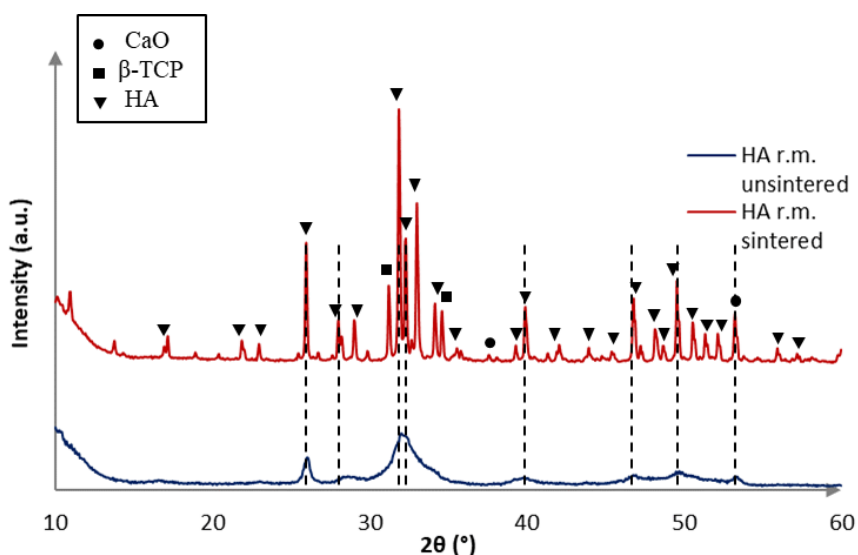


Figure 42: XRD spectra of HA r.m. sintered and HA r.m. unsintered.

As regards HA obtained with precipitation method at 100 °C, beside the HA related peaks, a low amount of  $\beta$ -TCP was observed (peaks between 30°-31°). With increased reaction temperature, the crystallite size was improved and, as a consequence HA crystallinity [61]. This phenomenon is noticeable with the appearance of sharper peaks if compared with HA r.m. unsintered (obtained from precipitation reaction at room temperature) spectrum.

#### 4.3.3 EDX analyses

Elemental analysis was carried out on HA r.m. (before and after sintering) and HA prec. using energy-dispersive X-ray spectrometry (EDX) with the aim to calculate Ca:P ratio (Fig. 43, 44, 45). The literature reports that stoichiometric hydroxyapatite has Ca:P ratio equal to 1.67; however it is reported that Ca:P ratio of bone-apatite lays in the range between 1.37 and 1.87 [71]. Values similar to that of stoichiometric hydroxyapatite were obtained from all the analyzed samples. As highlighted from data gathered from EDX analyses showed in Tab.6, HA r.m. was characterized by a Ca:P ratio of 1.69 and 1.66 before and after sintering procedure, respectively, indicating the formation of a calcium deficient hydroxyapatite, probably due to the rapid pouring of phosphoric acid solution into

the calcium hydroxide one, which allowed a faster HA precipitation. Concerning HA prec., a Ca:P ratio of 1.87 was obtained, probably due to the local presence of carbonated apatite compounds.

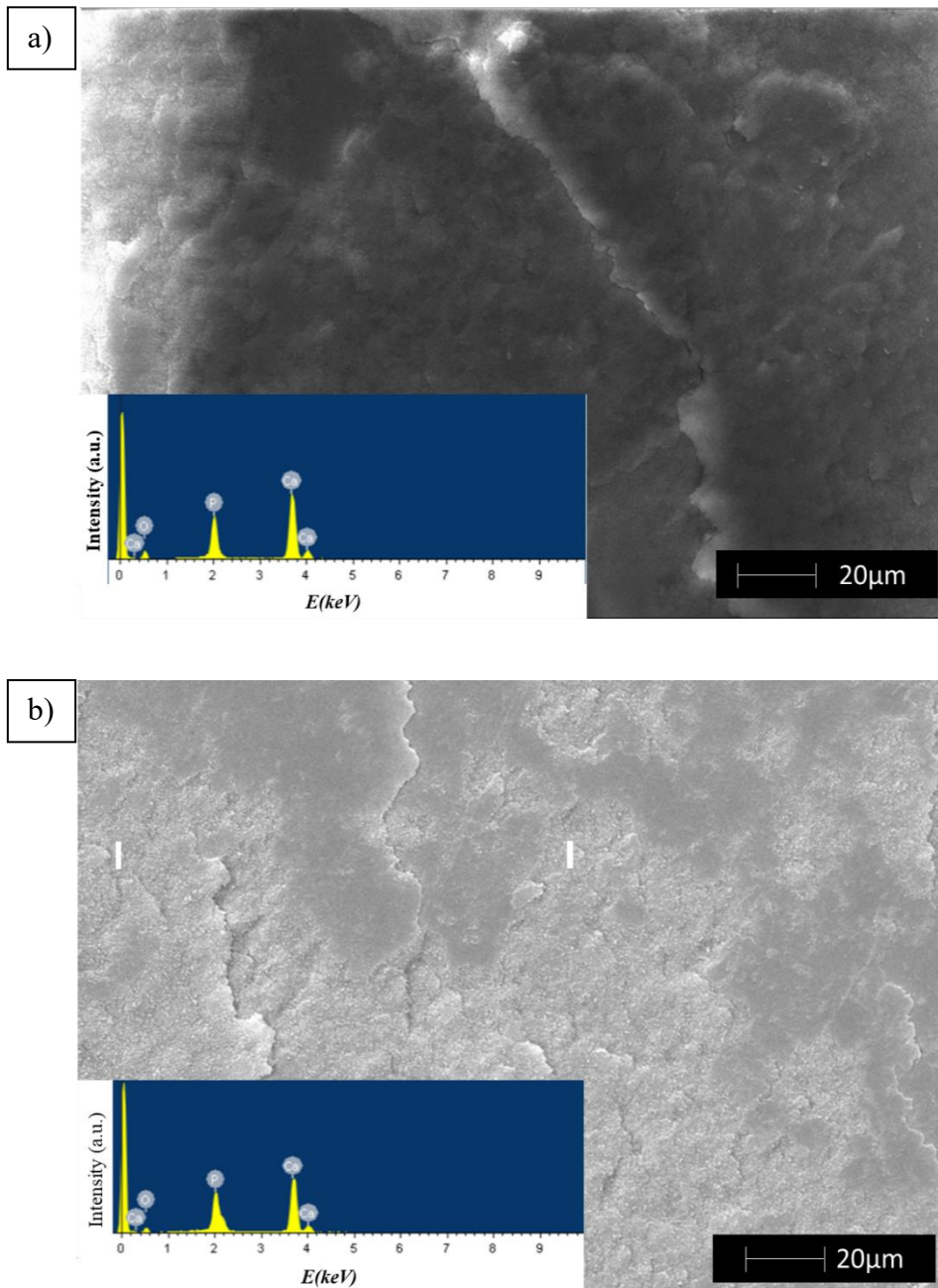


Figure 43: SEM images and EDS spectra obtained from two different samples of HA prec.

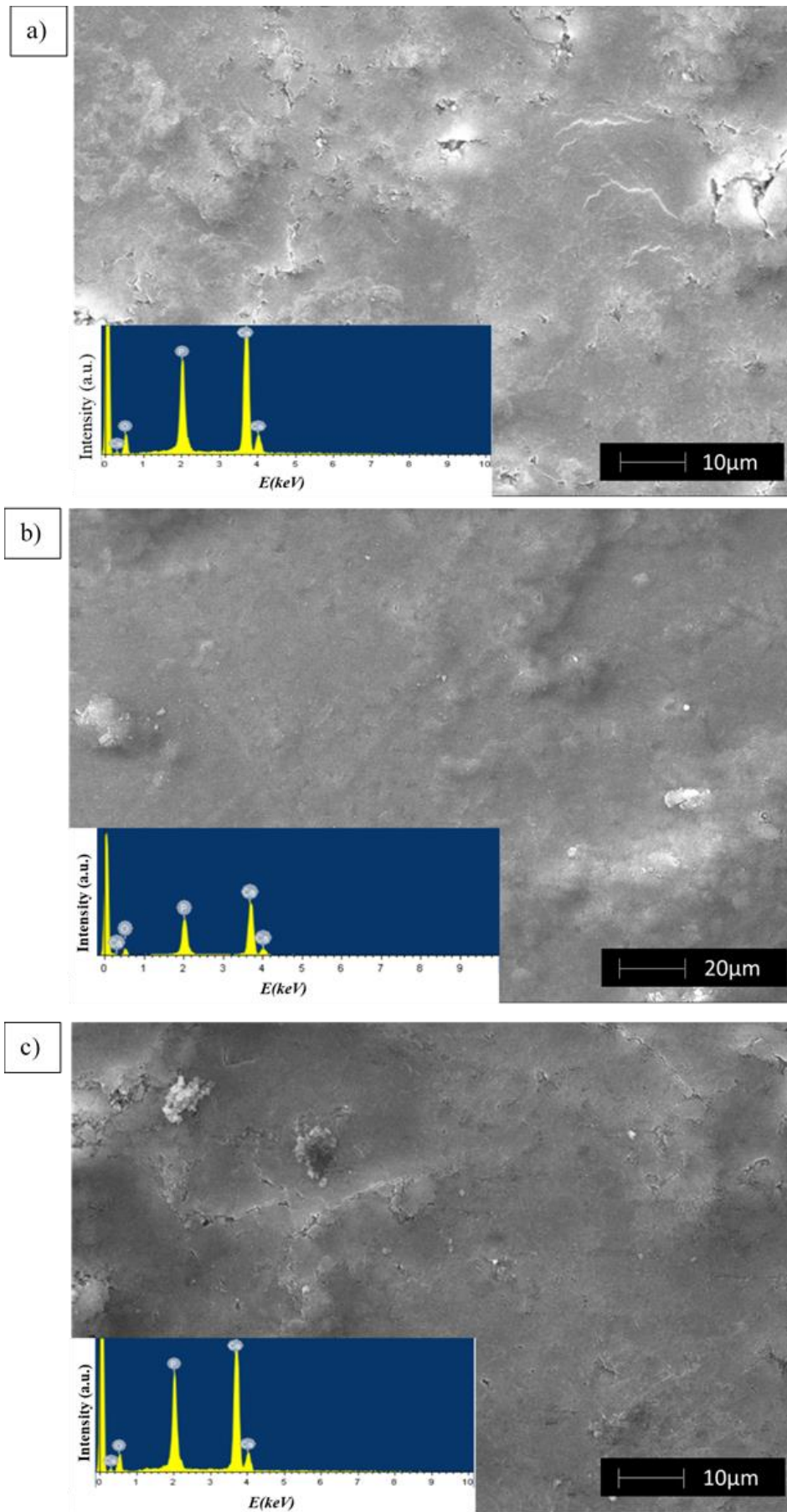


Figure 44: SEM and EDS spectra of HA r.m. obtained from 3 different syntheses.

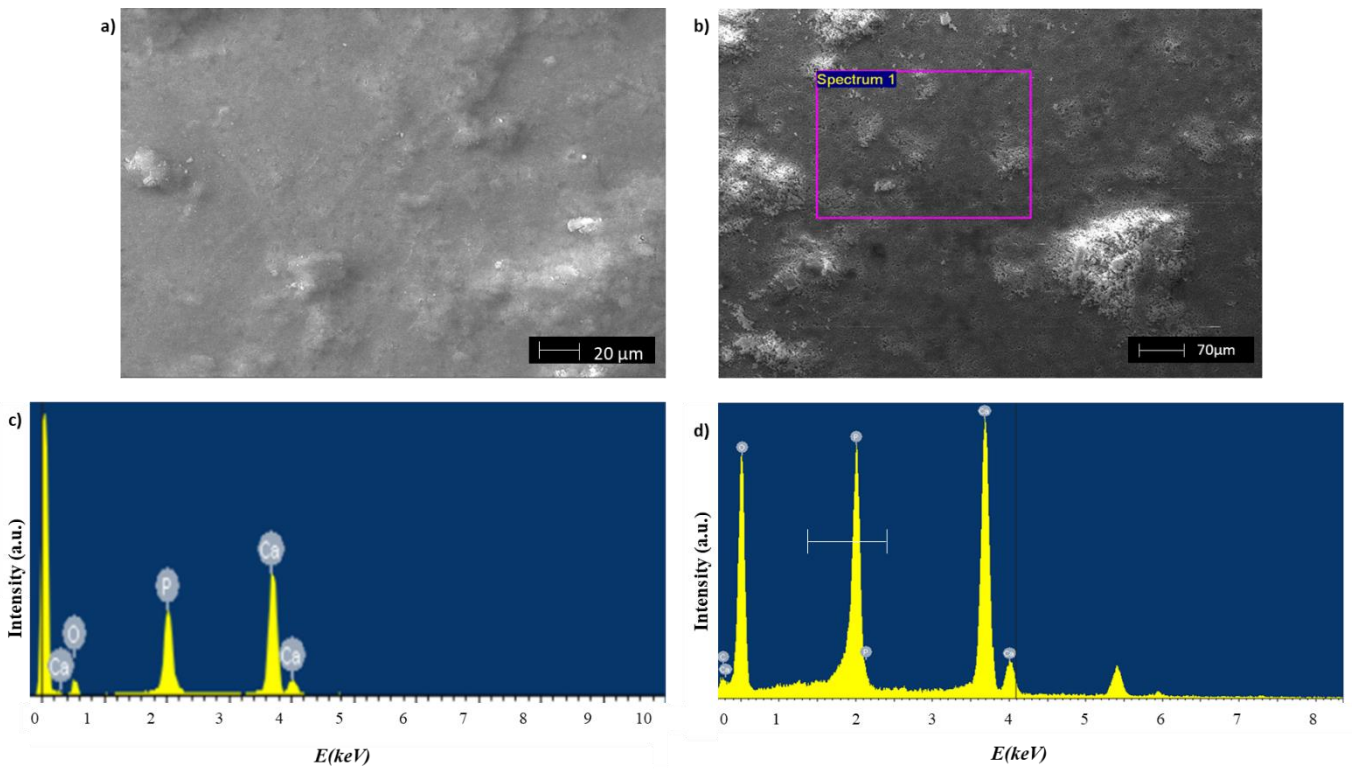


Figure 45: SEM image of a) HA r.m. before sintering and b) HA r.m. after sintering; c) EDS spectra of HA r.m. before sintering and d) EDS spectra of HA r.m. after sintering.

Table 6: Element composition and Ca:P ratios of HA r.m. Before Sintering (BS), Ha r.m. After Sintering (AS) and HA prec. produced.

Measurement	HA prec.	HA r.m. (BS)	HA r.m. (AS)
O	56,49	59,20	68,22
Ca	28,37	25,64	14,34
P	15,14	15,15	8,61
Ca:P ratio	1,87	1,69	1,66

#### 4.3.4 Field Emission Scanning Electron Microscope (FESEM) analysis

FESEM analyses were carried out to investigate HA morphology. It is known from literature that hydroxyapatite aspect ratio (length/diameter of the particle) depends on temperature variations. Specifically, for HA precipitated after the reaction between  $\text{Ca}(\text{OH})_2$  and  $\text{H}_3\text{PO}_4$ , needle like shape is observed at lower reaction temperatures, while spherical shape is usually obtained at higher reaction temperature [70]. In a way to obtain higher aspect ratio, nucleation rate of crystals must be faster than their growth rate, which is prevalent at lower temperatures. Furthermore, morphology depends on precipitation rate, in fact precipitation rate decreases with decreasing aspect ratio. Precipitation rate depends on the driving force of precipitation (Gibbs free energy,  $\Delta G$ ), that is the difference between

the supersaturated and the equilibrium solution of HA. Gibbs free energy is linked to ionic activity product (IAP), solubility product ( $k_{sp}$ ) and temperature (T), according to the following formula:  $\Delta G_{HA} = -(RT/v)\ln(IAP/k_{sp})$ . It is demonstrated that, for HA obtained from the abovementioned reagents, higher driving force is obtained with increasing temperature, because of a subsequent increasing of IAP and decreasing of  $k_{sp}$  [70]. In this work, HA r.m. aspect ratio was analyzed by means of Image-J software, obtaining particles with average dimensions of 43x34 nm with average aspect ratio of 1,29 (Fig. 46 (a)). Observing FESEM images of HA prec. (Fig. 46 (b)) a spherical shape is noticeable due to the high reaction temperature of 100°C. Particles size is uniform with an average size of 24x20 nm with average aspect ratio of 1,23. As expected, comparing the two HA (i.e., r.m. and prec.) synthesized it could be noticed that the one obtained from the precipitation at room temperature and then sintered, achieved a more stretched shape compared to the one precipitated at higher temperature.

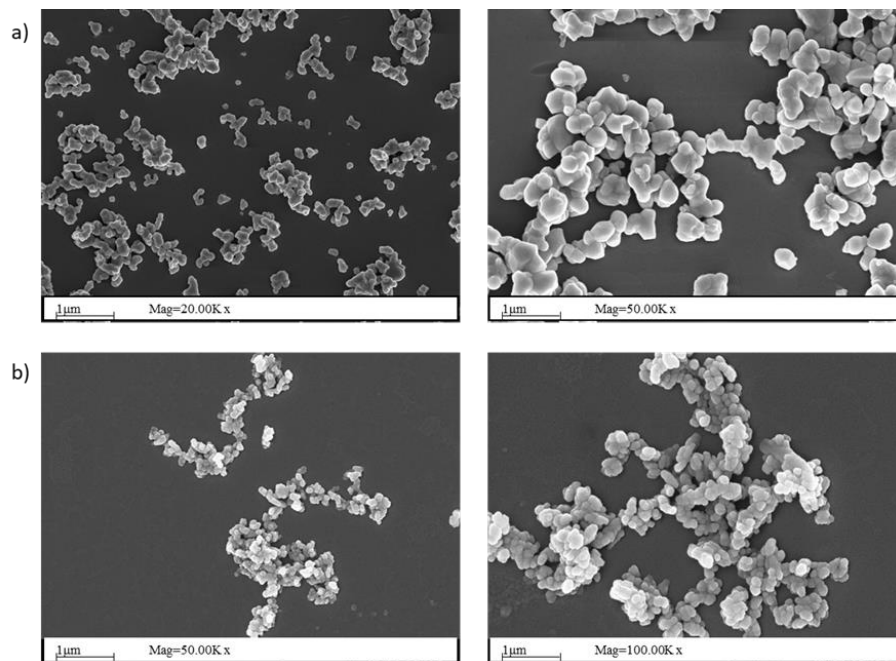


Figure 46: FESEM images of a) HA r.m. at 20K and 50K , b) HA prec. at 50 K and 100K.

#### 4.4 Dispersion of HA powder in gelMA

The process of HA nanoparticles (i.e., r.m. and prec.) dispersion into gelMA (i.e., GelMA 67%) solutions was optimized to obtain a homogeneous mixture in a simple and no-time consuming way. Composite hydrogel morphology was investigated by SEM analyses. Samples obtained through all the protocols described in paragraph 3.9 was characterized with the exception of the one obtained with the method 7) because sputtering phenomena hindered the analysis of its morphological structure. Based on SEM images observation (Fig. 47), two different methods, one for each kind of hydroxyapatite, were finally selected to get a good HA dispersion within GelMA: method 1) was

selected for HA r.m., while method 5) was selected for HA prec.. Both of these processes are simple to realize and guaranteed a uniform dispersion of HA nanoparticles into gelMA hydrogels.

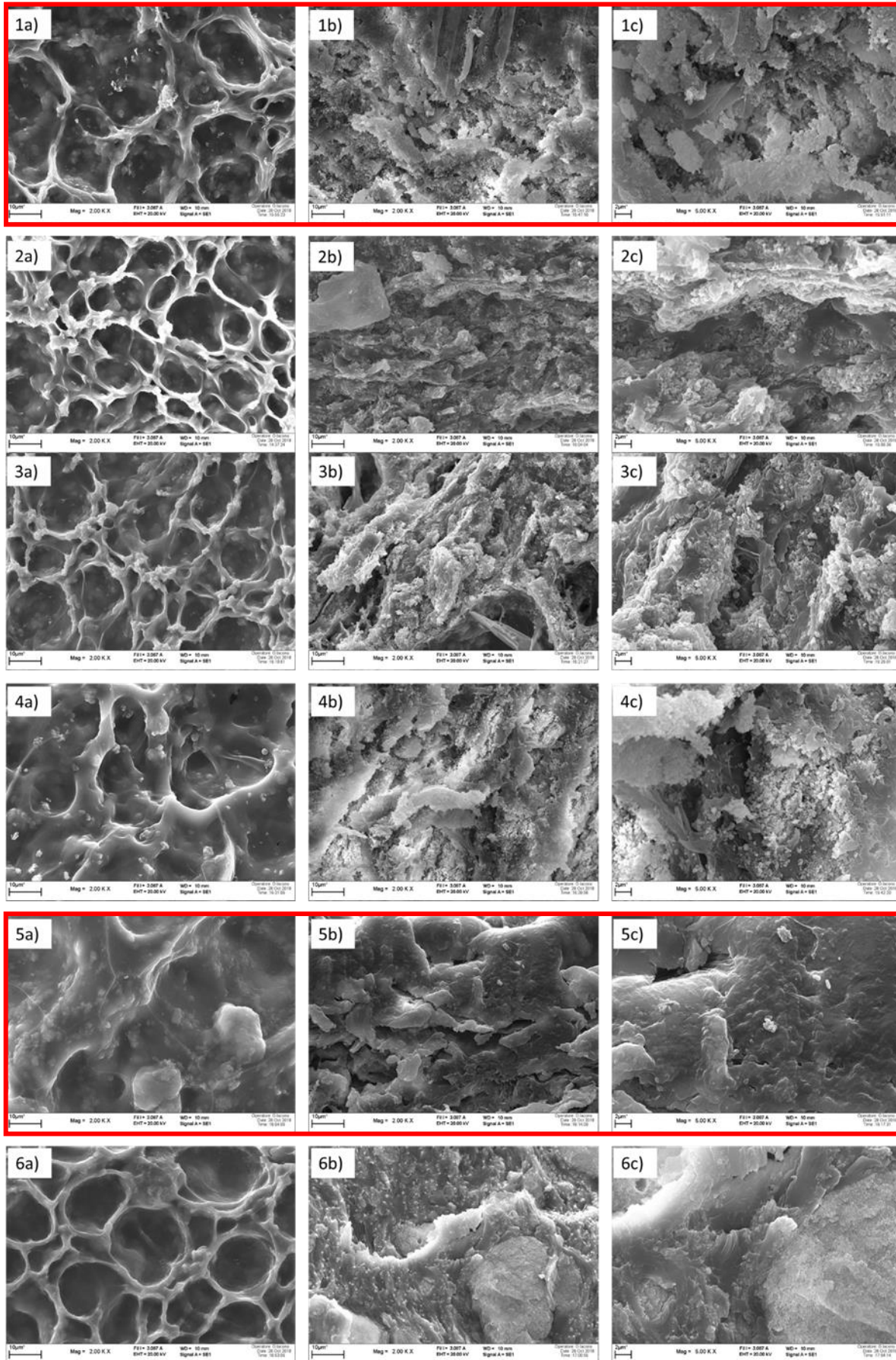


Figure 47: SEM images of a) surface at 2kX, b) cross section at 2kX and c) 5kX of the samples obtained with the methods reported above.

#### 4.4.1 Dispersion stability

Concerning solutions stored at 37 °C (Fig. 48, 49, 50, 51), a different behavior was observed depending on gelMA concentration and HA type. After 10 minutes, the dispersion was apparently stable for each sample. However, after two hours there was a more evident precipitation of HA in each tested solution. At a glance, it seemed that solutions with gelMA at 10% w/v concentration underwent a faster precipitation of HA due to overall lower viscosity of the samples (Fig. 50 (a), 51 (a), 52 (a), 53 (a)). After 24 hours incubation at 37 °C, all samples showed the complete precipitation of dispersed HA. Differently, no precipitation was observed by storing the samples at room temperature, i.e, in the gel state. In conclusion, it was evident that GelMA/HA dispersion storage in the gel state is the best way to preserve HA from precipitation in the long term.

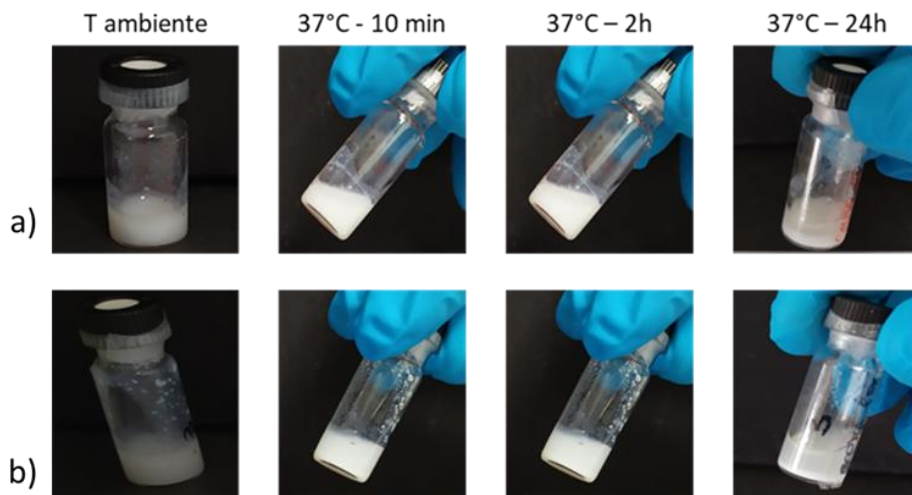


Figure 48: Stability of a) gelMA 67% at 10% w/v and HA prec. 10% w/v, b) gelMA 67% at 15% w/v and HA prec. 10% w/v

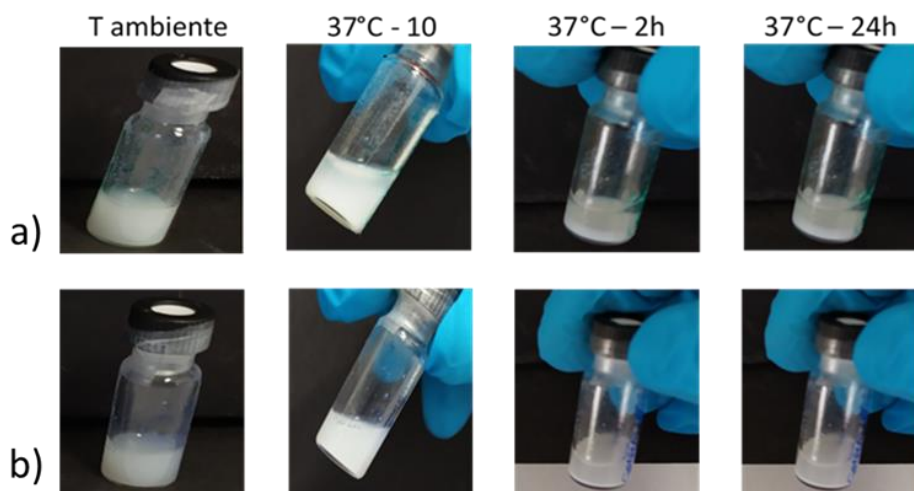


Figure 49: Stability of a) gelMA 67% at 10% w/v and HA prec. 5% w/v, b) gelMA 67% at 15% w/v and HA prec. 5% w/v.

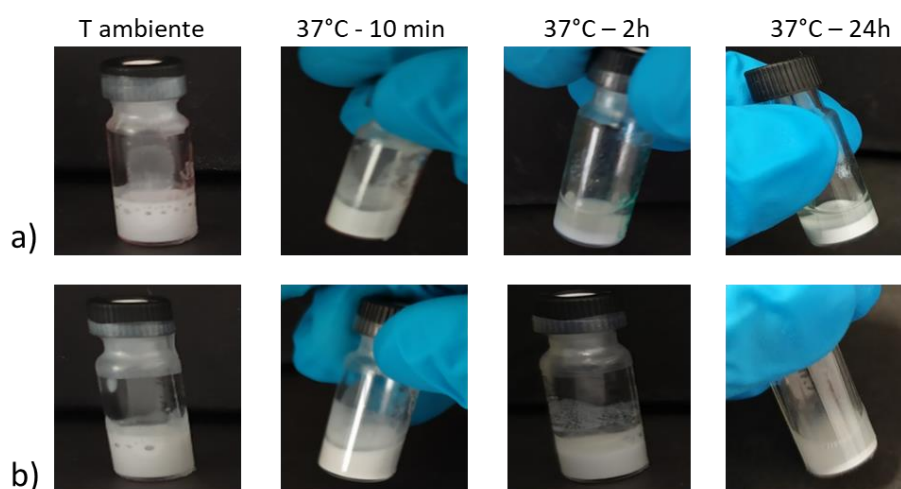


Figure 50: Stability of a) gelMA 67% at 10% w/v and HA r.m. 10% w/v, b) gelMA 67% at 15% w/v and HA r.m. 10% w/v.

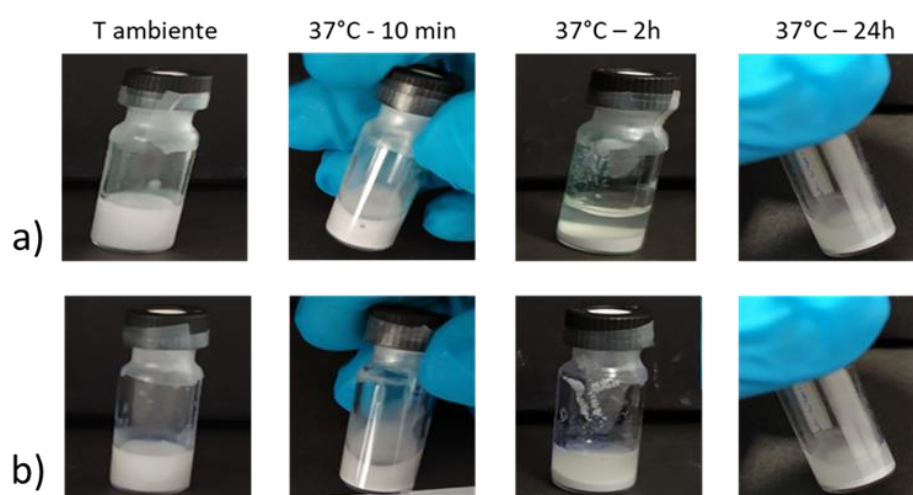


Figure 51: Stability of a) gelMA 67% at 10% w/v and HA r.m. 5% w/v, b) gelMA 67% at 15% w/v and HA r.m. 5% w/v.

Concerning gelMA 74%, it was assumed that the behavior of HA dispersed in GelMA solutions at 10% w/v concentration would have been the same. Hence, the stability of formulations containing GelMA 74% at 15%w/v was assessed upon addition of HA at 5 or 10 %w/v (Fig. 52, Fig. 53). Also for this type of gelMA fast gelation of the samples at room temperature occurred, leading to the absence of HA precipitation phenomena. Conversely, at 37 °C, a good HA dispersion was observe up to 10 minute storage. Then, progressive HA precipitation occurred at 37 °C. A similar trend was observed for gelatin-based composite formulations (Fig. 54, Fig. 55), suggesting that the exposure of methacrylamide and methacrylate moieties along gelatin backbone did not influence the stability of the dispersions.

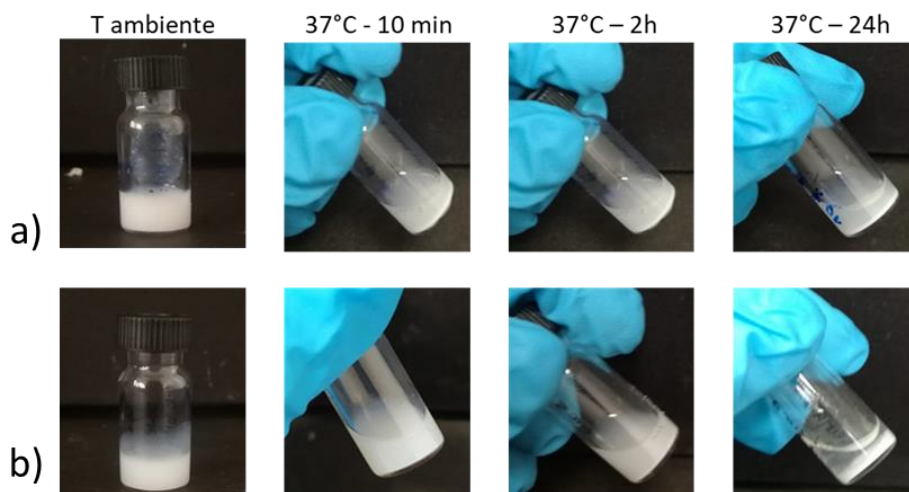


Figure 52: Stability of gelMA 74% at 15% w/v with a) HA prec. 10 % w/v and b) HA prec. 5% w/v.

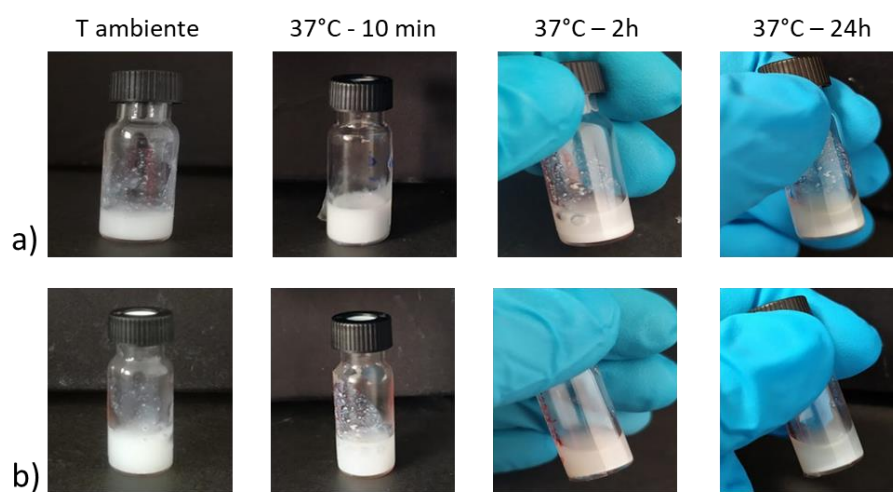


Figure 53: Stability of gelMA 74% at 15% w/v with a) HA r.m. 10 % w/v and b) HA r.m. 5% w/v.

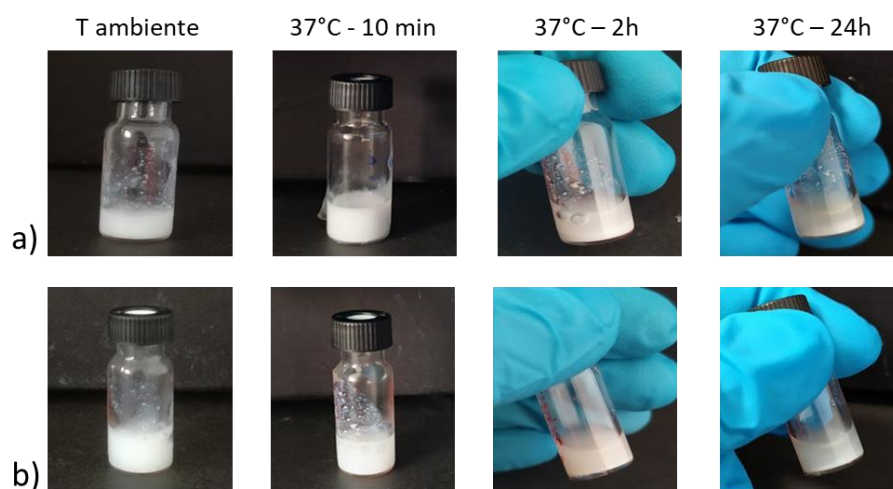


Figure 54: Stability of gelatin at 15% w/v with a) HA prec. 10 % w/v and b) HA prec. 5% w/v.

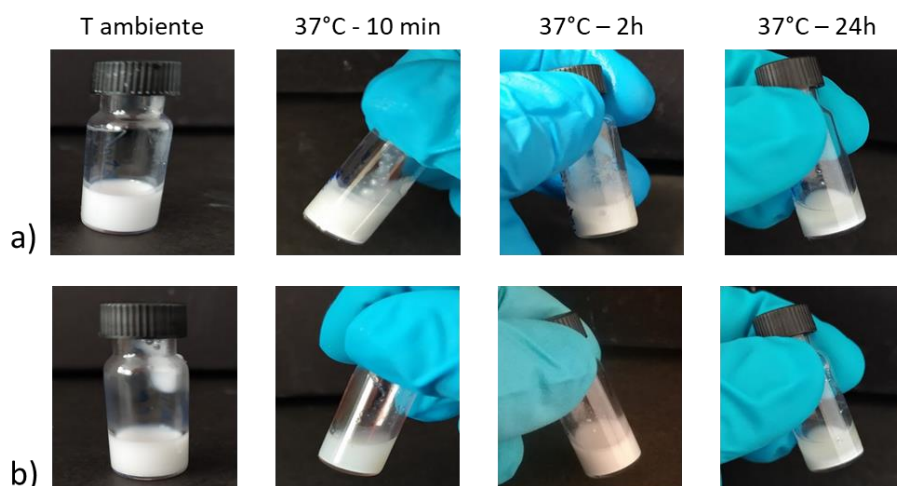


Figure 55: Stability of gelatin at 15% w/v with a) HA r.m. 10% w/v and b) HA r.m. 5% w/v.

#### 4.4.2 Tube inverting test on gelMA/HA composite solutions

As highlighted in Tab. 7, the addition of HA caused an increase in the sol/gel transition temperature of gelMA samples. In gelMA 74%, the addition of HA prec. caused a higher reduction in the sol/gel transition temperature than that of samples containing HA r.m.. Concerning gelatin, HA addition seemed to not influence sample sol/gel transition temperature. Observed differences could be correlated to the interactions (e.g., hydrogen bonds) occurring between HA nanoparticles and gelMA chains which make the gels stable within a wider temperature window, i.e., a higher temperature turned out to be required to induce the gel-to-sol transition. Further rheological characterization will be performed to better evaluate the influence of particles on the sol-gel transition of GelMA and gelatin samples.

Table 7: Gelation temperature of gelatin, gelMA 67% and gelMA 74%.

Gelatin 15% w/v	T of gelation (°C)	gelMA 67%, 15% w/v	T of gelation (°C)	gelMA 74%, 15% w/v	T of gelation (°C)
without HA	28	without HA	25	without HA	25
with HA r.m. 10 w/v	29	with HA r.m. 10 w/v	28	with HA r.m. 10 w/v	28
with HA r.m. 5% w/v	28	with HA r.m. 5% w/v	28	with HA r.m. 5% w/v	28
with HA prec. 10% w/v	28	with HA prec. 10% w/v	27	with HA prec. 10% w/v	26
with HA prec. 5% w/v	28	with HA prec. 5% w/v	27	with HA prec. 5% w/v	26

#### 4.5 GelMA/HA based hydrogel

Photo-cured gels were successfully obtained at 0.05%w/v LAP concentration, suggesting that the addition of HA did not hinder the photopolymerization process. From the visual inspection of the prepared gels, HA r.m. turned out to be better dispersed into gelMA gels (Fig. 56), but SEM analyses were necessary to confirm this hypothesis (Fig. 57, Fig. 58).

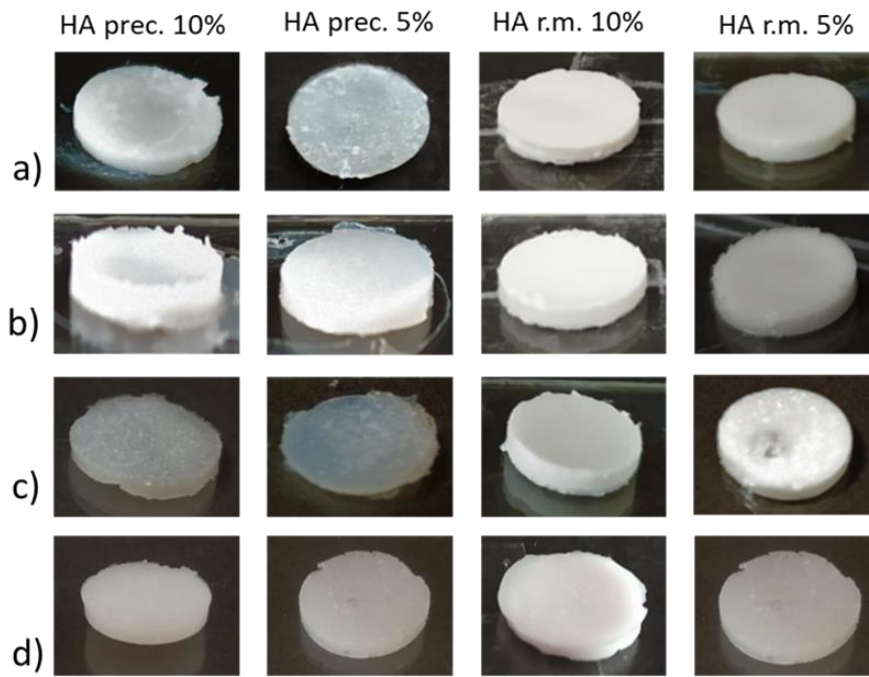
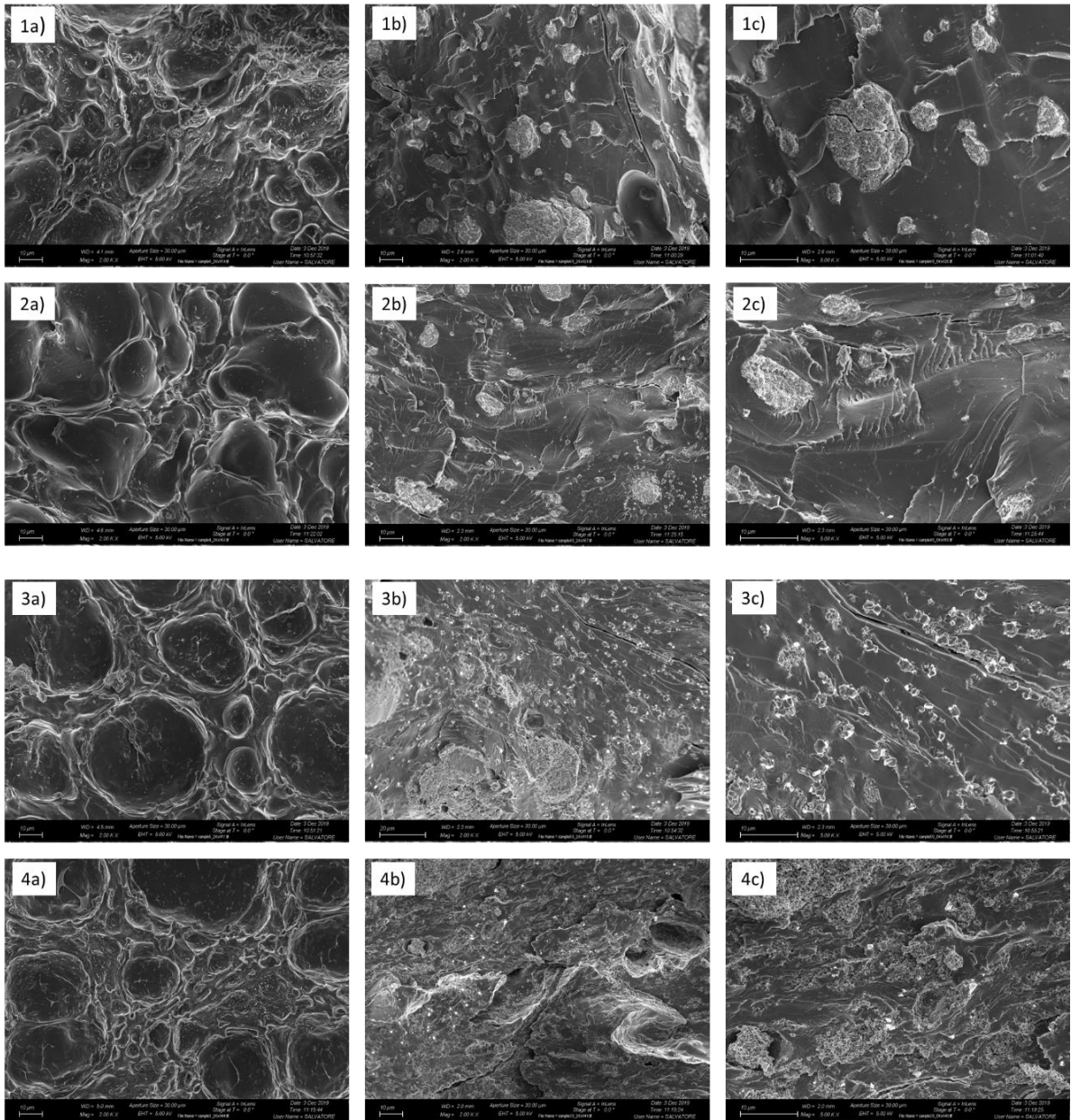


Figure 56: Samples of a) gelMA 67% at 10% w/v, b) gelMA 67% at 15% w/v, c) gelMA 74% at 15% w/v and d) gelatin at 15% w/v with hydroxyapatite.



**Figure 57: SEM images of 1a) surface at 2kX, 1b) cross section at 2kX and 1c) cross section at 5kX of gelMA 74% and HA prec. 10% w/v; 2a) surface at 2kX, 2b) cross section at 2kX and 2c) cross section at 5kX of gelMA 74% and HA prec. 5% w/v; 3a) surface at 2kX, 3b) cross section at 2kX and 3c) cross section at 5kX of gelMA 74% and HA r.m. 10% w/v; 4a) surface at 2kX, 4b) cross section at 2kX and 4c) cross section at 5kX of gelMA 74% and HA r.m. 5% w/v.**

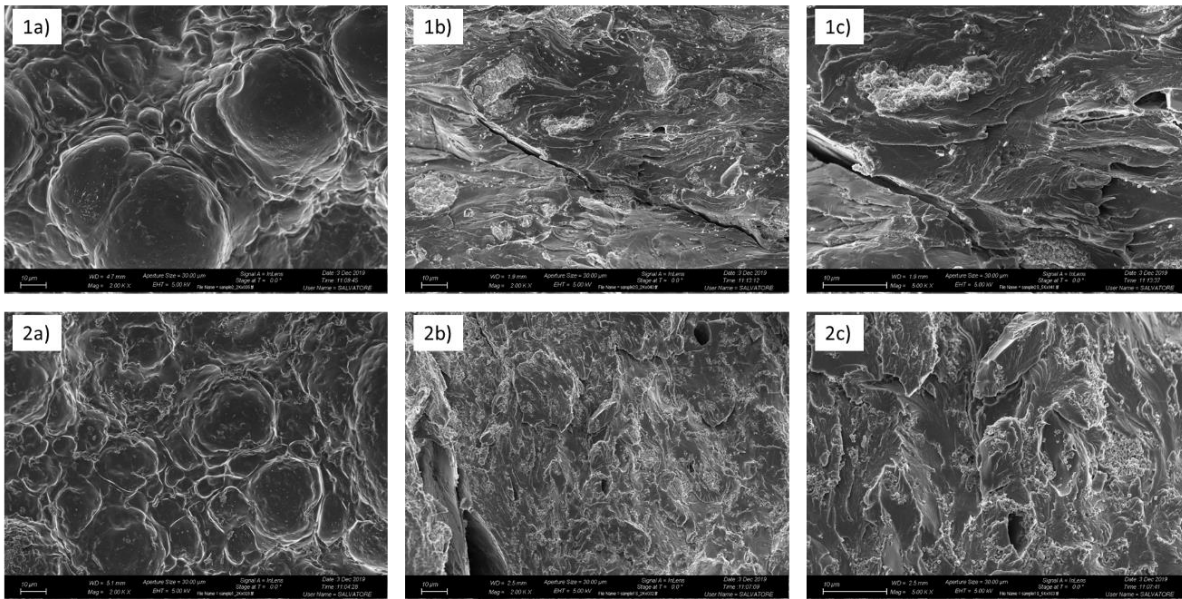


Figure 58: SEM images of: 1a) surface at 2kX, 1b) cross section at 2kX and 1c) cross section at 5kX of **gelMA 67% and HA prec. 5% w/v**; 2a) surface at 2kX, 2b) cross section at 2kX and 2c) cross section at 5kX of **gelMA 67% and HA r.m. 5% w/v**;

#### 4.5.1 Photo-rheological characterization

Regarding hydrogels with HA, it was evident that the presence of nanopowder did not inhibit the crosslinking of the gels also at the lowest tested LAP concentration (i.e., 0.05% w/v) (Fig. 59, Fig. 60). It was evident from a visual analysis that the HA r.m. (at 10% and 5% w/v) was better dispersed into gelMA solutions (at 15% w/v) compared to HA prec. (at 10% and 5% w/v). The latter formed noticeable aggregates (Fig. 61 (a), Fig. 62 (a)). These data further confirmed evidences provided by circular sample visual inspection (Fig. 61(a), Fig. 62 (a)), SEM (Fig. 57((1a-1c),(2a-2c)), Fig. 58 (1a-1c)) and  $\mu$ CT images (Fig. 65 (a), 66 (a)). Storage modulus trend as a function of time before, during and after irradiation for some formulations based on gelMA (at 15% w/v) and HA (HA r.m. at 5% and 10% w/v, HA prec. at 5% and 10% w/v) are reported in Fig. 61 and Fig. 62 as representative examples of gelMA/HA behavior.

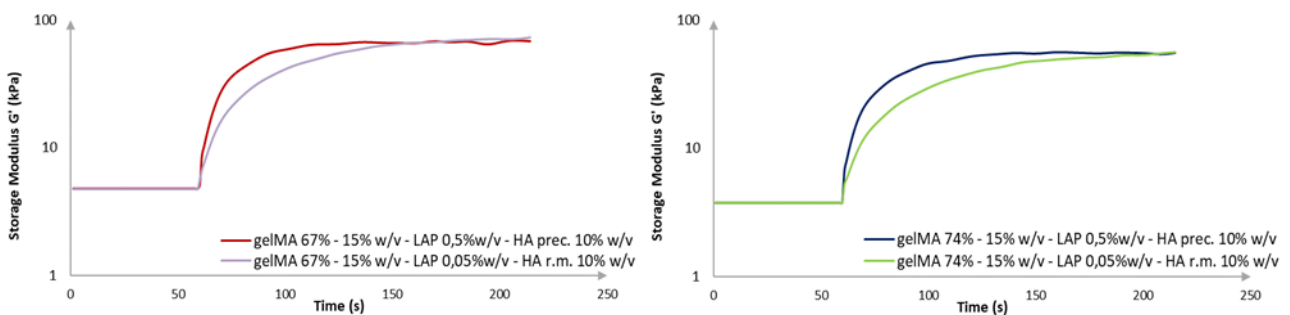


Figure 59: Storage modulus trend of **gelMA 67%** and **gelMA 74%** with HA (i.e., r.m. and prec.) sample before, during and after photo curing as assessed through time sweep tests. GelMA concentration was fixed at 15% w/v, HA concentration was of 10% w/v with LAP concentration at 0.05 and 0.5% w/v

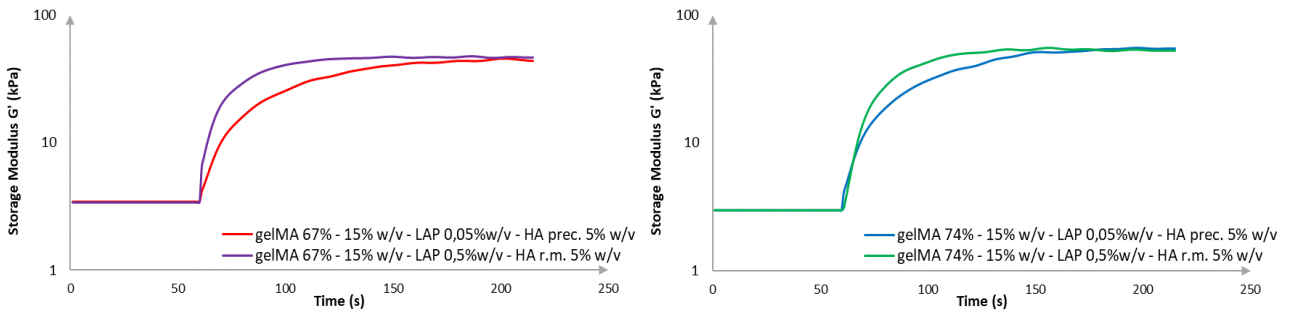


Figure 60: Storage modulus trend of gelMA 67% and gelMA 74% with HA (i.e., r.m. and prec.) sample before, during and after photo curing as assessed through time sweep tests. GelMA concentration was fixed at 15% w/v, HA concentration was of 10% w/v with LAP concentration at 0.05 and 0.5% w/v

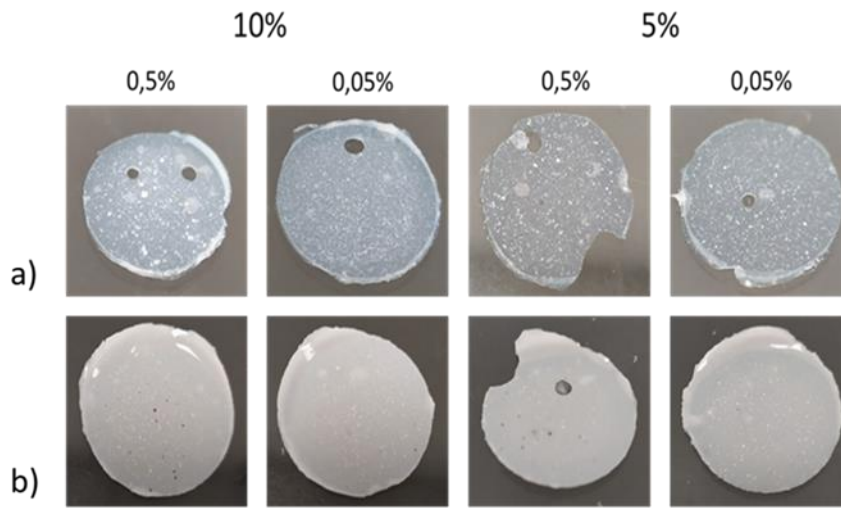


Figure 61: Samples of a) gelMA 67% and HA prec., b) gelMA 67% and HA r.m..

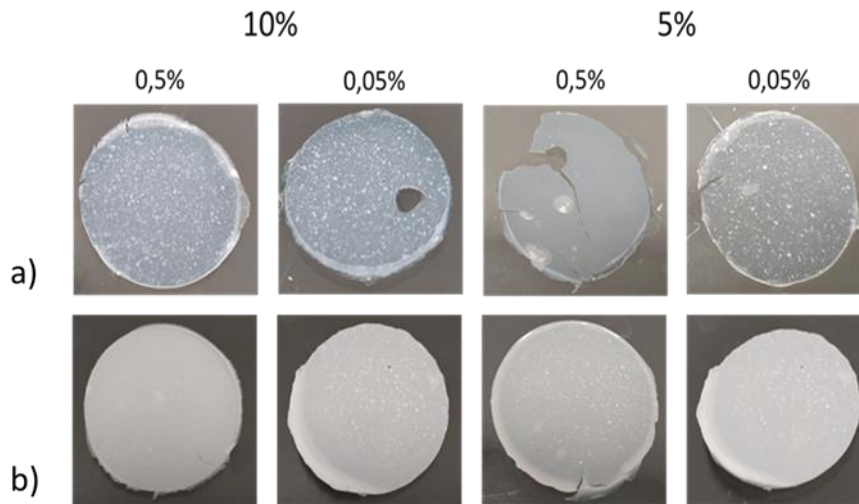


Figure 62: Samples of a) gelMA 74% and HA prec., b) gelMA 74% and HA r.m..

#### 4.5.2 $\mu$ CT analyses

Micro-CT analyses carried out on gelMA (i.e., 67% and 74% at a concentration of 10% and 15% w/v with 0.5% and 0.05% w/v LAP concentration) showed the surface and inner structure of the abovementioned crosslinked hydrogels (Fig. 63, 64). Conventional fabrication method (i.e. casting the material in a mould, followed by freeze-drying process) did not allow to realize materials with a precise geometry. Moreover, the porous nature of the hydrogel based materials contributed to the latter issue. Concerning GelMA/HA crosslinked hydrogels, differences could be noticed between HA prec. and HA r.m. distribution within the hydrogel. Concerning GelMA (i.e., 67% and 74% at a concentration of 15% w/v in PBS)/HA prec. (i.e., at a concentration of 5% and 10% w/v in PBS) with 0.05% LAP, particles aggregates were noticeable (Fig. 65) in each composition. As regard GelMA (i.e., 67% and 74% at a concentration of 15% w/v in PBS)/HA r.m. (i.e., at a concentration of 5% and 10% w/v in PBS) with 0.05% LAP, a uniform dispersion within both gelMA (i.e., 67% and 74%) based hydrogels was achieved with the 5% w/v HA concentration (Fig. 66).

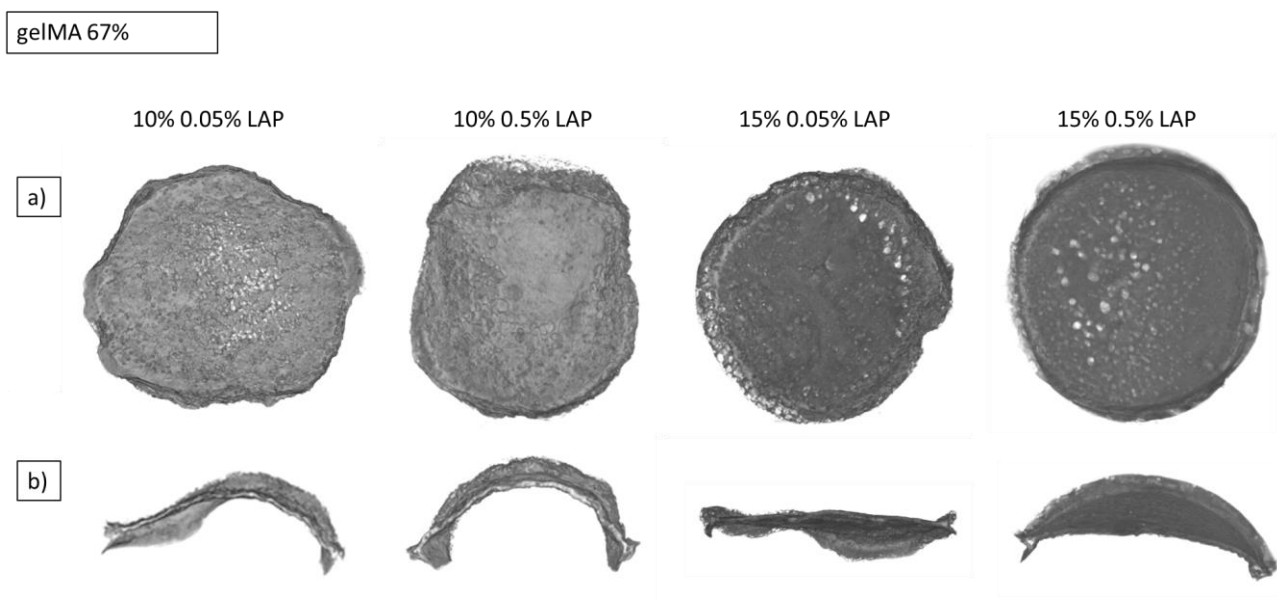


Figure 33: Micro-CT images of a) surface and b) cross section of gelMA 67%.

gelMA 74%

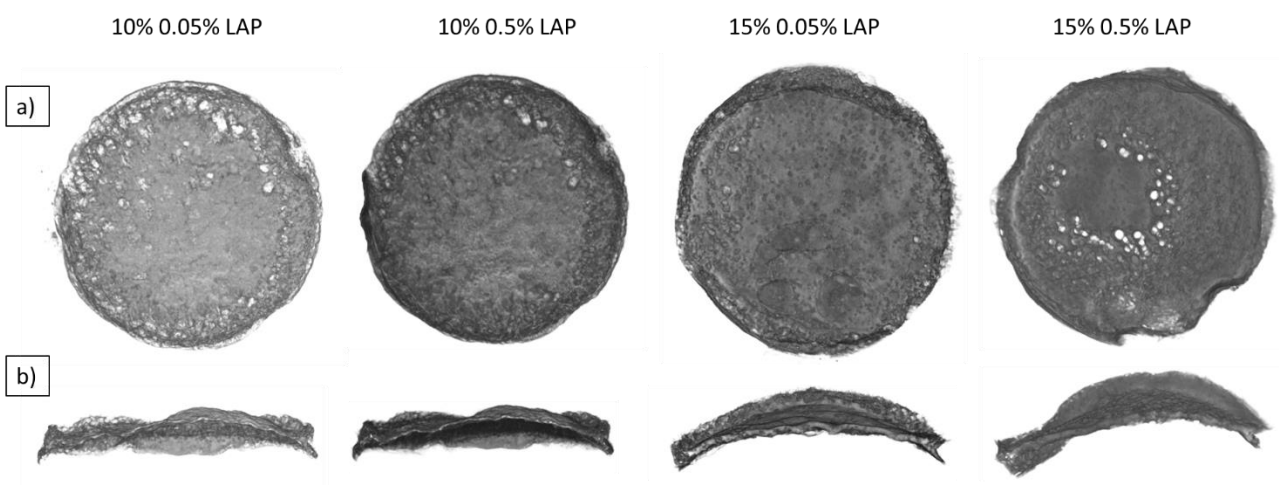


Figure 64: Micro-CT images of a) surface and b) cross section of gelMA 74%.

gelMA 67%

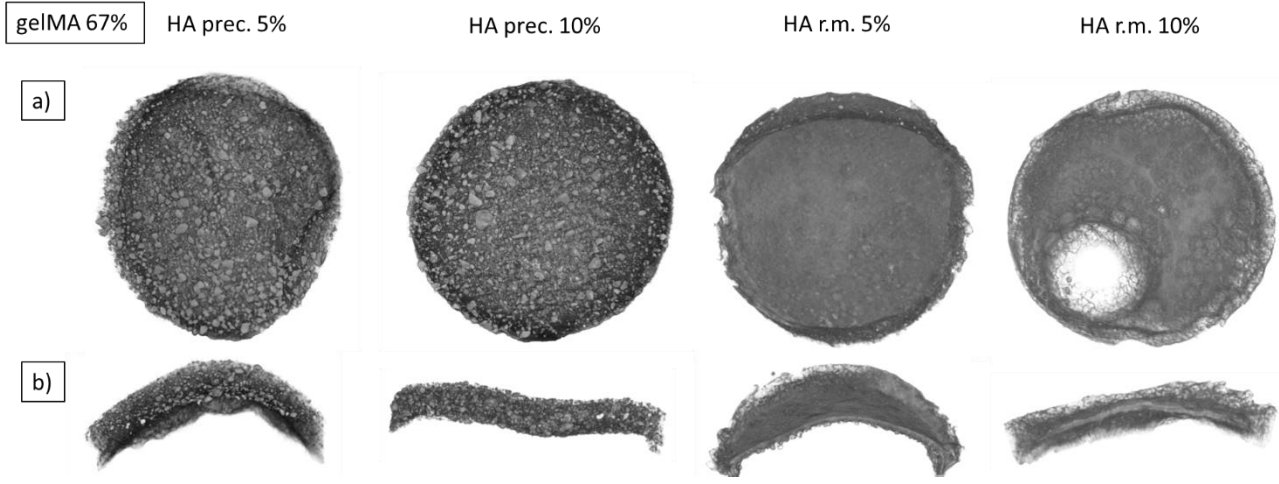


Figure 65: Micro-CT images of a) surface and b) cross section of gelMA/ HA.

gelMA 74%

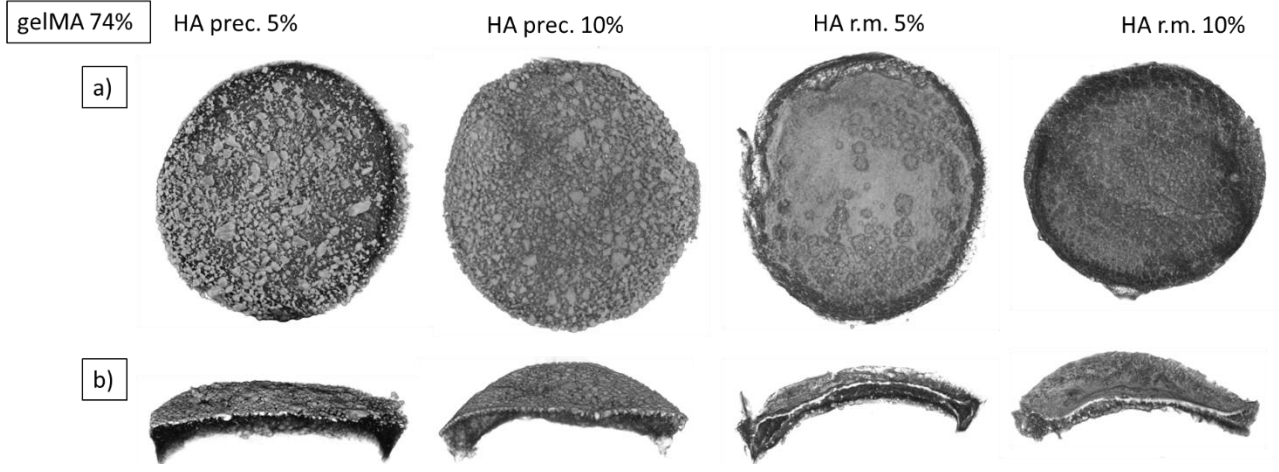


Figure 66: Micro-CT images of a) surface and b) cross section of gelMA/ HA.

## 4.6 PCL/HA based scaffolds characterization

### 4.6.1 Attenuated Total Reflectance Fourier Transform Infrared (ATR-FTIR) Spectroscopy

Concerning PCL/HA powders spectra (Fig. 67), according to the literature, hydroxyapatite peaks can be found at  $3555\text{ cm}^{-1}$  and  $622\text{ cm}^{-1}$  (structural OH),  $1040\text{ cm}^{-1}$  and  $561\text{ cm}^{-1}$  (respectively related to  $\text{PO}_4$  bending  $\nu_3$  and  $\nu_4$ ) [72]. Concerning polycaprolactone, a strong peak at  $1727\text{ cm}^{-1}$  due to the carbonyl stretching can be appreciated. A wider description of PCL and hydroxyapatite related peaks has been provided in tab. 8 [72], [73].

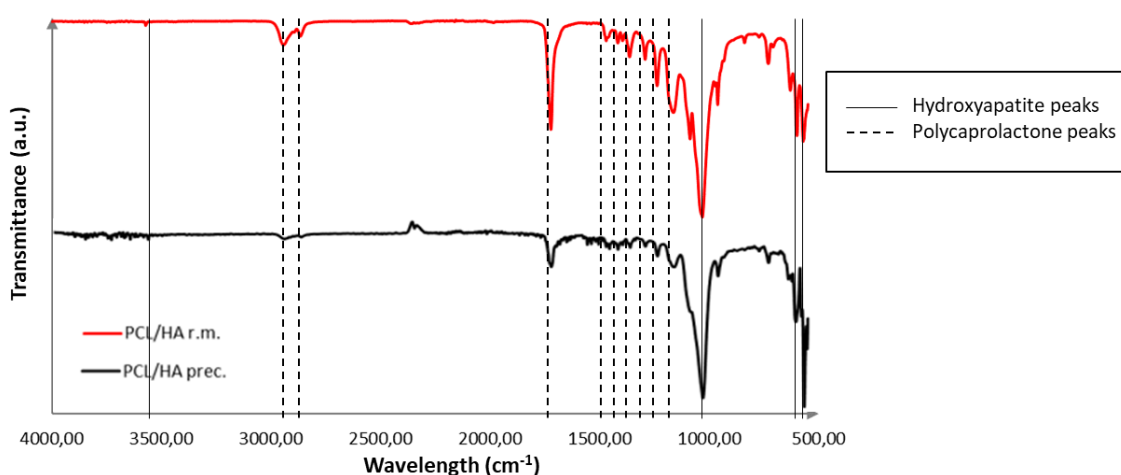


Figure 67: ATR-FTIR spectra of PCL/HA r.m. and PCL/HA prec..

In order to demonstrate HA presence in PCL/HA based scaffolds, ATR-FTIR analyses have been carried out on strands made up of the abovementioned composites (Fig. 68).

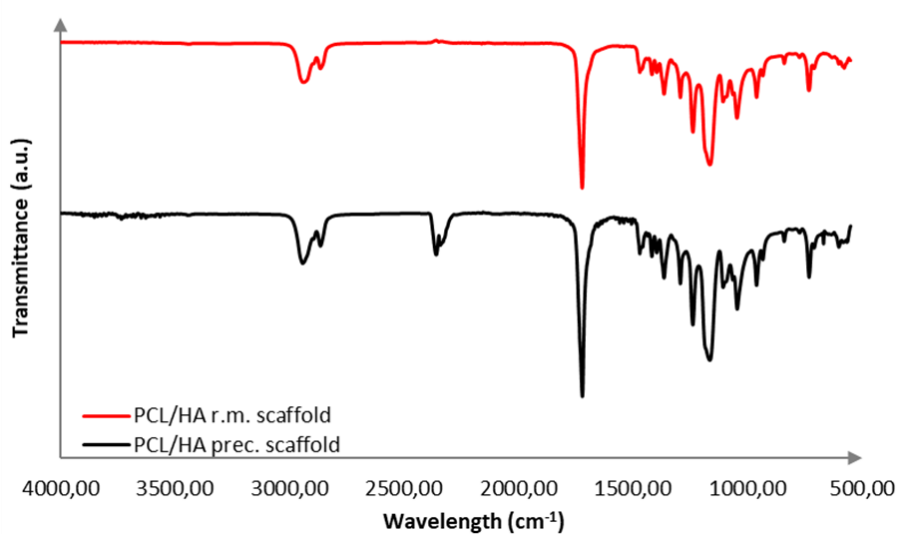


Figure 68: ATR-FTIR spectra on PCL/HA r.m. and PCL/HA prec. based strands.

Table 8: polycaprolactone and hydroxyapatite related peaks.

Wavelength (cm <sup>-1</sup> )	Vibration
3555	Structural OH
2949	Asymmetric CH <sub>2</sub> stretching
2865	Symmetric CH <sub>2</sub> stretching
1727	Carbonyl stretching
1293	C=O and C=C stretching in the crystalline phase
1240	Asymmetric COC stretching
1190	OC=O stretching
1170	Symmetric COC stretching
1157	C=O and C=C stretching in the amorphous phase
1040	PO <sub>4</sub> bending
622	Structural OH
561	PO <sub>4</sub> bending

#### 4.6.2 $\mu$ CT analyses

By means of  $\mu$ CT analyses, PCL/HA (i.e., r.m. and prec.) morphology and porosity was analysed. From fig. 69 it could be observed that, the 3D bioplotter technology allowed to reach precise structure with well defined strands. The final diameter of the latter was of 465  $\mu$ m and 526  $\mu$ m for PCL/HA prec. and r.m. respectively. This difference (from the 320  $\mu$ m desired one) was probably due to the printing parameters (such as needle offset, pressure, XY plane speed and platform temperature) which lead to more or less flattened fibres. Moreover, the heat kept by PCL/HA layers affected the behaviour of the adjacent deposited strands. Though, an open porosity of 59,14% and 62,01% was reached by PCL/HA prec. and PCL/HA r.m. with a negligible standard deviation. Furthermore, a better dispersion within PCL could be observed for HA prec. (Fig. 69a), while particle aggregates could be noticed in PCL/HA r.m. (Fig. 69b). According to several studies concerning particle aggregations, shape and size of the latter are strongly related to this phenomenon. Specifically, Van der Waals and Electrostatic Double Layer forces are reduced with lower particle size (i.e., at the nanometric scale), while changings occur within the superficial charge, reactivity and electronic structure. Moreover, considering the particles' different shape (e.g., spherical, spindle or rod like), it was demonstrated that, at separation distances lower than the average diameter, anisometric particles (e.g., needle like shaped) aggregation occurs with higher probability if compared with spherical ones (Vold, 1954). This is related to the higher amount of atoms close to each other [74].

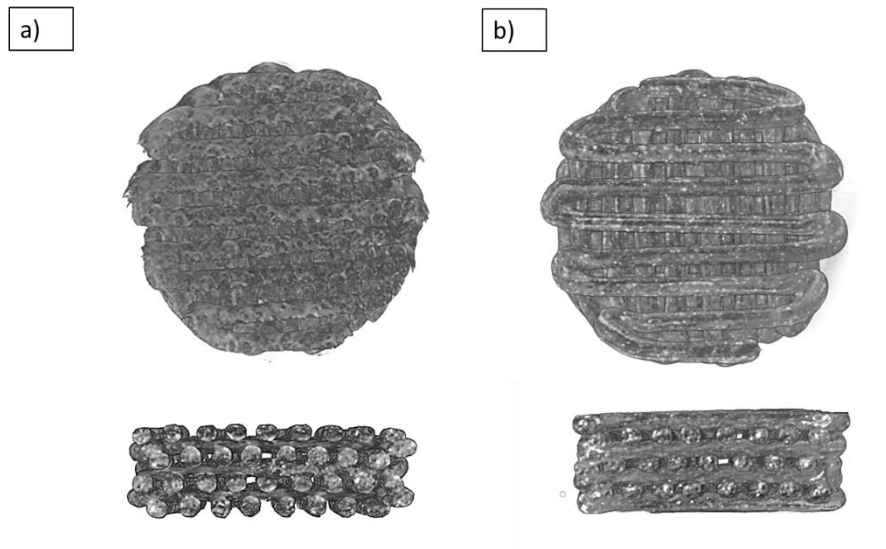


Figure 69:  $\mu$ CT images of a) PCL/HA prec. and b) PCL/HA r.m. surface and section.

#### 4.6.3 SEM analyses

Concerning SEM analyses, the homogeneity of the observed structures (i.e., PCL/HA prec. and PCL/HA r.m.) was assessed (Fig. 70, 71). Moreover, the 3D printing allowed in both cases to achieve a precise geometry and overall constant thickness of the strands. PCL/HA r.m. based scaffolds showed HA aggregates within the structure (Fig. 70 (b) and 71 (b)), on the contrary in PCL/HA prec. based scaffolds a lower amount of particles could be observed both on the surface and section (Fig. 70 (a) and 71 (a)). This result confirmed the one obtained with  $\mu$ CT analyses (Fig. 69 (b)).

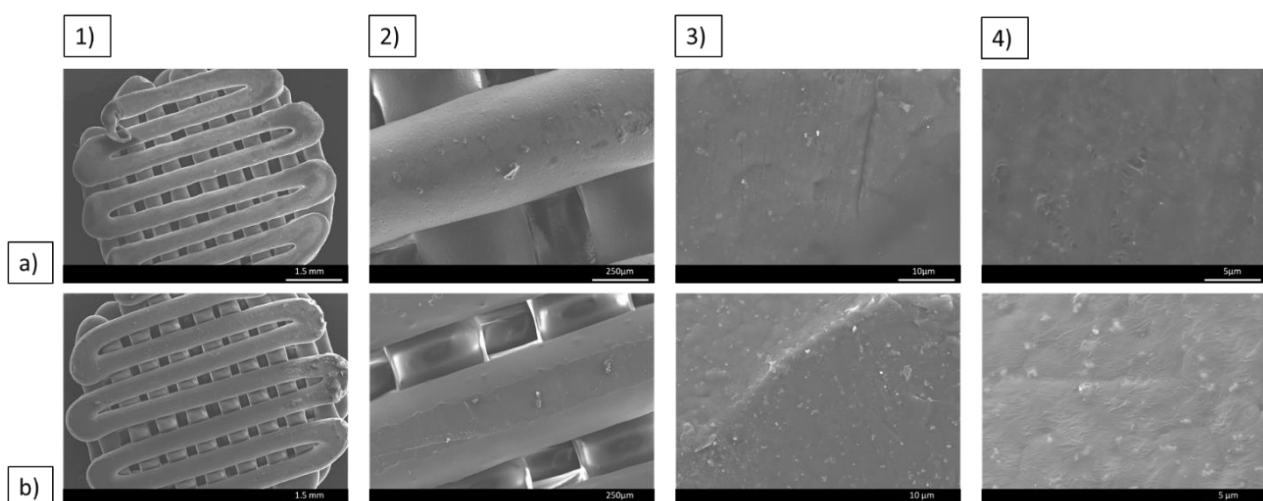


Figure 70: SEM images of a) PCL/HA prec. and b) PCL/HA r.m. surface at 1) 15x, 2) 100x, 3) 2Kx, 4) 5Kx.

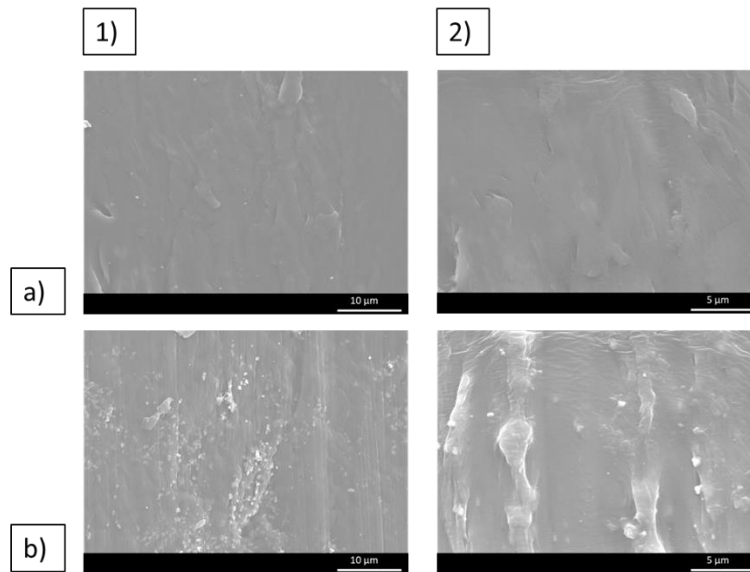


Figure 71: SEM images of a) PCL/HA prec. and b) PCL/HA r.m. cross section at 1) 2Kx and 2) 5Kx.

#### 4.6.4 Compressive test

Concerning the compressive tests carried out on PCL/HA (i.e., prec. and r.m.), differences could be noticed between the two blends (Fig. 72). None of the tested samples was broken at the maximum load (i.e., 490N), reaching the plasticity region. According to previous research works, porous scaffolds (i.e., with 60% porosity) made of PCL alone reached a compressive modulus of approx. 51 MPa, while the addition of HA phase lead to the material hardening [75]. Moreover, several studies showed how hydroxyapatite's mechanical properties (such as the Young modulus) were affected by thermal treatments (i.e., sintering process). Specifically, according to the work described in [76], hydroxyapatite Young's Modulus reached higher values (i.e., ranging from 42 to 81 GPa) with increasing sintering temperatures (i.e., from 1150 to 1300 °C). In this work PCL compressive modulus gathered from literature was used as control for the results obtained. Specifically, the Young modulus (E) varied between PCL/HA prec. and PCL/HA r.m. (i.e., 54% and 69% respectively), as highlighted in tab. 9. Thus, if compared with the porous scaffold made of PCL alone, an overall hardening for the composite structure was achieved, as expected, for both of the considered formulations. Moreover, PCL/HA r.m. showed a higher stiffness (with a steeper linear elastic region) if compared with PCL/HA prec., reaching lower levels of strain (i.e., 8% and 20% respectively for PCL/HA r.m. and PCL/HA prec.). Finally, the resulting Young modulus was probably affected by two main factors: the different mechanical properties of the hydroxyapatite alone due to the synthesis process (i.e., described in paragraphs 3.7.1 and 3.7.2) and the amount of particle aggregates within the PCL phase, (i.e., higher in PCL/HA r.m. as highlighted from  $\mu$ CT and SEM analyses (Fig. 69, Fig. 70, Fig. 71)).

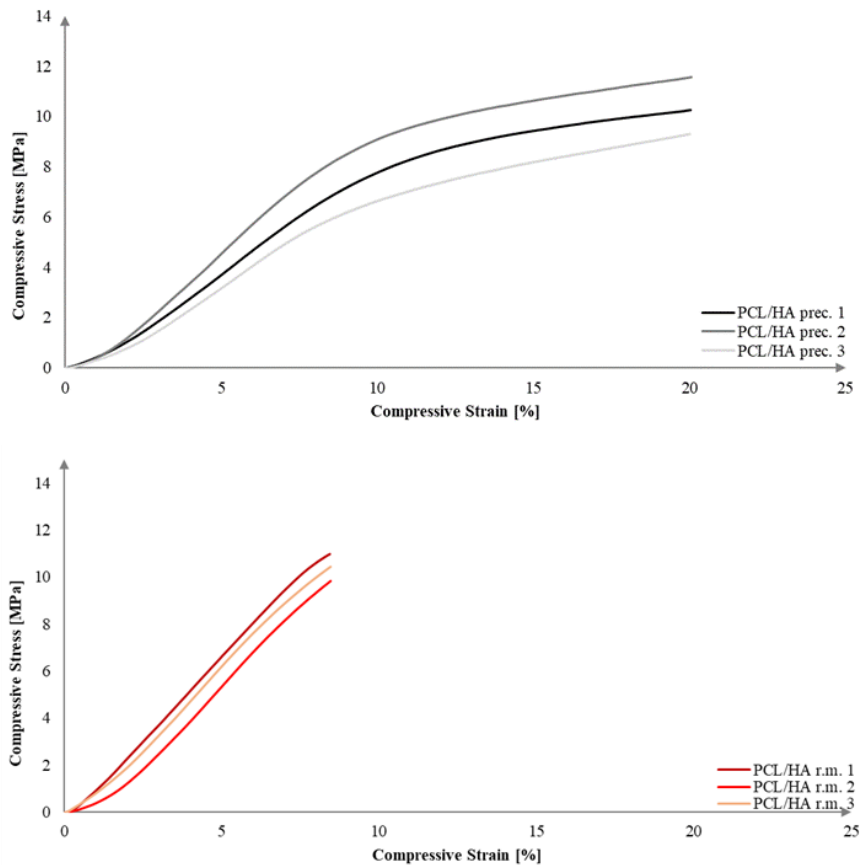


Figure 72: Stress-strain curves of PCL/HA r.m. and PCL/HA prec.

Table 9: Mechanical characteristics of PCL/HA r.m. and PCL/HA prec.

Material	Young Modulus [MPa]	Compressive strain at maximum compressive load [%]
PCL/HA r.m.	69 ±2,01	8 ± 0.0001
PCL/HA prec.	54 ± 0.32	20 ± 0.0001

#### 4.7 Gelatin and gelatin/HA crosslinked hydrogels preparation

Hydrogel solutions (i.e., gelatin at 15% w/v and gel/HA r.m. at 15% and 10% w/v concentration in PBS respectively for gelatin and hydroxyapatite) within 0.25% and 0.3% v/v Glutaraldehyde solution did not completely crosslink with reaction time of 1 and 3 minutes. After 5 minutes, all samples reacted with 0.3% v/v GA became crosslinked hydrogels. However, at this time point, gelatin/hydroxyapatite based hydrogel reacted with 0.25% v/v GA underwent gel-sol transition in incubator at 37°C (Fig. 73 a). Finally, gelatin and gel/HA r.m. crosslinked hydrogels were obtained after ten minutes in 0.25% and 0.3% v/v GA solution (Fig. 73 a, b). Taking into account this last result, the lower tested GA concentration it is preferred for further experiments because of the concernings about the molecule toxicity.

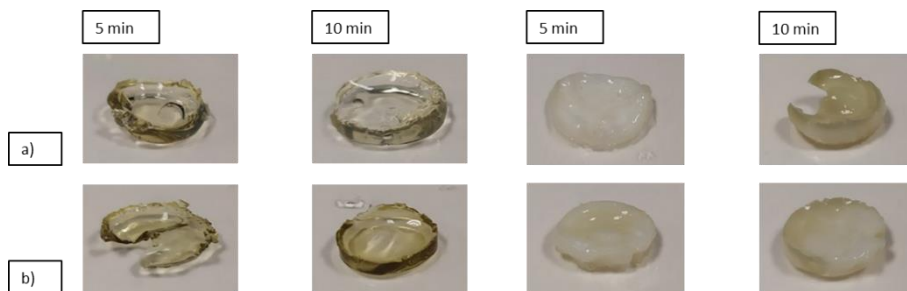


Figure 73: Crosslinked gelatin and gelatin/hydroxyapatite based hydrogel with: a) 0.25% GA and b) 0.3% GA.

## 4.8 Gelatin and gelatin/HA crosslinked hydrogels characterization

### 4.8.1 ATR-FTIR spectroscopy

In order to demonstrate the success of the crosslinking reaction, the dialdehyde peak at  $1960\text{ cm}^{-1}$  was not appreciated in both gelatin and gel/HA r.m. crosslinked hydrogel (i.e., with 0.25% v/v glutaraldehyde solution) spectra (Fig. 74) [77]. Concerning the gelatin spectrum in Fig. 17, amide I related peak (i.e., C=O stretching vibration) could be found at  $\sim 1630\text{ cm}^{-1}$ , while the amide II related peak was at  $\sim 1540\text{ cm}^{-1}$  (i.e., vibration associated to N-H bending and C-N stretching). Moreover, the OH-stretching related peak was appreciated at  $3500\text{ cm}^{-1}$  [66]. According to literature, hydroxyapatite peaks could be found at  $3555\text{ cm}^{-1}$  and  $622\text{ cm}^{-1}$  (structural OH),  $1040\text{ cm}^{-1}$  and  $561\text{ cm}^{-1}$  (respectively related to  $\text{PO}_4$  bending  $\nu_3$  and  $\nu_4$ ) (Fig. 74)[72].

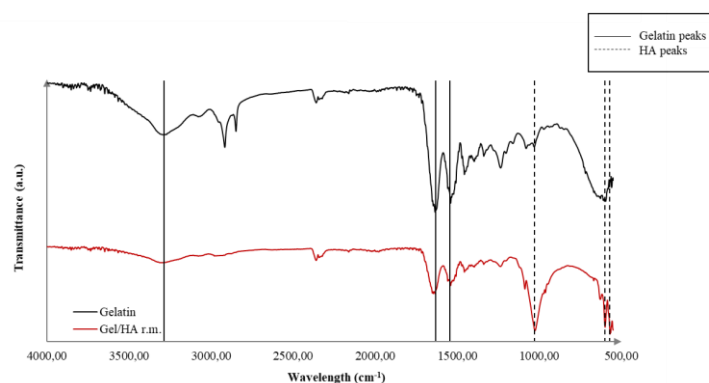


Figure 74: ATR-FTIR spectra of gelatin and gel/HA r.m.

### 4.8.2 $\mu$ CT analyses

Micro-CT analyses on gelatin and gel/HA r.m. samples showed the surface and inner structure of the abovementioned crosslinked hydrogels (Fig. 75). In both cases, conventional fabrication method (i.e. casting the material in a mould, followed by freeze-drying process) did not allow to realize materials with a precise geometry. Moreover, the porous nature of the hydrogel based materials contributed to

the latter issue. According with the result previously obtained with gelMA/HA formulations (Fig.65, Fig.66), Gel/HA r.m. crosslinked hydrogels, showed a uniform HA r.m. distribution (Fig. 75 (2b)).

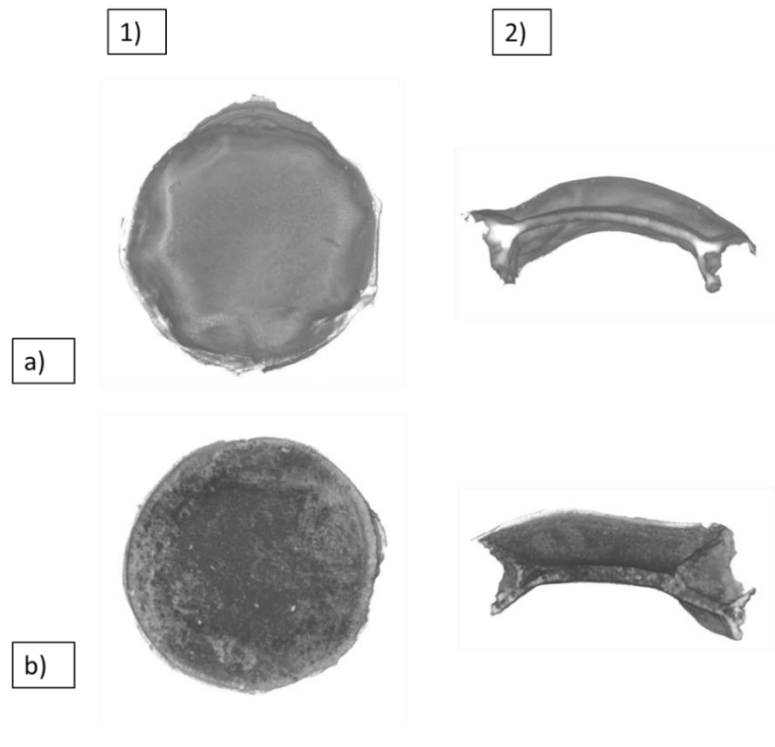


Figure 75: Micro-CT images of 1) surface and 2) cross section of a) gelatin (i.e., 15% w/v) and b) gel/HA r.m. (i.e., 15% and 10% w/v respectively for gelatin and HA r.m.).

#### 4.8.3 Re-swelling test

Fig. 76 reports the trend of swelling ratio overtime for all the analyzed samples. For both types of gelatin and gel/HA gels a plateau of swelling ratio parameter was reached after a maximum of 5h incubation in PBS. Additionally, at this time point, all the samples gave back to their original form and weight (Fig. 77). In particular, the latter reached lower levels of swelling, because of the HA presence within the gelatin network.

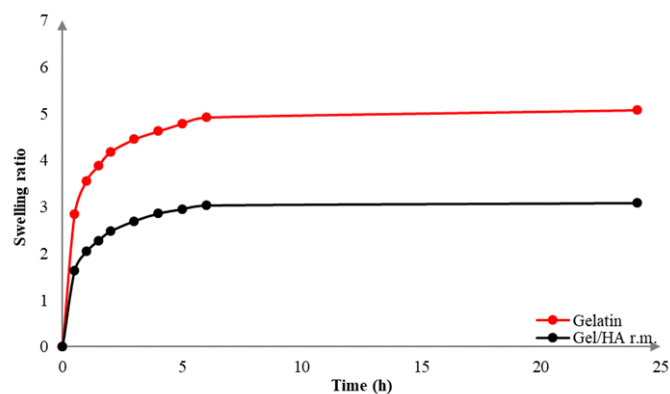


Figure 76: Swelling ratio of Gelatin (i.e., 15% w/v in PBS) and gel/HA r.m. (i.e., 10% and 15% w/v respectively for gelatin and HA r.m. in 0.25% v/v GA solution).

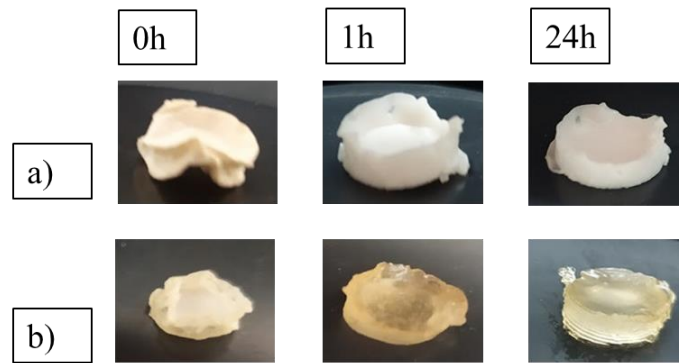


Figure 77: Images of a) gel/HA and b) gelatin swollen hydrogels after 0, 1 and 24h.

#### 4.9 Gel/HA r.m.-PCL/HA multicomponent scaffold fabrication

As highlighted in Fig.78 (a) and (b), a successful coupling between gel/HA r.m. based hydrogels with PCL/HA (i.e., r.m. and prec. at 10%w/w with respect to PCL) based scaffolds was achieved. However, structures with highly definite shape could not be obtained due to the exploited fabrication method and because of the hydrogel behaviour while in sol state.

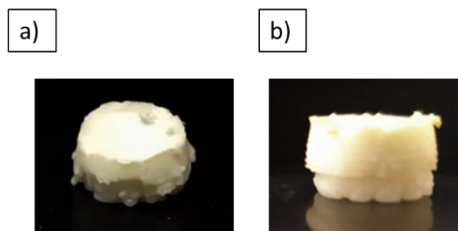


Figure 784: Images of a) PCL/HA r.m. and b) PCL/HA prec. with gel/HA r.m..

#### 4.10 Gel/HA r.m.-PCL/HA multicomponent scaffold characterization

##### 4.10.1 $\mu$ CT analyses

Morphology and porosity of both gel/HA r.m.-PCL/HA (i.e., r.m. and prec.) and gelMA/HA r.m.-PCL/HA (i.e., r.m. and prec.) were analysed. From Fig. 79 and Fig. 80 it could be observed that, the underlying thermoplastic/ceramic based precise structure was kept. The final diameter of the strands was of  $319,5 \pm 0.2 \mu\text{m}$  and  $412,5 \pm 0.2 \mu\text{m}$  for PCL/HA prec.-gel/HA r.m. and PCL/HA r.m.-gel/HA r.m. respectively. In this case, the thickness strand of  $320 \mu\text{m}$  (80% of needle diameter) was not reached, because of the exploited printing parameters (such as needle offset, pressure, XY plane speed and platform temperature) and the heat kept by PCL fibres. Moreover, as highlighted in Fig. 79 (2a) and (2b), gel/HA inclusion were noticeable into PCL/HA open pores, affecting in this way the overall porosity (52,38% and 48,43% for gel/HA r.m.-PCL/HA prec. and gel/HA r.m.-PCL/HA r.m. respectively). Concerning the latter, the obtained standard deviation was negligible.

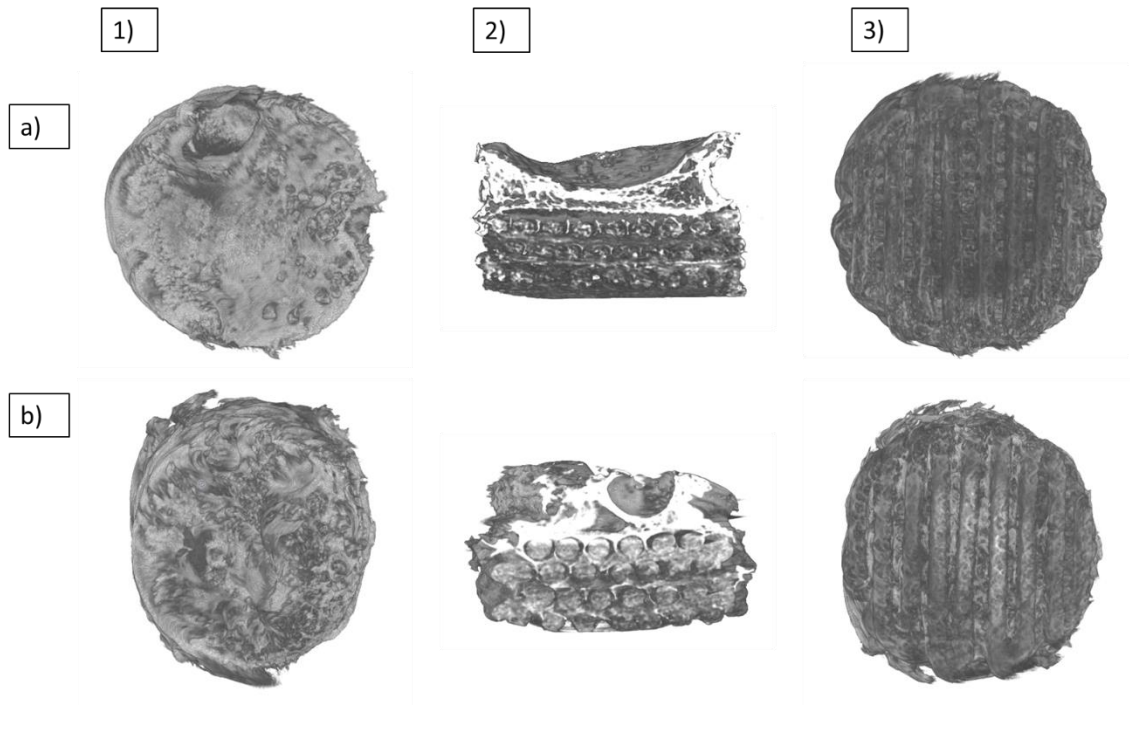


Figure 79: Micro-CT images of 1) top view, 2) cross section and 3) view from below of a) PCL/HA prec.-gel/HA r.m. and b) PCL/HA r.m.-gel/HA r.m..

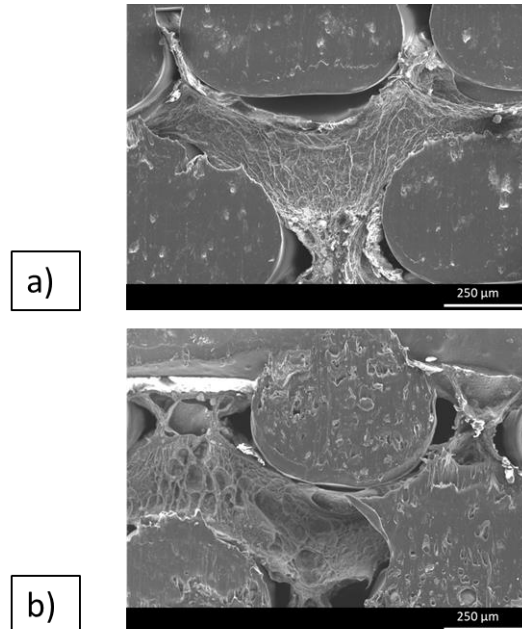


Figure 80: SEM images of a) PCL/HA prec. and b) PCL/HA r.m. coupled with gel/HA r.m. based hydrogels.

#### 4.10.2 Re-Swelling test

Fig. 81 reports the trend of swelling ratio overtime for all the analyzed samples. For both types of gelatin and gel/HA gels a plateau of swelling ratio parameter was reached after a maximum of 5h

incubation in PBS. Additionally, at this time point, all the samples gave back to their original form and weight (Fig. 82). In this case, the swelling phenomenon was completely due to the hydrogel counterpart. PCL/HA (i.e., r.m. and prec.) swelling ratio was used as control. As shown in fig. 83 the PCL/HA (i.e., r.m. and prec.) swelling ratio was negligible after 24h (i.e., ~5% of the initial weight). Moreover, PCL/HA water uptake was related to the water income into the material pores. Moreover, a comparison in terms of swelling ratio was made between the multi-component based scaffolds (i.e., Gel/HA r.m.-PCL/HA (i.e., r.m. and prec.)) and the crosslinked based hydrogels (i.e., gelatin and Gel/HA r.m.). A higher swelling ratio was observed for the latter, indicating that the water uptake at the interface (i.e., between PCL/HA and Gel/HA r.m.) was hindered by the thermoplastic barrier.

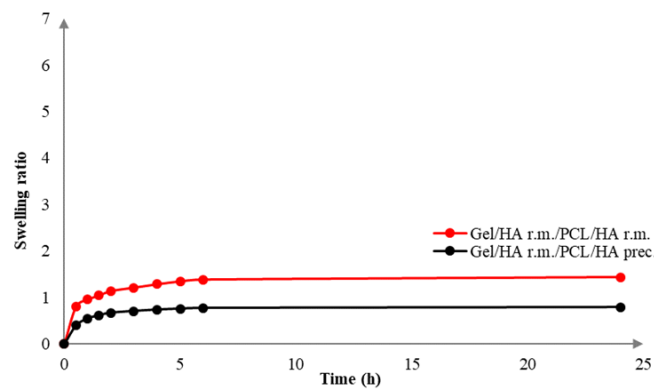


Figure 81: Swelling ratio of gel/HA r.m./PCL/HA r.m. and gel/HA r.m./PCL/HA prec.

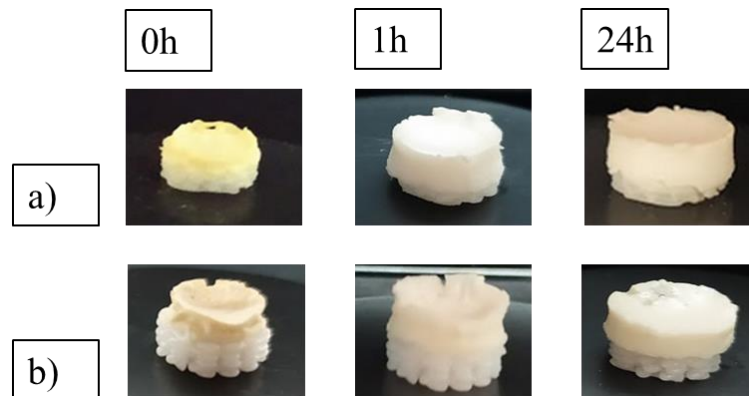


Figure 82: gel/HA r.m./PCL/HA r.m. and gel/HA r.m./PCL/HA prec. Samples after 0,1 and 24h in PBS solution.

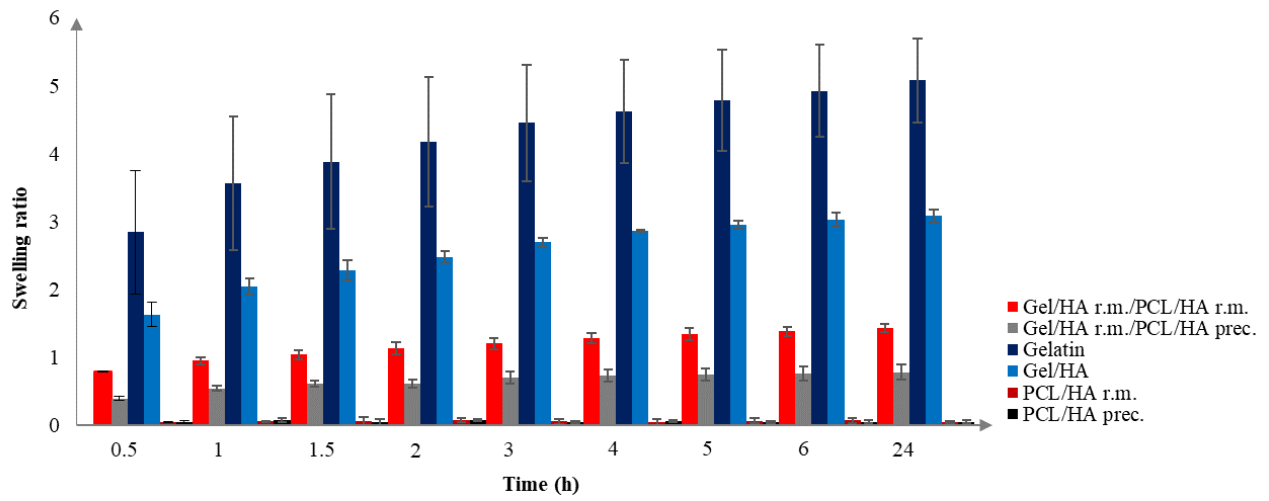


Figure 83: Swelling ratio of: PCL/HA (i.e., r.m. and prec.), PCL/HA-gel/HA r.m., gelatin and gel/HA r.m..

## 5. Conclusion and future works

This work aimed at the design and characterization of multi-component three-dimensional constructs for tissue engineering/regenerative medicine applications resulting from the combination of 3D printed scaffolds and hydrogels of natural origin. Specifically, glutaraldehyde (GA) cross-linked (10 minute immersion in a 0.25% v/v GA solution) and photocured (at 365 nm, 12 mW/cm<sup>2</sup>, 1 minute) gelatin/hydroxyapatite composite hydrogels (gel/HA and GelMA/HA, respectively) were combined with poly( $\epsilon$ -caprolactone)/HA (PCL-HA) 3D printed scaffolds (fabricated through pressure assisted microsyringe technique, circular shape, square grid, diameter strand 320  $\mu$ m, distance between strands 600  $\mu$ m, 7 layers). Each constituent of the composite scaffolds was first designed and thoroughly characterized. Concerning gelatin-based cross-linked hydrogels, samples were realized starting from a gelatin (from porcine skin, type A) solution at 15% w/v concentration that, upon thermal gelation, was crosslinked through immersion in a GA solution. The resulting crosslinked structures were analyzed in terms of chemical composition through Attenuated Total Reflectance Fourier Transform Infrared (ATR-FTIR) spectroscopy, in order to assess the success of the crosslinking process. Internal structure and morphology were assessed by Scanning Electron Microscope (SEM) and Micro-Computed Tomography ( $\mu$ CT). Swelling analyses were also carried out on freeze-dried gelatin (15% w/v in 0.25% v/v GA solution) gel, showing a complete recovery of sample initial wet weigh in 5h. As a different approach to design gelatin-based crosslinked gels, photocurable methacryloyl gelatin (GelMA) with different degrees of methacryloylation (DoMs) (i.e., 67 and 74 %, as assessed by Proton Nuclear Magnetic Resonance Spectroscopy) was synthesized by reacting gelatin (gelatin from porcine skin, type A) with methacrylic anhydride (at a concentration of 1.6% and 2.5% v/v). As synthesized GelMAs were also characterized by ATR-FTIR spectroscopy and colorimetric ninhydrin assay (Kaiser test) for indirect methacryloylation degree estimation. The ability of gelMA aqueous solutions (at 5, 8, 10, 12, 15, 18 and 20% w/v) to form gels at a specific temperature was verified by tube inverting test, using gelatin as control. At 15% w/v concentration, both kinds of GelMAs formed a stable gel at lower temperature compared to gelatin (25 vs 28 °C) due to the presence of exposed methacryloyl groups hindering single helices reorganization into an organized network. Then, gelMA solutions (at concentration of 10% and 15% w/v) were photocured, exploiting Lithium phenyl-2,4,6-trimethylbenzoylphosphinate (LAP) as photoinitiator (at a concentration of 0.05% and 0.05% w/v) and a UV light source (at 10 mW/cm<sup>2</sup> and 365 nm), in order to obtain photo-polymerized gels. Stiffer hydrogels were obtained by increasing GelMA degree of methacryloylation, the amount of photoinitiator and gelMA concentration. Freeze-dried GelMA gels were also characterized in terms of swelling capability, with GelMA\_74% gels reaching lower

swelling percentages compared to GelMA\_67% systems irrespective of its concentration within the gels. Additionally, a complete recovery of sample initial wet weigh was observed in 5h. Photo-rheological measurements evidenced higher storage modulus values and faster crosslinking rates with increasing LAP concentration. Higher storage modulus values were also achieved by increasing GelMA concentration within the hydrogels. In order to develop composite hydrogels, hydroxyapatite powder was synthesized following two different precipitation methods, which involved Calcium hydroxide ( $\text{Ca}(\text{OH})_2$ ) and Phosphoric acid ( $\text{H}_3\text{PO}_4$ ) as precursors. The first precipitation method was performed at 100 °C (obtaining HA prec.), while the second one was carried out at room temperature (obtaining HA r.m.). The resulting hydroxyapatite powders were characterized in terms of chemical composition, crystallinity, and morphology (by means of Energy Dispersive X-ray spectroscopy, X-Ray power Diffraction and Field Emission Scanning Electron Microscope respectively). Both the followed protocols led to the successful synthesis of hydroxyapatite crystals. Indeed, both HA r.m. and HA prec. exhibited a Ca:P ratio (i.e., 1.66 and 1.87 respectively) similar to the stoichiometric value of 1.67, meanwhile round shape and spindle-shape morphologies was obtained for HA prec. and HA r.m., respectively. Then, HA dispersion within gelatin and gelMA solutions was analyzed in order to optimize the protocol for composite hydrogels fabrication (HA and gelatin concentrations were set at 10% w/v and 10-15% w/v, respectively). HA-GelMA dispersions were also characterized in terms of stability (both at room temperature and 37 °C for 10 min, 2h and 24h) and capability to form physical gels. Gelation of HA-containing GelMA solutions occurred within few minutes at room temperature, leading to stable dispersions, while hydroxyapatite precipitation was evident after 2h at 37 °C. Furthermore, compositions containing gelMA at 10% w/v concentration exhibited a faster hydroxyapatite precipitation, due to their lower viscosity. Tube inverting test evidenced that hydroxyapatite loading did not hinder the temperature driven gelation even at high concentration (i.e., 10% w/v). The abovementioned composite formulations were also characterized by photo-rheology, showing that hydroxyapatite did not hinder the crosslinking phenomenon. Structural and morphological analyses were carried out on gelMA/hydroxyapatite samples exploiting Scanning Electron Microscope (SEM) and micro-computed tomography ( $\mu\text{CT}$ ), highlighting the different distribution of hydroxyapatite powders, which turned out to be correlated to the type and concentration of HA within the samples (better dispersion was achieved with HA r.m. compared to HA prec. and at lower HA concentration). Optimized protocol for HA dispersion within GelMA was also adopted in the preparation of GA crosslinked gel-HA gels. In view of the design of multicomponent 3D matrices based on a thermoplastic scaffold combined with a hydrogel, poly( $\epsilon$ -caprolactone)/HA 3D-printed structures were fabricated (exploiting both HA r.m. and HA prec. at  $\pm 10\%$  w/w) by means of the EnvisionTEC's 3D Bioplotter technology. The printing process was

optimized to obtain layered structures with an open porosity of approx. 59% and 62% for PCL/HA prec. and PCL/HA r.m. respectively. Fabricated scaffolds were characterized in terms of water uptake capability, morphology, porosity and mechanical properties (by means of swelling test, SEM, micro-computed tomography and mechanical tests, respectively). Compressive tests carried out on PCL/HA (i.e., HA r.m. and HA prec.) based scaffolds showed an overall hardening of the structures compared with the literature Young's Modulus values of PCL based porous scaffolds (i.e., approx. 51 MPa, with a porosity of 60%). Specifically, in this work, differences between PCL/HA prec. and PCL/HA r.m. were appreciated in terms of Young Modulus (i.e.,  $54 \pm 0.32$  and  $69 \pm 2.01$  MPa, respectively) and compressive strain at maximum compressive load (i.e.,  $8 \pm 0.0001$  % and  $20 \pm 0.0001$ %, respectively for PCL/HA r.m. and PCL/HA prec.). These differences were attributed to the intrinsic characteristics of the ceramic counterpart (i.e., higher Young Modulus related to the sintering process) and to the amount of particle aggregates (i.e., higher for HA r.m. nanoparticles) within the PCL phase. Moreover, visual analyses of  $\mu$ CT and SEM images, showed the better HA prec. dispersion within PCL, compared to the one obtained with HA r.m.. Also, this result was explained by the higher probability of anisotropic particles (i.e., HA r.m. needle shaped nanoparticles) to form aggregates at the nanometric scale if compared with spherical ones (i.e., HA prec. nanoparticles). Finally, the coupling between PCL/HA scaffolds and composite gel/HA r.m. hydrogels (at concentration of 15% w/v and 10% w/v for gelatin and HA r.m., respectively) was performed (through crosslinking with GA at 0.25% v/v). The final structures were characterized in terms of swelling capability, morphology, porosity and mechanical properties (by means of swelling test, SEM, micro-computed tomography and compressive tests), using PCL/HA scaffolds as control. Structural changings occurred because of gelatin/HA r.m. inclusion into PCL/HA. Specifically, compared with PCL/HA based scaffolds as such, open porosity at the interface between the hydrogel (i.e., gelatin/HA r.m.) and the thermoplastic matrix (i.e., PCL/HA), was reduced at 52% and 48% for PCL/HA prec.-gel/HA r.m. and PCL/HA r.m.-gel/HA r.m., respectively. Swelling capability of gelatin/HA r.m. was also lowered (i.e., with respect to the hydroxyapatite-containing hydrogel alone) because of the presence of the hydrophobic PCL/HA barrier. Further analyses are required to have a better knowledge of the produced material properties. Specifically, compressive test should be carried out on multicomponent scaffolds (i.e., PCL/HA r.m.-gel/HA r.m., PCL/HA prec.-gel/HA r.m). Moreover, degradation rate and biocompatibility should be assessed (i.e., evaluating scaffold properties after immersion in PBS for more than 7 days and performing long lasting cell culture respectively). Future works will also involve the realization of PCL/HA-gelMA/HA multicomponent scaffolds, in order to investigate the possibility to produce structures by means of different crosslinking methods. Then, the obtained products should be analyzed in terms of mechanical properties, inner and external structures, but also

swelling and degradation behavior. Additionally, full 3D printed composite scaffolds could be produced by printing also gel/HA r.m. or gelMA/HA hydrogels instead of using them as a bulk layer integrated with PCL/HA porous matrices. Such an approach will allow the design of structures with precise shape and highly tunable mechanical properties. To summarize, in this work a proof of concept of the feasibility to design multicomponent 3D scaffolds by combining different forming-materials and fabrication technologies was assessed. Thanks to the many degrees of freedom of the proposed platform, composite structures with highly tunable properties can be obtained acting on scaffold composition, material selection and concentration, and crosslinking approach and degree. The here-manufactured composite scaffolds could have high potential for tissue engineering applications, in particular in all those cases in which an interface between different tissues should be repaired and regenerated, such as in osteochondral tissue engineering.

## Bibliography

- [1] J. Vacanti, «Tissue engineering and regenerative medicine: from first principles to state of the art», *J. Pediatr. Surg.*, vol. 45, n. 2, pagg. 291–294, feb. 2010, doi: 10.1016/j.jpedsurg.2009.10.063.
- [2] D. J. Polak, «Regenerative medicine. Opportunities and challenges: a brief overview», *J. R. Soc. Interface*, vol. 7, n. suppl\_6, dic. 2010, doi: 10.1098/rsif.2010.0362.focus.
- [3] H.-Y. Cheung, K.-T. Lau, T.-P. Lu, e D. Hui, «A critical review on polymer-based bio-engineered materials for scaffold development», *Compos. Part B Eng.*, vol. 38, n. 3, pagg. 291–300, apr. 2007, doi: 10.1016/j.compositesb.2006.06.014.
- [4] D. W. Hutmacher e S. Cool, «Concepts of scaffold-based tissue engineering—the rationale to use solid free-form fabrication techniques», *J. Cell. Mol. Med.*, vol. 11, n. 4, pagg. 654–669, lug. 2007, doi: 10.1111/j.1582-4934.2007.00078.x.
- [5] J. M. Rosiak e F. Yoshii, «Hydrogels and their medical applications», *Nucl. Instrum. Methods Phys. Res. Sect. B Beam Interact. Mater. At.*, vol. 151, n. 1–4, pagg. 56–64, mag. 1999, doi: 10.1016/S0168-583X(99)00118-4.
- [6] J. P. Glotzbach, V. W. Wong, G. C. Gurtner, e M. T. Longaker, «In Brief», *Curr. Probl. Surg.*, vol. 48, n. 3, pagg. 142–146, mar. 2011, doi: 10.1067/j.cpsurg.2010.11.001.
- [7] L. L. Hench, «Third-Generation Biomedical Materials», *Science*, vol. 295, n. 5557, pagg. 1014–1017, feb. 2002, doi: 10.1126/science.1067404.
- [8] B. Guo e P. X. Ma, «Synthetic biodegradable functional polymers for tissue engineering: a brief review», *Sci. China Chem.*, vol. 57, n. 4, pagg. 490–500, apr. 2014, doi: 10.1007/s11426-014-5086-y.
- [9] E. M. Ahmed, «Hydrogel: Preparation, characterization, and applications: A review», *J. Adv. Res.*, vol. 6, n. 2, pagg. 105–121, mar. 2015, doi: 10.1016/j.jare.2013.07.006.
- [10] A. A. Mariod e H. F. Adam, «REVIEW: GELATIN, SOURCE, EXTRACTION AND INDUSTRIAL APPLICATIONS», *Review*, pag. 13.
- [11] Lh. Yahia, «History and Applications of Hydrogels», *J. Biomed. Sci.*, vol. 04, n. 02, 2015, doi: 10.4172/2254-609X.100013.
- [12] A. K. Gupta, «ENVIRONMENTAL RESPONSIVE HYDROGELS: A NOVEL APPROACH IN DRUG DELIVERY SYSTEM», *J. Drug Deliv. Ther.*, vol. 2, n. 1, gen. 2012, doi: 10.22270/jddt.v2i1.87.

- [13] E. M. White, J. Yatvin, J. B. Grubbs, J. A. Bilbrey, e J. Locklin, «Advances in smart materials: Stimuli-responsive hydrogel thin films», *J. Polym. Sci. Part B Polym. Phys.*, vol. 51, n. 14, pagg. 1084–1099, lug. 2013, doi: 10.1002/polb.23312.
- [14] C. S. Satish, K. P. Satish, e H. G. Shivakumar, «Hydrogels as controlled drug delivery systems: Synthesis, crosslinking, water and drug transport mechanism», *Indian J. Pharm. Sci.*, vol. 68, n. 2, 2006, doi: 10.4103/0250-474X.25706.
- [15] Y. Qiu e K. Park, «Environment-sensitive hydrogels for drug delivery», *Adv. Drug Deliv. Rev.*, vol. 64, pagg. 49–60, dic. 2012, doi: 10.1016/j.addr.2012.09.024.
- [16] S. Van Vlierberghe, P. Dubruel, e E. Schacht, «Biopolymer-Based Hydrogels As Scaffolds for Tissue Engineering Applications: A Review», *Biomacromolecules*, vol. 12, n. 5, pagg. 1387–1408, mag. 2011, doi: 10.1021/bm200083n.
- [17] N. Bhattarai, H. R. Ramay, J. Gunn, F. A. Matsen, e M. Zhang, «PEG-grafted chitosan as an injectable thermosensitive hydrogel for sustained protein release», *J. Controlled Release*, vol. 103, n. 3, pagg. 609–624, apr. 2005, doi: 10.1016/j.jconrel.2004.12.019.
- [18] M. Zrínyi, «Intelligent polymer gels controlled by magnetic fields», *Colloid Polym. Sci.*, vol. 278, n. 2, pagg. 98–103, feb. 2000, doi: 10.1007/s003960050017.
- [19] Z. Lei, Q. Wang, S. Sun, W. Zhu, e P. Wu, «A Bioinspired Mineral Hydrogel as a Self-Healable, Mechanically Adaptable Ionic Skin for Highly Sensitive Pressure Sensing», *Adv. Mater.*, vol. 29, n. 22, pag. 1700321, giu. 2017, doi: 10.1002/adma.201700321.
- [20] T. Naota e H. Koori, «Molecules That Assemble by Sound: An Application to the Instant Gelation of Stable Organic Fluids», *J. Am. Chem. Soc.*, vol. 127, n. 26, pagg. 9324–9325, lug. 2005, doi: 10.1021/ja050809h.
- [21] K. Saini, «Preparation method, Properties and Crosslinking of hydrogel: a review», vol. 5, n. 1, pag. 10.
- [22] B. D. Martin, R. J. Linhardt, e J. S. Dordick, «Highly swelling hydrogels from ordered galactose-based polyacrylates», *Biomaterials*, vol. 19, n. 1–3, pagg. 69–76, gen. 1998, doi: 10.1016/S0142-9612(97)00184-1.
- [23] S. A. Sell, M. J. McClure, K. Garg, P. S. Wolfe, e G. L. Bowlin, «Electrospinning of collagen/biopolymers for regenerative medicine and cardiovascular tissue engineering», *Adv. Drug Deliv. Rev.*, vol. 61, n. 12, pagg. 1007–1019, ott. 2009, doi: 10.1016/j.addr.2009.07.012.
- [24] A. M. Ferreira, P. Gentile, V. Chiono, e G. Ciardelli, «Collagen for bone tissue regeneration», *Acta Biomater.*, vol. 8, n. 9, pagg. 3191–3200, set. 2012, doi: 10.1016/j.actbio.2012.06.014.
- [25] R. A. F. Clark, K. Ghosh, e M. G. Tonnesen, «Tissue Engineering for Cutaneous Wounds», *J. Invest. Dermatol.*, vol. 127, n. 5, pagg. 1018–1029, mag. 2007, doi: 10.1038/sj.jid.5700715.

- [26] M. E. Nimni, «Collagen: Structure, function, and metabolism in normal and fibrotic tissues», *Semin. Arthritis Rheum.*, vol. 13, n. 1, pagg. 1–86, ago. 1983, doi: 10.1016/0049-0172(83)90024-0.
- [27] S. Ricard-Blum, «The Collagen Family», *Cold Spring Harb. Perspect. Biol.*, vol. 3, n. 1, pagg. a004978–a004978, gen. 2011, doi: 10.1101/cshperspect.a004978.
- [28] D. I. Zeugolis, G. R. Paul, e G. Attenburrow, «Cross-linking of extruded collagen fibers-A biomimetic three-dimensional scaffold for tissue engineering applications», *J. Biomed. Mater. Res. A*, vol. 89A, n. 4, pagg. 895–908, giu. 2009, doi: 10.1002/jbm.a.32031.
- [29] P. Zhou e J. M. Regenstein, «Effects of Alkaline and Acid Pretreatments on Alaska Pollock Skin Gelatin Extraction», *J. Food Sci.*, vol. 70, n. 6, pagg. c392–c396, mag. 2006, doi: 10.1111/j.1365-2621.2005.tb11435.x.
- [30] G.-H. Wu e S. Hsu, «Review: Polymeric-Based 3D Printing for Tissue Engineering», *J. Med. Biol. Eng.*, vol. 35, n. 3, pagg. 285–292, giu. 2015, doi: 10.1007/s40846-015-0038-3.
- [31] B. J. Klotz, D. Gawlitta, A. J. W. P. Rosenberg, J. Malda, e F. P. W. Melchels, «Gelatin-Methacryloyl Hydrogels: Towards Biofabrication-Based Tissue Repair», *Trends Biotechnol.*, vol. 34, n. 5, pagg. 394–407, mag. 2016, doi: 10.1016/j.tibtech.2016.01.002.
- [32] K. Yue, G. Trujillo-de Santiago, M. M. Alvarez, A. Tamayol, N. Annabi, e A. Khademhosseini, «Synthesis, properties, and biomedical applications of gelatin methacryloyl (GelMA) hydrogels», *Biomaterials*, vol. 73, pagg. 254–271, dic. 2015, doi: 10.1016/j.biomaterials.2015.08.045.
- [33] F. Xu *et al.*, «Three-Dimensional Magnetic Assembly of Microscale Hydrogels», *Adv. Mater.*, vol. 23, n. 37, pagg. 4254–4260, 2011, doi: 10.1002/adma.201101962.
- [34] E. Kaemmerer, F. P. W. Melchels, B. M. Holzapfel, T. Meckel, D. W. Hutmacher, e D. Loessner, «Gelatin methacrylamide-based hydrogels: An alternative three-dimensional cancer cell culture system», *Acta Biomater.*, vol. 10, n. 6, pagg. 2551–2562, giu. 2014, doi: 10.1016/j.actbio.2014.02.035.
- [35] B. Dhandayuthapani, Y. Yoshida, T. Maekawa, e D. S. Kumar, «Polymeric Scaffolds in Tissue Engineering Application: A Review», *Int. J. Polym. Sci.*, vol. 2011, pagg. 1–19, 2011, doi: 10.1155/2011/290602.
- [36] J. R. Woodard *et al.*, «The mechanical properties and osteoconductivity of hydroxyapatite bone scaffolds with multi-scale porosity», *Biomaterials*, vol. 28, n. 1, pagg. 45–54, gen. 2007, doi: 10.1016/j.biomaterials.2006.08.021.
- [37] R. Z. LeGeros e J. P. LeGeros, «DENSE HYDROXYAPATITE», in *An Introduction to Bioceramics*, WORLD SCIENTIFIC, 1993, pagg. 139–180.

- [38] J. Venkatesan e S.-K. Kim, «Nano-Hydroxyapatite Composite Biomaterials for Bone Tissue Engineering—A Review», *J. Biomed. Nanotechnol.*, vol. 10, n. 10, pagg. 3124–3140, ott. 2014, doi: 10.1166/jbn.2014.1893.
- [39] S. Kuttappan, D. Mathew, e M. B. Nair, «Biomimetic composite scaffolds containing bioceramics and collagen/gelatin for bone tissue engineering - A mini review», *Int. J. Biol. Macromol.*, vol. 93, pagg. 1390–1401, dic. 2016, doi: 10.1016/j.ijbiomac.2016.06.043.
- [40] S. M. Peltola, F. P. W. Melchels, D. W. Grijpma, e M. Kellomäki, «A review of rapid prototyping techniques for tissue engineering purposes», *Ann. Med.*, vol. 40, n. 4, pagg. 268–280, gen. 2008, doi: 10.1080/07853890701881788.
- [41] B. K. Gu, D. J. Choi, S. J. Park, M. S. Kim, C. M. Kang, e C.-H. Kim, «3-dimensional bioprinting for tissue engineering applications», *Biomater. Res.*, vol. 20, n. 1, pag. 12, dic. 2016, doi: 10.1186/s40824-016-0058-2.
- [42] N. A. Sears, D. R. Seshadri, P. S. Dhavalikar, e E. Cosgriff-Hernandez, «A Review of Three-Dimensional Printing in Tissue Engineering», *Tissue Eng. Part B Rev.*, vol. 22, n. 4, pagg. 298–310, ago. 2016, doi: 10.1089/ten.teb.2015.0464.
- [43] M. A. Kuss *et al.*, «Short-term hypoxic preconditioning promotes prevascularization in 3D bioprinted bone constructs with stromal vascular fraction derived cells», *RSC Adv.*, vol. 7, n. 47, pagg. 29312–29320, 2017, doi: 10.1039/C7RA04372D.
- [44] M. Asim, M. Jawaid, N. Saba, Ramengmawii, M. Nasir, e M. T. H. Sultan, «Processing of hybrid polymer composites—a review», in *Hybrid Polymer Composite Materials*, Elsevier, 2017, pagg. 1–22.
- [45] W. Schuurman, V. Khristov, M. W. Pot, P. R. van Weeren, W. J. A. Dhert, e J. Malda, «Bioprinting of hybrid tissue constructs with tailorable mechanical properties», *Biofabrication*, vol. 3, n. 2, pag. 021001, giu. 2011, doi: 10.1088/1758-5082/3/2/021001.
- [46] A. Hamlekhan, M. Mozafari, N. Nezafati, M. Azami, e H. Hadipour, «A Proposed Fabrication Method of Novel PCL-GEL-HAp Nanocomposite Scaffolds for Bone Tissue Engineering Applications», *Adv. Compos. Lett.*, vol. 19, n. 4, pag. 096369351001900, lug. 2010, doi: 10.1177/096369351001900401.
- [47] M. Abedalwafa, F. Wang, L. Wang, e C. Li, «BIODEGRADABLE POLY-EPSILON-CAPROLACTONE (PCL) FOR TISSUE ENGINEERING APPLICATIONS: A REVIEW», pag. 18.
- [48] S. Gautam, A. K. Dinda, e N. C. Mishra, «Fabrication and characterization of PCL/gelatin composite nanofibrous scaffold for tissue engineering applications by electrospinning method», *Mater. Sci. Eng. C*, vol. 33, n. 3, pagg. 1228–1235, apr. 2013, doi: 10.1016/j.msec.2012.12.015.

- [49] X. Yang, F. Yang, X. F. Walboomers, Z. Bian, M. Fan, e J. A. Jansen, «The performance of dental pulp stem cells on nanofibrous PCL/gelatin/nHA scaffolds», *J. Biomed. Mater. Res. A*, vol. 9999A, pag. NA-NA, 2009, doi: 10.1002/jbm.a.32535.
- [50] Q. Zhang, K. Tan, Y. Zhang, Z. Ye, W.-S. Tan, e M. Lang, «In Situ Controlled Release of rhBMP-2 in Gelatin-Coated 3D Porous Poly( $\epsilon$ -caprolactone) Scaffolds for Homogeneous Bone Tissue Formation», *Biomacromolecules*, vol. 15, n. 1, pagg. 84–94, gen. 2014, doi: 10.1021/bm401309u.
- [51] H. Shirahama, B. H. Lee, L. P. Tan, e N.-J. Cho, «Precise Tuning of Facile One-Pot Gelatin Methacryloyl (GelMA) Synthesis», *Sci. Rep.*, vol. 6, n. 1, pag. 31036, ago. 2016, doi: 10.1038/srep31036.
- [52] H. Yang e A. M., «Vis/Near- and Mid- Infrared Spectroscopy for Predicting Soil N and C at a Farm Scale», in *Infrared Spectroscopy - Life and Biomedical Sciences*, T. Theophile, A c. di InTech, 2012.
- [53] M.-M. Blum e H. John, «Historical perspective and modern applications of Attenuated Total Reflectance - Fourier Transform Infrared Spectroscopy (ATR-FTIR): Modern applications of ATR-FTIR», *Drug Test. Anal.*, vol. 4, n. 3–4, pagg. 298–302, mar. 2012, doi: 10.1002/dta.374.
- [54] S. H. Moolenaar, U. F. H. Engelke, e R. A. Wevers, «Proton nuclear magnetic resonance spectroscopy of body fluids in the field of inborn errors of metabolism», *Ann. Clin. Biochem.*, vol. 40, n. 1, pagg. 16–24, gen. 2003, doi: 10.1258/000456303321016132.
- [55] M. Zhu, Y. Wang, G. Ferracci, J. Zheng, N.-J. Cho, e B. H. Lee, «Gelatin methacryloyl and its hydrogels with an exceptional degree of controllability and batch-to-batch consistency», *Sci. Rep.*, vol. 9, n. 1, pag. 6863, dic. 2019, doi: 10.1038/s41598-019-42186-x.
- [56] E. Hoch, C. Schuh, T. Hirth, G. E. M. Tovar, e K. Borchers, «Stiff gelatin hydrogels can be photo-chemically synthesized from low viscous gelatin solutions using molecularly functionalized gelatin with a high degree of methacrylation», *J. Mater. Sci. Mater. Med.*, vol. 23, n. 11, pagg. 2607–2617, nov. 2012, doi: 10.1007/s10856-012-4731-2.
- [57] C. Pontremoli *et al.*, «Hybrid injectable platforms for the in situ delivery of therapeutic ions from mesoporous glasses», *Chem. Eng. J.*, vol. 340, pagg. 103–113, mag. 2018, doi: 10.1016/j.cej.2018.01.073.
- [58] S. Pahoff, C. Meinert, O. Bas, L. Nguyen, T. J. Klein, e D. W. Hutmacher, «Effect of gelatin source and photoinitiator type on chondrocyte redifferentiation in gelatin methacryloyl-based tissue-engineered cartilage constructs», *J. Mater. Chem. B*, vol. 7, n. 10, pagg. 1761–1772, 2019, doi: 10.1039/C8TB02607F.

- [59] S. T. Ho e D. W. Hutmacher, «A comparison of micro CT with other techniques used in the characterization of scaffolds», *Biomaterials*, vol. 27, n. 8, pagg. 1362–1376, mar. 2006, doi: 10.1016/j.biomaterials.2005.08.035.
- [60] C. J. Wilcock, P. Gentile, P. V. Hatton, e C. A. Miller, «Rapid Mix Preparation of Bioinspired Nanoscale Hydroxyapatite for Biomedical Applications», *J. Vis. Exp.*, n. 120, pag. 55343, feb. 2017, doi: 10.3791/55343.
- [61] R. Kumar, K. H. Prakash, P. Cheang, e K. A. Khor, «Temperature Driven Morphological Changes of Chemically Precipitated Hydroxyapatite Nanoparticles», *Langmuir*, vol. 20, n. 13, pagg. 5196–5200, giu. 2004, doi: 10.1021/la049304f.
- [62] «EDX Analysis with a Scanning Electron Microscope (SEM): How Does it Work?» [In linea]. Available at: <https://blog.phenom-world.com/edx-analysis-sem>. [Consultato: 22-gen-2020].
- [63] U. Mohan Rao e R. K. Jarial, «Measurement of transformer solid insulation degradation using dilatometry and X-ray diffraction analysis», *Measurement*, vol. 131, pagg. 701–705, gen. 2019, doi: 10.1016/j.measurement.2018.09.024.
- [64] A. Mayeen, L. K. Shaji, A. K. Nair, e N. Kalarikkal, «Morphological Characterization of Nanomaterials», in *Characterization of Nanomaterials*, Elsevier, 2018, pagg. 335–364.
- [65] H. Cheng *et al.*, «Synergistic interplay between the two major bone minerals, hydroxyapatite and whitlockite nanoparticles, for osteogenic differentiation of mesenchymal stem cells», *Acta Biomater.*, vol. 69, pagg. 342–351, mar. 2018, doi: 10.1016/j.actbio.2018.01.016.
- [66] S. Farris, J. Song, e Q. Huang, «Alternative Reaction Mechanism for the Cross-Linking of Gelatin with Glutaraldehyde», *J. Agric. Food Chem.*, vol. 58, n. 2, pagg. 998–1003, gen. 2010, doi: 10.1021/jf9031603.
- [67] K. Rahali *et al.*, «Synthesis and Characterization of Nanofunctionalized Gelatin Methacrylate Hydrogels», *Int. J. Mol. Sci.*, vol. 18, n. 12, pag. 2675, dic. 2017, doi: 10.3390/ijms18122675.
- [68] J. Hossan, M. A. Gafur, M. R. Kadir, e M. M. Karim, «Preparation and Characterization of Gelatin-Hydroxyapatite Composite for Bone Tissue Engineering», *Int. J. Eng.*, vol. 14, n. 01, pag. 9, 2014.
- [69] N. G. Parker e M. J. W. Povey, «Ultrasonic study of the gelation of gelatin: Phase diagram, hysteresis and kinetics», *Food Hydrocoll.*, vol. 26, n. 1, pagg. 99–107, gen. 2012, doi: 10.1016/j.foodhyd.2011.04.016.
- [70] K. H. Prakash, R. Kumar, C. P. Ooi, P. Cheang, e K. A. Khor, «Apparent Solubility of Hydroxyapatite in Aqueous Medium and Its Influence on the Morphology of Nanocrystallites with Precipitation Temperature», *Langmuir*, vol. 22, n. 26, pagg. 11002–11008, dic. 2006, doi: 10.1021/la0621665.

- [71] A. Kohutová, P. Honcová, L. Svoboda, P. Bezdička, e M. Maříková, «Structural characterization and thermal behaviour of biological hydroxyapatite», *J. Therm. Anal. Calorim.*, vol. 108, n. 1, pagg. 163–170, apr. 2012, doi: 10.1007/s10973-011-1942-6.
- [72] M. Azami, F. Moztafzadeh, e M. Tahriri, «Preparation, characterization and mechanical properties of controlled porous gelatin/hydroxyapatite nanocomposite through layer solvent casting combined with freeze-drying and lamination techniques», *J. Porous Mater.*, vol. 17, n. 3, pagg. 313–320, giu. 2010, doi: 10.1007/s10934-009-9294-3.
- [73] T. Elzein, M. Nasser-Eddine, C. Delaite, S. Bistac, e P. Dumas, «FTIR study of polycaprolactone chain organization at interfaces», *J. Colloid Interface Sci.*, vol. 273, n. 2, pagg. 381–387, mag. 2004, doi: 10.1016/j.jcis.2004.02.001.
- [74] E. M. Hotze, T. Phenrat, e G. V. Lowry, «Nanoparticle Aggregation: Challenges to Understanding Transport and Reactivity in the Environment», *J. Environ. Qual.*, vol. 39, n. 6, pagg. 1909–1924, nov. 2010, doi: 10.2134/jeq2009.0462.
- [75] E. Nyberg, A. Rindone, A. Dorafshar, e W. L. Grayson, «Comparison of 3D-Printed Poly-ε-Caprolactone Scaffolds Functionalized with Tricalcium Phosphate, Hydroxyapatite, Bio-Oss, or Decellularized Bone Matrix <sup/>», *Tissue Eng. Part A*, vol. 23, n. 11–12, pagg. 503–514, giu. 2017, doi: 10.1089/ten.tea.2016.0418.
- [76] R. I. Martin e P. W. Brown, «Mechanical properties of hydroxyapatite formed at physiological temperature», *J. Mater. Sci. Mater. Med.*, vol. 6, n. 3, pagg. 138–143, mar. 1995, doi: 10.1007/BF00120289.
- [77] I. Luis de Redín *et al.*, «Human serum albumin nanoparticles for ocular delivery of bevacizumab», *Int. J. Pharm.*, vol. 541, n. 1–2, pagg. 214–223, apr. 2018, doi: 10.1016/j.ijpharm.2018.02.003.